Spring 5-10-2019

Synthesis, Characterization and Crystal Growth of I2-II-IV-VI4 and I4-II-IV2-VI7 Diamond-Like Semiconductors with potential In IR-NLO Applications

Jennifer Glenn

SYNTHESIS, CHARACTERIZATION AND CRYSTAL GROWTH OF I_2-II-IV-VI_4 AND I_4-II-IV_2-VI_7 DIAMOND-LIKE SEMICONDUCTORS WITH POTENTIAL IN INFRARED NONLINEAR OPTICAL APPLICATIONS

A Dissertation

Submitted to the Bayer School of Natural and Environmental Sciences

Duquesne University

In partial fulfillment of the requirements for

the degree of Doctor of Philosophy

By

Jennifer R. Glenn

May 2019

SYNTHESIS, CHARACTERIZATION AND CRYSTAL GROWTH OF I_2-II-IV-VI_4 AND I_4-II-IV_2-VI_7 DIAMOND-LIKE SEMICONDUCTORS WITH POTENTIAL IN INFRARED NONLINEAR OPTICAL APPLICATIONS

By

Jennifer R. Glenn

Approved March 29, 2019

Jennifer A. Aitken Professor of Chemistry (Committee Chair)	Michael Van Stipdonk Associate Professor of Chemistry (Committee Member)
Stephanie J. Wetzel Teaching Assistant Professor (Committee Member)	Joon I. Jang Associate Professor of Physics Sogang University (Committee Member)
Philip Reeder Dean and Professor, Bayer School of Natural and Environmental Sciences	Ellen Gawalt Chair, Department Chemistry and Biochemistry Professor of Chemistry

ABSTRACT

SYNTHESIS, CHARACTERIZATION AND CRYSTAL GROWTH OF I_2-II-IV-VI_4 AND I_4-II-IV_2-VI_7 DIAMOND-LIKE SEMICONDUCTORS WITH POTENTIAL IN INFRARED NONLINEAR OPTICAL APPLICATIONS

By

Jennifer R. Glenn

May 2019

Dissertation supervised by Dr. Jennifer A. Aitken

In this dissertation, several new and existing diamond-like semiconductors (DLSs) were synthesized and investigated for their potential in infrared nonlinear optical (IR-NLO) applications. In Chapter 2 growth of large single crystals of Li_2MnGeS_4 was carried out using iodine vapor transport and a newly created graphite-tube containment system. This crystallization method produced sizable single crystals on the scale of 2x1x1 mm^3, that were used to determine the material's magnetic properties. Magnetization data indicate that the compound is antiferromagnetic with a Néel temperature of 10 K and an effective magnetic moment of 5.6 μ_B/f.u.. The specific heat measurements show that as the field strength increases the Néel temperature decreases; the low Néel temperature confirms the weak magnetic coupling of the Mn^{2+} ions. Chapters 3, 4 and 5 report the new DLS $Cu_4MnGe_2S_7$, $Cu_4CdSi_2S_7$ and Li_2ZnSiS_4 for which detailed descriptions of

their physical and electronic structures are given. Chapter 4 also reports the NLO properties of $Cu_4MnGe_2S_7$ and Cu_2MnGeS_4. The $\chi^{(2)}$ value for $Cu_4MnGe_2S_7$ was determined to be 2.33 ± 0.86 pm/V. Due to the relatively weak SHG response, phase matching could only be tested up to 1600 nm, where the compound was found to be non-phase-matchable. On the other hand, Cu_2MnGeS_4 is phase matchable at 3100 nm and exhibits a significant $\chi^{(2)}$ value of 16.9 ± 2.0 pm/V. Chapter 6 presents a study in which one polymorph of Cu_2ZnSiS_4 was targeted through alteration of the cooling rate. These products of these reactions were analyzed via neutron diffraction and solid-state MAS-NMR. While a single polymorph was not attained, a modified beta polymorph (gamma) was discovered.

DEDICATION

This dissertation is dedicated to every figure skater whose Olympic moment is not at the Olympics.

Get Up

We all fall.

It's how we get up that matters.

By U.S. Figure Skating

Get Up. It sounds so simple, yet it's actually a skill – one that figure skaters do each day on the ice and in real life. It takes the same inner strength to master a double Axel as it does to study for a difficult test, stand up to bullies, overcome shyness or run for class president. Each fall in the rink, each wrong answer on a test, each nervous moment at the lectern is a step closer to success. As figure skaters know well, ice is slippery – you will fall.

The same can be said for life.

It's what you do next that matters.

And skaters Get Up.

ACKNOWLEDGEMENT

I would first like to thank Dr. Jennifer A. Aitken for the privilege of working in her lab and for introducing me to solid-state chemistry, which I have grown to love. Dr. Aitken's fierce interest in diamond-like semiconductors has allowed her to be awarded numerous National Science Foundation grants that allowed the work presented in this dissertation to be possible (DMR-1201729 and DMR-1611198). I would also like to thank the members of my dissertation committee Dr. Stephanie Wetzel, Dr. Michael Van Stipdonk and Dr. Joon Jang along with our department chair Dr. Gawalt for their continued support and guidance.

I am thankful to all the present and past members of the Aitken team for their support, help and comradery over the last five years. I don't know what I would have done without them.

This work would have not been possible without the help of numerous collaborators and they have my deepest gratitude for all their help and support. In addition to serving as one of my committee members, I would also like to thank Dr. Joon Jang and his student Jeong Bin for their help collecting NLO data. I wish to thank Dr. Joseph MacNeil and his students Kristi Deverant, Anne Radzanowski, and Delenne Fingerlow for their enormous help with the computational aspects of this work. Additionally, I would like to thank Dr. James Rodinelli and Raymond Wang for carrying out the electronic structure calculations for my magnetic materials. I would like to thank Dr. Jinlei Yao for collecting magnetic data and his patience in explaining them to me. A huge thanks is owed to our solid-state NMR collaborators, Dr. Michale Paris, Dr. Alain

Lafond, and Stephane Jobic without whom I would not have discovered the gamma polymorphs of Cu_2ZnSiS_4. Finally, I would like to thank Argonne National Lab and NIST for the use of their 11-BM and BT-1 diffraction instrumentation.

My deepest gratitude goes out to Dr. Casey Raymond, my undergraduate research advisor, for seeing in me what I had yet to see in myself. I will forever be in your debt, and I would not be writing a dissertation if it had not been for you. I am also grateful to those who started my journey towards being a scientist, Mr. Grizzaffi and Mr. Przedwiecki, who showed me that being nerdy could still be cool even when I was in high school.

Speaking of people from high school, I would also like to thank my soul sister, my person, my best friend Victoria Young. You have always supported me and I will never forget the many phone calls and glasses of wine we shared through my graduate school career, and how you always believed in me, even when I didn't.

You learn a lot in graduate school, but I need to thank my figure skating coaches Nikki Schallen-Colman and Karla Schallen for teaching me the most important lesson, one that helped me survive grad school. Thank you for teaching me how to get back up and try just "one more time".

To my Mom and Dad, I will never be able to express how much your support and belief in me means, so I will simply say thank you for everything.

TABLE OF CONTENTS

Page

LIST OF TABLES

Page

LIST OF FIGURES

Page

Chapter 1

1.1 Introduction

One of the world's most famous scientists, Francis Crick, said in his autobiography that, "If you want to study function, study structure". (*1,2*) While Crick is famous for his work in molecular biology, this idea extends deep into chemistry and materials science as well. This idea has been rebranded and continues to be the focus of science today. Most recently this idea has been reiterated by the Materials Genome Initiative (MGI) launched by the United States Federal government in 2011 to accelerate the discovery and development of advanced materials that are essential to economic security and human wellbeing. (*3*) According to the MGI there are seven steps between the discovery and deployment of new materials; discovery, development, property optimization, systems design and integration, certification, manufacturing and deployment. (*3*) Research carried out at the university level and presented in this dissertation tackles the first part of the MGI and reports the discovery of new materials, investigates their properties and their potential uses.

While many new materials are discovered serendipitously or by trial and error, in contrast, this work exploits the synthetic predictability of diamond-like semiconductors (DLSs) and focuses on their potential use in the field of nonlinear optics, specifically the area of second harmonic generation (SHG). To this end the new compounds $Cu_4MnGe_2S_7$, $Cu_4CdSi_2S_7$ and Li_2ZnSiS_4 have been investigated in this work. Li_2MnGeS_4 and Cu_2ZnSiS_4 were further investigated as they have been previously reported with promising properties.

1.1.1 Tetrahedral (Diamond-like) Structure

DLSs are ideal for creating candidate SHG materials, as they are inherently noncentrosymmetric, i.e. do not possess an inversion center. The lack of an inversion center is a result of the tetrahedral building blocks and the packing of those building blocks, where they align along one direction to create the larger crystal structure. (*4*) In our reactions, it is not possible to start out with tetrahedral building blocks and we cannot make them pack into a noncentrosymmetric structure, but as a mental exercise the idea of building blocks can be used to explain the creation of diamond-like structures. The process of creating a DLS starts with choosing elements that have a preference towards a tetrahedral coordination. This type of coordination is preferred as a tetrahedron lacks an inversion center. Each individual tetrahedron can be abstractly thought of as a building block. Acentric building blocks are conceptually targeted as they would ideally pack into a noncentrosymmetric structure. It is possible to encourage such a design by following the guidelines for creating DLSs, which are inherently noncentrosymmetric due to the alignment of all the metal-sulfur tetrahedra in one crystallographic direction. (*4*)

1.1.2 Designing Diamond-like Semiconductors (DLSs)

Diamond-like semiconductors can be created by following three or four guidelines. Those of the general formula I_4-II-IV_2-VI_7 only follow the first three. This work concentrates on quaternary DLSs, therefore the quaternary formulae will be used to exemplify them. The general formula I_2-II-IV-VI_4 will be used to illustrate a normal DLS, in which the roman numerals represent the valence electrons of the atoms and the numerical subscripts indicate the stoichiometry. The first guideline is that each of the ions must be tetrahedrally coordinated. (*4,5*) The corner-sharing of the tetrahedral ions creates the intrinsically noncentrosymmetric structure exhibited by DLSs. The

average number of valence electrons must be four (*4,5*), and the average number of valence electrons per anion must equal eight. (*4,5*) The final guideline is Pauling's second rule which states that the charge of the anion is compensated by its nearest neighboring cations for the polyhedron to be regular. (*6*) If a material obeys Pauling's second rule, it will be the most stable configuration. Materials that do not follow Pauling's second rule, such as I_4-II-IV_2-VI_7 DLSs, can also be targeted. All I_2-II-IV-VI_4 DLSs follow Pauling's second rule and will therefore be used to exemplify how it is satisfied, Figure 1.1. The cations of I_2-II-IV-VI_4 (I, II, and IV) have +1, +2, and +4 charges, respectively, and the VI anion has a -2 charge. As each of the cation's is bound to four hexavalent anions, therefore only one fourth of the cations charge is contributed towards each hexavalent anion. The tetrahedral coordination of an isolated hexavalent anion consists of to two monovalent, one divalent and one tetravalent cation. This bonding results in a +1/4 (times two), +1/2, and +1 charges donated from the monovalent, divalent and tetravalent cations, respectively, producing an overall cationic charge of +2 that is locally charge balanced by the -2 charge of the hexavalent anion.

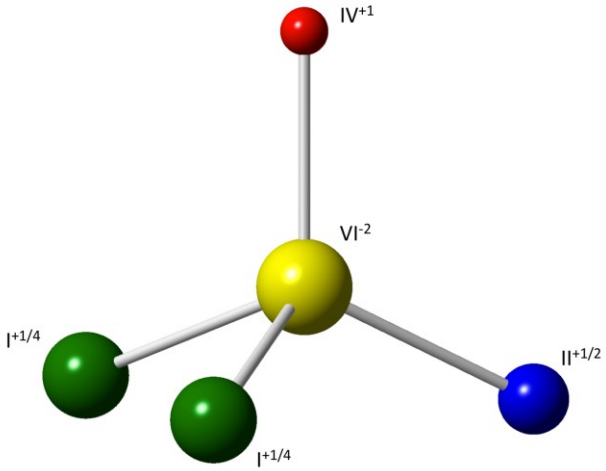

Figure 1.1: I_2-II-IV-VI_4 tetrahedron that adheres to Pauling's second rule.

1.1.3 Compositional Flexibility

One advantage of DLSs is that they are compositionally flexible, a quality that can be exploited to tune the properties of a material. There are a few ways in which compositional flexibility can

be manipulated including doping, solid-solutions, choice of elements, the progression of DLSs from binary to ternary and quaternary materials, and changes in stoichiometry. The process of doping is well known for its use in tuning semiconductors, as it allows for a small amount of an element to replace another element in the parent material or incorporate into an interstitial space. (*7-9*) Doping results in two forms of semiconductors p- or n-type. An n-type material is one in which the dopant element donates electrons to the parent material, thus increasing the conductivity. (*7-9*) A p-type dopant creates deficiencies of valence electrons resulting in holes in the charge carriers. (*7-9*) Solid-solutions allow for a larger amount of substitution than doping, with atoms or ions either directly replacing an atom or ion in the parent structure. (*10*) They result in new solids all the way across the series $A_{1-x}C_xB$ from AB to CB. (*10*) For DLSs the choice of elements is determined by the element's valency and its preference for tetrahedral coordination. While there is a finite selection of elements, the possible combinations of these elements vastly increase the number of potential compounds. For quaternary DLSs of the general formula I_2-II-IV-VI_4 and I_4-II-IV_2-VI_7, which are studied in this work, the choice of elements is limited to those that have one, two, four and six valence electrons. Theoretically this results in thousands of combinations, although they are not all possible as the synthesis of some materials are not favorable. The high cost of some elements, the ease of which the elements can be obtained and other hazards associated with them limit the choices. The selection of elements can also be used to tune the bandgap of a material, exemplified by the ternary DLSs and their corresponding bandgap energies listed in Table 1.1. (*11-13*) In each set of materials there are three

Table 1.1: Select ternary DLSs and their corresponding bandgap energies.

DLS	Bandgap	Reference
$LiGaS_2$	3.62 eV	*11*
$AgGaS_2$	2.76 eV	*12*
$CuGaS_2$	2.40 eV	*13*
$LiGaSe_2$	3.13 eV	*11*
$AgGaSe_2$	1.83 eV	*12*
$CuGaSe_2$	1.70 eV	*13*
$LiInS_2$	3.56 eV	*11*
$AgInS_2$	2.03 eV	*13*
$CuInS_2$	1.53 eV	*13*

different monovalent ions and it can be observed that changing the monovalent ion affects the bandgap. As the monovalent ion is changed from lithium to silver to copper the bandgap decreases, in each case. Table 1.1 also illustrates how changing the hexavalent ion can affect the bandgap, when comparing $LiGaS_2$ to $LiGaSe_2$, $AgGaS_2$ to $AgGaSe_2$, and $CuGaS_2$ to $CuGaSe_2$ the bandgap decreases when the hexavalent ion is changed from sulfur to selenium.

The tunability of DLSs can also be altered by the progression of DLSs. All DLSs are structurally derived from either cubic or hexagonal diamond. (*5*) This progression has led to the creation of binary, ternary and quaternary normal tetrahedral DLSs, by using cross substitution as illustrated in Figure 1.2. The general formula of cubic and hexagonal diamond consists of four valence electrons, by doubling the number of valence electrons to eight and using a divalent and hexavalent ion, a binary DLS can be theorized. A ternary DLS is theorized by doubling the number of valence electrons again (16 valence electrons) and splitting these electrons among one monovalent, one trivalent and two hexavalent ions. Quaternary DLSs arise from a third doubling to attain 32 valence electrons that are distributed among two monovalent, one divalent, one tetravalent and four hexavalent ions. Each time another element has been added to the general formula, the selection of elements has increased, thus opening more options for further tuning the properties. Altering the stoichiometry of the DLS formula is also an option, such as changing the stoichiometry from I_2-II-IV-VI_4 to I_4-II-IV_2-VI_7, which is investigated in the work presented here.

Tuning the properties of DLSs is important to extending their utility in new applications and devices. This work focuses on DLSs for their use in nonlinear optics, where the bandgap of a material can be altered to also affect the second-order nonlinear optical (NLO) susceptibility and laser-induced damage threshold (LIDT). (*14-16*) This is possible, as the bandgap of a material and its SHG are generally inversely related (*15*), while bandgap and LIDT are directly related. (*16*) Therefore, by carefully choosing elements, and the appropriate stoichiometry, a material with a desired property can be targeted.

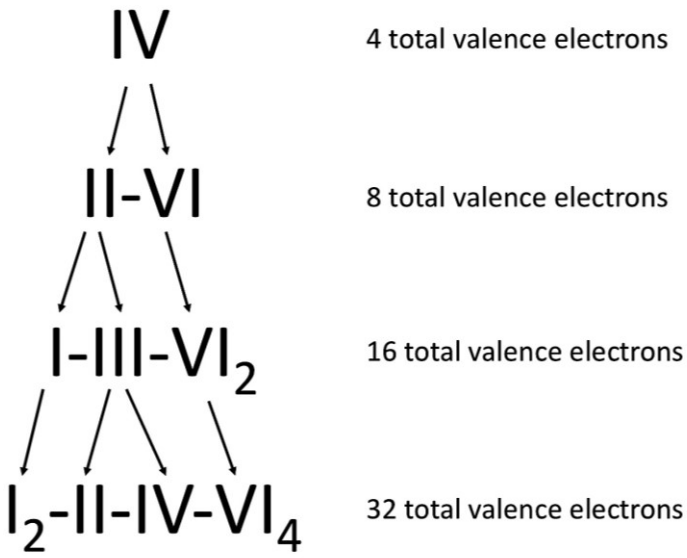

Figure 1.2: Cross substitution diagram for select normal tetrahedral DLSs.

1.1.4 Breaking Pauling's Second Rule

The need for further advancement of DLSs has led to interest in quaternary materials of the I_4-II-IV_2-VI_7 stoichiometry. To date, there are seven I_4-II-IV_2-VI_7 DLSs that have been reported in the literature, $Li_4MnGe_2S_7$ (*17*), $Li_4MnSn_2S_7$ (*17*), $Li_4HgGe_2S_7$ (*18*), $Ag_4HgGe_2S_7$ (*19*), $Ag_4CdGe_2S_7$ (*19*), $Cu_4NiSi_2S_7$ (*20*), and $Cu_4NiGe_2S_7$. (*20*) This dissertation presents two additional I_4-II-IV_2-VI_7 DLSs, $Cu_4MnGe_2S_7$ and $Cu_4CdSi_2S_7$. So far, all the I_4-II-IV_2-VI_7 DLSs have been found to crystallize in either the monoclinic space group C2 (*20*) or C*c* (*17-19*), with structures that are derived from cubic or hexagonal diamond, respectively. I_4-II-IV_2-VI_7 DLSs differ from

those of the I_2-II-IV-VI_4 stoichiometry in the local charge environment for some of the sulfide anions. (*17-20*) The I_4-II-VI_2-IV_7 DLSs of the C*c* space group, which are investigated in this work, consist of seven crystallographically unique sulfurs that are all on general positions. (*17-19*) The environment around four of these sulfurs anions are the same as those of I_2-II-IV-VI_4 DLSs and thus bonded to two monovalent, one divalent and one tetravalent cation; the other three sulfur anions consist of either three monovalent and one tetravalent cations or two monovalent and two tetravalent cations. (*17-20*) The later three sulfur anions break Pauling's second rule. (*6*) The positive local charge of these neighboring cations either under- or over-compensate for the charge of the anion. The breaking of Pauling's second rule results in slight distortions of the tetrahedral, shape as evidenced in the observed bond distance and angles. However, these distortions are small enough that the corner-sharing tetrahedral structure is maintained, and while Pauling's second rule is not followed locally, charge balancing is present within one unit cell. (*17-20*) This process creates an additional route to tuning the properties of DLSs through altering the stoichiometry.

1.2 Previous Work

Six structure types for quaternary DLSs have been discovered. The first I_2-II-IV-VI_4 DLS structure type was discovered by L.O. Brockway in 1934. (*21*) Brockway reported the DLS Cu_2FeSnS_4 (stannite) which crystallizes in the space group I-42*m*. (*21*) Two more structure types of normal I_2-II-IV-VI_4 DLSs were reported in 1969 by Pathé, Yvon and Deitch when they reported the structure of Cu_2CdGeS_4 and twenty other quaternary DLS, six of the I_2-II-IV-VI_4 general formula. (*22*) In their paper, Pathé, Yvon and Deitch describe the wurtz-stannite (P*mn*2_1) and wurtz-kesterite (P*n*) structure types. (*22*) To synthesize Cu_2CdGeS_4 Pathé, Yvon and Deitch used the same iodine vapor transport method as Nitsche, Sargent and Wild. (*23*) In the late 1960s and

early 1970s iodine vapor transport was a common crystallization technique used to synthesize new DLS compounds. (*23,24*) A fourth I_2-II-IV-VI_4 structure type was discovered in 1972, when West and Glasser described the lithium cobalt (II) silicate, Li_2CoSiO_4, structure type with the P*na*2_1 space group. (*25*) This structure type was later confirmed in 1979. (*26*) The kesterite (I-4) structure type was later discovered in 1978 by Hall, Szymanski and Stewart, who compared the kesterite structure to that of the stannite structure. (*27*) Lafond et. al. investigated Cu_2ZnSnS_4 and how dual occupancy of the Cu/Zn sites affected the structure. (*28*) Their work lead to the sixth structure type for normal I_2-II-IV-VI_4 DLSs, the disordered kesterite structure type, which crystalizes in the I-42*m* space group. (*28*)

In the 1960s and 1970s the concentration of materials chemistry was on the discovery of new materials, much like the first step of the MGI, but like the subsequent steps of the MGI the next steps for many scientist was to investigate the properties of DLSs. Cu_2ZnSnS_4 is one example of such a material. This material was first synthesized by Nitche et al. via iodine vapor transport, but was later studied as a candidate for next-generation solar cells. (*23,29-31*) The analogous Cu_2FeSnS_4 has also been investigated for its potential in photovoltaics, as its bandgap (reported in the range of 1.27-1.4 eV) and photocatalytic activity are both appropriate for solar cell absorber layers. (*32,33*) Cu_2CdGeS_4 has been investigated for its promising use in thermoelectrics as it is a p-type semiconductor with a bandgap of 2.05 eV, and a large thermal electro-motive force. (*34,35*) Li_2MnGeS_4 and Li_2CoSnS_4 have recently both been investigated for their NLO properties. (*36*) Brant et al. published that Li_2MnGeS_4 has a bandgap of 3.069 eV and wide regions of transparency and phase matchability. (*36*) Most notably, Li_2MnGeS_4 was discovered to exhibit a large LIDT of >16 GW/cm^2 at 1064 nm with a pulse width of 30 ps. (*36*)

The history of I_4-II-IV_2-VI_7 DLSs began with $Cu_4MnSi_2S_7$ and $Cu_4NiGe_2S_7$ which were investigated for their magnetic properties. (*20*) The crystal structures of $Ag_4HgGe_2S_7$ and $Ag_4CdGe_2S_7$ were published by Gulay et al., but the properties of these materials have not yet been assessed. (*17*) In 2013, $Li_4MnGe_2S_7$ and $Li_4MnSn_2S_7$ were investigated for their use as anode materials in lithium-ion batteries. (*18*) The specific capacities of $Li_4MnGe_2S_7$ and $Li_4MnSn_2S_7$ were measured to be 585 and 725 mAh/g, respectively, greater than commercially used graphite with a theoretical capacity of 372 mAh/g. (*18*) $Li_4HgGe_2S_7$ is the only I_4-II-IV_2-VI_7 DLS reported for which its NLO properties have been reported. (*19*) The bandgap of $Li_4HgGe_2S_7$ was assessed to be 2.75 eV, with a SHG 1.5x $AgGaS_2$ and an LIDT of 104 $MWcm^{-1}$ (wavelength = 2.09μm, pulse width =50 ns). (*19*)

1.3 Applications

As DLSs have evolved, their compositional flexibility has lent them to a variety of applications, making them marketable materials. Some of the more notable applications for DLSs include photovoltaics, thermoelectrics, photocatalysis, lithium-ion batteries, magnetoelectronics, and nonlinear optics.

Photovoltaics involve the production of electric current at a semiconductor junction. DLSs are used as either the n- or p-type semiconductors that create the junction in solar cells and serve as the absorber of sunlight. The most noteworthy compound DLS used in solar cells is $CuIn_{1-x}Ga_xS_2$ (CIGS). (*37*) Cu_2ZnSnS_4 (CZTS) is of interest as a candidate for the next generation of solar cells. (*29-31*)

Thermoelectric applications also utilize the junction between n- and p- type semiconductors allowing thermoelectrics to convert between heat and electricity. (*38*) The first

possible effect is called the Seebek effect during which a temperature gradient is applied to a thermoelectric junction and the material thus generates an electric current. (*38*) The second phenomenon in which the electric current passes through the thermoelectric junction and results in the production of heat at the other side of the material, is called the Peltier effect. (*38*) These effects make thermoelectric materials valuable for both power generation and solid-state cooling, respectively. (*38, 39*) Some DLSs that are under investigation for their potential use in thermoelectric applications include $AgInSe_2$, (*40*) Cu_2SnSe_3, (*41*) Cu_3SbSe_3, (*42*) and $Cu_2ZnGeSe_4$. (*43*)

Photocatalysis is the acceleration of a chemical reaction by light and is another area for which DLSs have been investigated. (*44*) Five DLSs, Cu_2ZnGeS_4, Cu_2ZnSnS_4, Ag_2ZnGeS_4, Ag_2ZnSnS_4 and Ag_2ZnSnS_4, have been investigated for their use as photocatalysts. (*44*) These DLSs have been used with a ruthenium cocatalyst to produce visible-light-induced hydrogen evolution from Na_2S and K_2SO_3 aqueous solutions. (*44*)

Solid-state lithium-ion batteries are of interest because they use solid-state electrolytes which are safer than the liquid electrolytes currently used in battery systems. A solid-state electrolyte is advantageous as it does not pose the issue of flammability, electrolyte leakage, electrolyte vaporization, or phase transitions at low temperature which are all challenges associated with liquid electrolytes. (*45,46*) For these reasons, lithium-containing DLSs have also drawn attention for their potential in lithium-ion batteries as some contain lithium ion channels required for these applications. (*17,47*)

Magnetoelectronic devices combine magnetic and electronic properties, usually by perturbing a change in the magnetic properties driven by an electric field. These applications include field sensors (*48-51*), energy harvesters (*48, 52-62*), and random access memory

(MeRAM). (*48,61,63,64*) These field sensor devices are ideal for power-line current detection. (*50*) Magnetoelectronic materials are also being investigated for their use as energy harvesters, in which the low fixed frequency magnetic noise in the environment is used to harvest energy which could then power devices without the need for bulky power supplies. (*48,52-62*) Advancements are also being made in MeRAM which could potentially result in the replacement of internal memory, external storage and flash memory that is currently limited to encoding information in only two logic states. (*48,61,63,64*)

The work in this dissertation targets materials that could potentially be used in applications and they will be discussed in greater detail in the following.

1.3.1 IR Nonlinear Optical Applications

As a matter of fact, every material is nonlinear as it manifests its NLO behavior with increasing interaction with light. However, it is important to develop novel NLO materials with a remarkable efficiency for practical NLO applications. In this regard, DLSs have found multiple uses as they can provide a means for wavelength conversion, optical amplification, and optical phase conjunction. There are two fields that frequently utilize NLO materials especially working the IR regime: the medical field and the military. The medical community employs NLO materials in devices for the diagnostics, monitor, and treatment of disease in patients. (*14*) The detection of diseases is one of the biggest challenges for the medical community, as several diseases cannot be detected until they are quite advanced. Also, invasive testing deters many patients from seeking treatment sooner. NLO devices for early disease detection exploit molecular spectroscopy in the range of 2-20 μm. (*14*) In the case of cystic fibrosis, those diagnosed with the disease are also frequently infected with bacteria which produce hydrogen cyanide (HCN). (*14*) The HCN are

excreted in exhaled breath; therefore, breath analysis is conducted on the patient and the HCN is detected via molecular spectroscopy on the exhaled breath. (*14*) The presence of HCN is so frequently seen in those who have cystic fibrosis that the breath analysis technique could save many from unnecessary invasive tissue sampling. (*14)* This method is also being utilized for the detection of lung cancer by the presence of alkanes and breast cancer by the excretion of formaldehyde. (*14*)

The military uses NLO materials for a variety of applications, including minimal risk training in which IR scene projectors are used for simulation training, missile testing and thermal detection. (*65-67*) Communication technology is another use for NLO materials, in which they are used for data storage, and laser communication with concealed submarines. (*68*) IR countermeasure systems are being used in planes to "jam" incoming missile IR guidance systems. Similar systems are being investigated for use on commercial flights, but would require improved durability, power and efficiency. (*69-71*) NLO materials have made laser radar possible for target acquisition, tracking and pointing. (*72,73*) Although these systems exist, there is still room for improvement as it would be optimal for them to operate at an eye-safe wavelength beyond 1.5 μm. (*72,73*) Laser weaponry may still exist only in science fiction movies, but lasers are being used to sense chemicals, specifically for stand-off detection of drugs and explosives at the parts per trillion level using IR spectroscopy. This technique takes advantage of chemical signatures in the fingerprint regions of the IR to identify such materials. (*74*) IR spectroscopy is already being employed for 2,4,6-trinitrotoluene (TNT) and cyclotrimethylenetrinitramine (RDX) detection, using broadly tunable (6-8 μm) $ZnGeP_2$ optical parametric oscillators. (*75*)

Other applications for which NLO materials are utilized are environmental processing including climate studies, wind profile analysis, and monitoring of atmospheric air and water

pollutants including chemicals such as methane, carbon monoxide, sulfur dioxide, ozone and nitric oxide. (*76-79*) Along with ecological applications, NLO materials are also used in industrial process control, and optical frequency metrology. (*80,81*)

1.4 Nonlinear Optics

NLO materials produce a change in the optical properties of materials when exposed to a strong electromagnetic field. This in turn results in the modification of the light field via light-matter interaction. An ideal NLO material for frequency conversion simultaneously optimizes many characteristics including, but not limited to, a noncentrosymmetric crystal structure, a high second harmonic coefficient, a wide transparency region, a high LIDT, high thermal stability, phase matchability, chemical stability and ease of crystal growth. (*82*) Simultaneous optimization of all these properties is difficult as many of them are interdependent and inversely related. For some compounds in this dissertation three of these properties have been evaluated, second harmonic generation (SHG), laser-induced damage threshold (LIDT) and crystal growth. A noncentrosymmetic crystal structure is observed for all the compounds discussed in this dissertation, as they are all DLSs and inherently have a noncentrosymmetric structure. The pursuit of DLSs to achieve new NLO devices, however, is not the only option for targeting noncentrosymmetric materials.

1.4.1 Targeting Nonlinear Optical Materials

Since this dissertation focuses on second-order NLO properties, NLO materials hereafter are considered noncentrosymmetric. NLO materials can be pursued by targeting acentric building blocks that may assemble into noncentrosymmetric structures. The utilization of this method to

create DLSs has been described in Section 1. The conceptualization of acentric blocks is also used by those who target second-order Jahn-Teller distortions, and borate $[BO_3]^{3-}$ units to create NLO materials that can produce SHG, although these options are not as reliable as the pursuit of DLSs.

At its very core, the Jahn-Teller effect is an electronic distortion of the vibrionic systems, that results in a physical distortion of the molecules. (*83-85*) To target the Jahn-Teller effect the metal centers of NLO materials are chosen from certain d-block transition metals. (*83-85*) The Jahn-Teller effect results in the unequal occupation of degenerate orbitals, and instability within the structure which is compensated for by physical distortions of the material to relieve the degeneracy. (*83-85*) Those targeting NLO materials through the Jahn-Teller effect utilize this distortion in shape to create acentric building blocks that they hope will pack noncentrosymmetrically.

Borates based on $[BO_3]^{3-}$ units exhibit SHG because of asymmetric electronic distribution on the distorted planar anions. (*14*) These distortions create π-delocalized building blocks due to the joining of BO_3 and BO_4 units. (*14*)

1.4.2 Second Harmonic Generation

SHG is one potential property of NLO materials in which a material that possesses SHG can interact with light of a specific wavelength and output a wavelength half that of the incident wavelength, and therefore, the frequency doubled. (*14,85, 86, 87*) Harmonic responses are a consequence of light entering a medium when the dielectric polarization of the medium responds nonlinearly to the electric field, E(t), of the incident light at time t and is described by the following equation: $P(t) = \varepsilon_o[\chi^{(1)}E(t) + \chi^{(2)}E^2(t) + \chi^{(3)}E^3(t)+..]$ in which ε_o is the vacuum dielectric constant and each $\chi^{(n)}$ term is the nth order susceptibility of the NLO material. (*14,85- 87*) The

SHG term is $\chi^{(2)}E^2(t)$, and is nonzero only when a crystal lacks an inversion symmetry. (*14,85-87*) A powder sample is measured by the Kurtz-Perry powder method in which the near-static value of $\chi^{(2)}$ is calculated by comparison to a reference; $\chi_S^{(2)} = \chi_R^{(2)}\left(\frac{I_S^{SHG}}{I_R^{SHG}}\right)^{1/2}$ where I_S^{SHG} and I_R^{SHG} are the experimentally measured SHG counts from the sample and the reference, respectively. (*88*)

1.4.3 Laser Induced Damage Threshold

Laser-induced damage threshold (LIDT) of a material is a measure of the laser intensity that a crystal can withstand before incurring damage. (*89,90*) When an NLO crystal is subjected to a laser pulse, the electrons within the material are excited due to a laser pulse, which creates the promotion of electrons from the valence band to the conduction band. (*89,90*) When the electrons collide with one another they produce heat. This heat is then dispersed throughout the crystal lattice. (*89,90*) Once the lattice can no longer disperse the heat, the crystal begins to incur damage which is observed by physical phenomena such as burning, melting or cracking. (*89,90*) This is typically assessed by viewing the sample under a light microscope and searching for plasma formation. When measurements on single crystals are not possible, the LIDT is measured on a powder sample by subjecting it to pulses of an incident laser at a specific wavelength. Damage to the powder sample can be defined as the point at which the SHG stops following the expected square fit law. This is done by plotting the measured SHG counts as a function of laser intensity and using the first few data points to fit the data with the square fit law; once the data begins to deviate from the square fit law the LIDT has been reached.

1.4.4 Future of IR-Nonlinear Optical Materials

To date, all the commercially available IR NLO materials are ternary DLSs. While ternary DLSs such as $AgGaS_2$, $AgGaSe_2$ (*12*) and $ZnGeP_2$ (*91*) are commercially used, they suffer from drawbacks. $AgGaS_2$ and $AgGaSe_2$ are limited by inadequate LIDT and multiphoton absorption effects (*92-94*), while $ZnGeP_2$ suffers from difficult crystal growth, multiphoton absorption and a low LIDT. (*94-96*) These drawbacks warrant the continued search for new DLSs with improved properties. Moving forward, there have been many new quaternary DLSs of the general formula I_2-II-IV-VI_4 that have been discovered, but have not yet made their way to industrial use. To further tune the properties of DLSs the future of NLO materials could be the discovery of new I_4-II-IV_2-VI_7 DLSs. There have also been several new NLO materials that have been discovered with impressive LIDT and moderate SHG which warrant further evaluation of the IR-NLO applications by testing additional properties on single crystals. Two such materials investigated in this dissertation are Li_2MnGeS_4 (*36*) and Cu_2ZnSiS_4. (*97*)

1.5 Crystal Growth Techniques

The growth of crystalline materials is almost as important as the properties of those materials when considering them for industrial use. A material can have the world's best NLO properties, but it is completely useless for nonlinear optics aside from an academic interest if it cannot be synthesized as large single crystals that can be cut. This is a point of disconnect between academia and industry. Researchers in academia tend to investigate new compounds as microcrystalline powders or small single crystals, while those in industry are interested in the properties of large (cm or larger) size single crystals. The work in this dissertation aims to bridge this gap by synthesizing millimeter-sized single crystals when possible. The synthesis of large

single crystals is important as certain properties, like thermal conductivity, transparency measured by laser calorimetry and refractive index, can only be measured on sizable single crystals. Additionally, the measured properties can also depend on the crystals orientation. To obtain sizable, different crystallization techniques have been employed in addition to high-temperature solid-state synthesis, including flux reactions, and iodine vapor transport.

1.5.1 Flux Reactions

High-temperature, solid-state reactions are generally used for the synthesis of inorganic materials, in which heating reactants to sufficiently high temperatures and dwelling for adequate time results in a stable state being reached. (*98*) Such reactions are favored, as they can yield up to 100% and are straight forward. (*98*) However, such synthetic routes are not always possible, depending on the melting points of the starting materials. Flux reactions can be utilized in some instances. This involves the addition of an excess of the flux component that is either inert "solvent" or a material that can be incorporated into the desired/final product of the reaction, and allows the reaction to occur at a lower temperature. (*98-100*) The molten "solvent" allows the starting materials to move within the melt to facilitate solid state diffusion. (*98-100*) The ideal flux material is one for which the excess flux can be removed at the completion of the reaction. (*98-100*) For that reason, the flux used for the lithium-containing compounds in this dissertation is a self-flux of Li_2S:S as the reactions already contain Li_2S and sulfur, and will interact with the reactants. Conveniently, Li_2S can later be removed from the reactions by washing with polar solvents, such as methanol. (*100*)

1.5.2 Iodine Vapor transport

Iodine vapor transport (IVT) is one type of chemical vapor transport used to grow single crystals. During this process, starting material and crystalline iodine are combined in a reaction vessel and sealed under vacuum. (*101,102*) To avoid a buildup of pressure, it is recommended that a maximum of 5 mg/cm^3 of iodine is added to the reaction. (*23*) Crystalline iodine can begin to sublimate at room temperature, so special care must be taken when flame sealing the reaction vessel, to prevent the iodine from escaping and/or building up unwanted pressure in the tube. This can be done by submerging the portion of the reaction vessel containing the iodine in liquid nitrogen during the sealing process. The sealed reaction vessel is then placed in a furnace in such a manner that a temperature gradient is formed between the two ends of the reaction vessel: more commonly the vessel is oriented so that the reactants are at the high-temperature zone. (*101,102*) It is preferable to do this in a multi-zone furnace to obtain good control over the temperature gradient, which should be at least 100 °C and is recommended not to exceed 300 °C. (*101,102*) As the vessel is heated, the iodine will sublimate and create a convection current between the high- and low-temperature ends of the reaction vessel. (*101,102*) The convection current transports reactants from the high-temperature zone to the low-temperature zone forming crystals upon deposit. (*101-104*) It is also theorized that rather than simply transporting the reactants via convention current, the reactants may bond with the iodine creating metal-iodine species at the high-temperature zone, which decompose and deposit the reactants in the low-temperature zone, where the deposition aids the growth of single crystals. (*101,102*) This process has been used to produce single crystals on the order of millimeter size in one or more dimensions, depending on the crystal habit and the size of the reaction vessel. (*101,102*) Many of the DLSs that have been made by IVT are copper-containing materials including Cu_2-II-IV-VI_4, where II = Zn, Cd, Fe, Mn,

Ni, Co, Hg, IV=Sn, Ge, Si and VI=S, Se. (*23*) IVT was used for the work presented in this dissertation as it is a relatively inexpensive and quick technique.

1.5.3 Bridgman Growth

The Bridgman growth method can be used to grow single crystals of centimeter size. This method produces a crystal from a melt by slowly freezing it as it passes through the high- to low-temperature zone. For the Bridgman growth method, pre-synthesized phase-pure material or thoroughly mixed reactants are combined in a cubicle that will not react with the starting materials. (*105*) These reaction vessels can be made of several types of materials, including fused-silica (*105*), graphite (*106-110*), carbon-coated fused-silica (*111,112*), pyrolytic boron nitride (*113*) and glassy carbon (*113*) to name a few. The reaction vessel is also traditionally tapered at the tip and curved to create a concave growth surface to restrict crystal growth to one crystal. (*105*) To grow the crystal, the reaction vessel is slowly passed through a temperature gradient created by either the movement of the reaction vessel or movement of the furnace. (*105*) The rate at which the reaction vessel moves through the temperature zones can range from 0.1-30 mm/hour. (*105*) While this technique was not employed in this dissertation work, it is a viable next step for many of the investigated materials. The Bridgman method is already being used for many commercially available DLSs including $LiInS_2$ (*106,107,113*), $LiInSe_2$ (*108-113*), $LiGaSe_2$ (*110*) and $LiGaTe_2$. (*110*)

1.6 Conclusions

The overarching goal of this research was to identify new candidate IR-NLO materials among quaternary I_2-II-IV-VI_4 and I_4-II-IV_2-VI_7 diamond-like semiconductors and study their

physicochemical properties as microcrystalline powders and large single crystal samples. Li_2MnGeS_4, $Cu_4MnGe_2S_7$, $Cu_2CdSi_2S_7$, Li_2ZnSiS_4 and Cu_2ZnSiS_4 were the targeted materials. This knowledge gained from the various characterization techniques was then used to assess if these compounds are commercially viable for IR-NLO applications, surpassing at least one of the desired properties of commercially available IR-NLO crystals. This was achieved through the following objectives:

1. Synthesized the proposed compounds as polycrystalline powder samples.
2. Analyzed the synthesized powders using X-ray powder diffraction, scanning electron microscopy (SEM) coupled with energy dispersive spectroscopy (EDS) and optical diffuse reflectance UV-vis-NIR spectroscopy. X-ray powder diffraction was used to assess the phase purity of the synthesized compounds. SEM and EDS were utilized to study the materials morphology and approximate elemental ratio. Optical diffuse reflectance spectroscopy allowed for the bandgap of the materials to be estimated.
3. Determined the optimal crystal growth conditions for the compounds using high temperature solid-state synthesis and iodine vapor transport.
4. Measured second harmonic generation (SHG) and laser-induced damage threshold (LIDT) on microcrystalline powders.
5. Compared, collectively, the properties of the proposed compounds that are important for IR-NLO applications to commercially available materials ($AgGaS_2$ and $AgGaSe_2$) in order to determine their commercial viability.

Table 1.2: Select properties of two commercially available DLS IR NLO materials $AgGaSe_2$ and $AgGaS_2$. (*114*)

	$AgGaSe_2$	$AgGaS_2$
Melting Point	998°C	1002 °C
Transparency Range	0.8-17 µm	0.5-11 µm
Phase Matchability	$\lambda \geq 3100$ nm	$\lambda \geq 1800$ nm
$\chi^{(2)}$	66 pm/V	36 pm/V
LIDT (incident λ, pulse width)	25 MW/cm^2* (2.05 µm, 50 ns)	10 MW/cm^2# (1.06 µm, 20 ns)

$*\lambda = 2.05\ \mu m, \tau = 50\ ns, \quad \#\lambda = 1.06\ \mu m, \tau = 20\ ns$

1.7 References

(1) Jones, R.O., *J. Phys.: Condens. Matter*, in press.

(2) Crick, F.; *What Mad Pursuit: A Personal View of Scientific Discovery*, Penguin, London, England, **1988**.

(3) MGI White Paper, https://www.nist.gov/mgi, (Accessed February 3, 2019)

(4) Parthé, E. *Crystal Chemistry of Tetrahedral Structures*, Gordon and Breach Science Publishing, New York, NY, **1964**.

(5) Goryunova, N.C., *The Chemistry of Diamond-like Semiconductors*, The MIT Press, Cambridge MA, **1964**.

(6) Pauling, L., *J. Am. Chem. Soc.*, **1929**, *51*, 1010-1026.

(7) Miessler, G.L.; Tarr, D.A., Inorganic Chemistry Fourth Edition, Pearson, Upper Saddle River, New Jersey, **2004**

(8) Sze, S.M.; Lee, M.K., *Semiconductor Devices Third Edition, John Wiley & Sons Inc.*, New York, NY, **2010**

(9) Leck, J.H., *Theory of semiconductor junction devices; a textbook for electrical and electronic engineers*, Pergamon Press Ltd., Headington Hill Hall, Oxford, **1967**

(10) West, A.R., *Basic Solid State Chemistry*, John Wiley & Sons, Great Britain, Chichester, **1988**.

(11) Eifler, A.; Riede, V.; Brückner, J.; Weise, S.; Krämer, V.; Lippold, G.; Schmitz, W.; Bente K.; Grill, W., *Jpn. J. Appl. Phys.*, **2000**, *39*, 279-281.

(12) Catella, G.C.; Burlage, D., *MRS Bull.*, **1998**, *23*, 28-36.

(13) Bhar, G.C.; Smith, R.C., *Phys Status Solidi*, **1972**, *13*, 157-168.

(14) Aitken, J.A.; Brant, J.A.; Clark, D.J.; Kim, Y.S.; Jang, J.I., *Nonlinear Optics: Fundamentals, Applications and Technological Advances*, Wilkins F. Ed.; Nova Science Publishers Inc., NY, **2014**.

(15) Jackson, A.G.; Ohmer, M.C.; LeClair, S.R., *Infrared Physics & Technology*, **1997**, *38*, 233-244.

(16) Gallais, L.; Douti, D.-B.; Commandré, M.; Batavičiūtė, G.; Pupka, E.; Ščiuka, M.; Smalakys, L.; Sirutkaitis, V.; Melninkaitis, A.; *J. Appl. Phys.* **2015**, *117*, 223103.

(17) Kaib, T.; Haddadpour, S.; Andersen, H.F.; Mayfofer, L.; Järvi, T.T.; Moseler, M.; Möller,K.-C.; Dehnen, S.; *Adv. Funct. Mater.*, **2013**, *23*, 5693-5699.

(18) Wu, K.; Yang, Z.; Pan, S., *Chem. Commun.*, **2017**, *53*, 3010-3013.

(19) Gulay, L.D.; Olekseyuk, I.D.; Parasyuk, O.V.; *J Alloys Compd*, **2002**, *340*, 157-166.

(20) Shäfer, W.; Scheunemann, K.; Nitsche, R., *Mat. Res. Bull.*, **1980**, *15*, 933-937.

(21) Brockway, L.O., *Z. Krist.,* **1934**, *89* 434–441.

(22) Parthé, E.; Yvon, K.; Deithch, R.H., *Acta Crystallogr.*, **1969**, *25*, 1164-1174.

(23) Nitsche, R.; Sargent, D.F.; Wild, P., *J. Cryst. Growth*, **1967**, *1*, 52-53.

(24) Schäfer, W.; Nitsche, R., *Mat. Res. Bull.*, **1974**, *9*, 645-654.

(25) West, A.R., Glasser, F.P., *J. Solid State Chem.*, **1972**, *4*, 20-28.

(26) Yamaguchi, H.; Akatsuka, K.; Setoguchi, M.; Takaki, Y., *Acta Cryst.*, **1979**, *B35*, 2680-2682.

(27) Hall, S.R.; Szymanski, J.T.; Stewart, J.M., *Can. Miner.*, **1978**, *16*, 131-137.

(28) Lafond, A.; Choubrac, I.; Guillot-Deudon, C.; Fertey, P.; Evain, M.; Jobic, S., *Acta, Cryst.*, **2014**, *B70*, 390-394.

(29) Mitzi, D.B.; Gunawan, O.; Todorov, T.K.; Wang, K.; Guha, S., *Solar Energy Materials & Solar Cells*, **2011**, *95*, 1421-1436.

(30) Fella, C.M.; Romanyuk, Y.E.; Tiawari, A.N., *Sol. Energ. Mat.*, **2013**, *119*, 276-277.

(31) Delbos, S., *EPJ Photovolt*, **2012**, *3*, 35004.

(32) Baláz, P.; Baláz, M.; Sayagués, M.J.; Eliyas, A.; Kostova, N.G.; Kanuchová, M.; Dutková, E.; Zorkovská, A., Crystals*,* **2017***, 7,* 367.

(33) Miao, X.; Chen, R.; Cheng, W., *Materials Letters*, **2017**, *193*, 183-186.

(34) Parasyuk, O.V.; Romanyuk, Y.E.; Olekseyuk, I.D., *J. Cryst. Growth*, **2005**, *275*, e159-e162.

(35) Davydyuk, G.Y.; Parasyuk, O.V.; Romanyuk, Y.E.; Semenyuk, S.A.; Zaremba, V.I.; Piskach, L.V.; Koziol, J.J.; Halka, V.O., *J. Alloys Compd.*, **2002**, *339*, 40-45.

(36) Brant, J.A.; Clark, D.J.; Kim, Y.S.; Jang, J.I.; Weiland, A.; Aitken, J.A., *Inorg. Chem.*, **2015**, *54*, 2809-2819.

(37) Ramanujam, J.; Singh, U.P., *Energy Environ. Sci.*, **2017**, *10*, 1306-1319.

(38) DiSalvo, F.J., *Science*, **1999**, *285*, 703-706.

(39) Chen, G.; Dresselhaus, M.S.; Dresselhaus, G.; Fleurial, J.P.; Caillat, T., *Int. Mater. Rev.*, **2003**, *48*, 45-66.

(40) Qui, P.; Qin, Y.; Zhang, Q.; Li, R.; Yang, J.; Song, Q.; Tang, Y.; Bai, S.; Shi, X.; Chen, L. *Adv, Sci. (Weinh)*, **2018**, 1700727.

(41) Fan, J.; Carrillo-Cabrera, W.; Akselrud, L.; Antonyshyn, I.; Chen, L.; Grin, Y., *Inorg. Chem.*, **2013**, *52*, 11067-11074.

(42) Wei, T.-R.; Wu, C.-F.; Sun, W.; Pan, Y.; Li, J.-F., *RSC Adv.*, **2015**, *5*, 42848.

(43) Ibáñez, M.; Zamani, R.; LaLonde, A.; Cadavid, D.; Li, W.; Shavel, A.; Arbiol, J.; Morante, J.R.; Gorsse, S.; Snyder, G.J.; Cabot, A., *J. Am. Chem. Soc.*, **2012**, *134*, 4060-4063.

(44) Tsuji, I.; Shimodaira, Y.; Kato, H.; Kobayashi, H.; Kudo, A., *Chem Mater.*, **2010**, *22*, 1402-1409.

(45) Takada, K., *Acta Mater.*, **2013**, *61*, 759-770.

(46) Knauth, P., *Solid State Ionics*, **2009**, *180*, 911-916.

(47) Brant, J.A.; Massi, D.M.; Holzwarth, N.A.W.; MacNeil, J.H.; Douvalis, A.P.; Bakas, T.; Martin, S.W.; Gross, M.D.; Aitken, J.A., *Chem. Mater.*, **2015**, *27*, 189-196.

(48) Cheng, Y.; Peng, B.; Hu, Z.; Zhou, Z.; Liu, M., *Physics Letters A*, **2018**, *382*, 3018-3025.

(49) Paluszek, et al., Magnetoelectric composites for medical application in: G. Srinivasan, S. Priya, M.X. Sun (Eds.), Composite Magnetoelectrics, **2015**.

(50) Bichurin, M.; Petrov, R.; Leontiev, V.; Semenov, G.; Sokolov, O., *Sensors*, **2017**, *17*, 1271.

(51) Le, M.-Q., Belhora, F.; Cornogolub, A.; Cottinet, P.-J.; Lebrun, L.; Hajjaji, A., *J. Appl. Phys.*, **2014**, *115*, 194193.

(52) Annapureddy, V.; *Adv. Energy Mater.*, **2016**, *6*

(53) Zhou, S.; *Appl. Phys Lett.*, **2015**, *106*, 093901.

(54) Han, N.; *Appl. Energy*, **2016**, *178*, 672-680.

(55) Naifar, S.; *Measurement*, **2017**, *106*, 251-263.

(56) Bian, I,;", *Sens, Actuators A Phys.*, **2009**, *150*, 207-211.

(57) Cho, K.-H.; *J. Appl. Phys.*, **2014**, *115*, 204108.

(58) Han, J.; *Appl. Phys. Lett.*, **2014**, *104*, 093901.

(59) Zhou, Y.; Apo, D.J.; Priya, S., *Appl. Phys. Lett.*, **2013**, *103*, 192909.

(60) Lasheras, A.; *Smart Mater. Struct.*, **2015**, *24*, 065024.

(61) Leung, C.M.; Li, J.; Viehland, D.; Zhuang, X., *J. Phys. D: Appl. Phys.*, **2018**, *51*, 263002.

(62) Joshi, V.K., *JESTECH*, **2016**, *19*, 1503-1513.

(63) Gajek, M.; *Nat. Mater.*, **2007**, *6*, 296.

(64) Yang, F.; *J. Phys. D. Appl. Phys.*, **2009**, *42*, 072004.

(65) Williams, O.M., *Infrared Phys, Techn.*, **1998**, *39*, 473-486.

(66) Richardson, M.A.; Coath, J.A., *Opt. Laser. Technol.*, **1998**, *30*, 137-140.

(67) Eckardt, R.C., *Proc. SPIE*, **1995**, *2469*, 132-140.

(68) Lu, W; Liu, L.; Sun, J.; Pan, W., *Opik*, **2008**, *119*, 388-394.

(69) Hopkins, F.K. *Opt. Photonics News*, **1998**, *9*, 32-38.

(70) Hecht, J. *Laser Focus World*, **2014**, *50*, 31-38.

(71) Knuteson, D.J.; Singh, N.B.; Kanner, G.; Berghmans, A.; Wagner, B.; Kahler, D.; McLaughlin, S.; Suhre, D.; Gottlieb, M, *J Cryst. Growth*, **2010**, *312*, 1114-1117.

(72) Miller, M.J.: Mott, A.G.; Ketchel, B.P., *Proc. SPIE*, **1998**, *3472*, 24-29.

(73) Zuclich, J.A.; Lund, D.J.; Stuck, B.E., *Health Phys.*, **2007**, *92*, 15-23.

(74) Clewes, R.J.; Howle, C.R.; Stothard D.J.M.; Dunn, M.H.; Robertson, G.; Miller, W.; Malcolm, G.; Maker, G.; Cox, R.; Williams, B.; Russell, M., *Proc. SPIE*, **2012**, *8456*, 85460X.

(75) Todd, M.W.; Provencal, R.A.; Owano, T.G.; Paldus, B.A.; Kachanov, A.; Vodopyanov, K.L.; Hunter, M.; Coy, S.L.; Steinfeld, J.I.; Arnold, J.T., *Appl. Phys. B*, **2002**, *75*, 367-376.

(76) Chatterjee, U., *Pramana-J. Phys.*, **2014**, *82*, 29-38.

(77) Vaicikauskas, V.; Kaucikas, M.; Swedas, V.; Kuprionis, Z., *Rev. Sci. Instrum.*, **2007**, *78*, 023106.

(78) Andreev, Yu. M.; Geiko, P.P.; Krekov, G.M., *Proc. SPIE*, **1991**, *1811*, 367-370.

(79) Sumpf, B.; Rehle, D.; Kelz, T.; Dronfeldt, H.-D., *Appl. Phys. B.*, **1998**, *67*, 369-373.

(80) Bamford, D.J.; Cook, D.J.; Sharpe, S.J.; Van Pelt, A.D., *Appl. Opt.*, **2007**, *46*, 3958-3968.

(81) Udem, T.; Holzwarth, R.; Hänsch, T.W., *Nature*, **2002**, *416*, 233-237.

(82) Ohmer, M.C.; Pandev, R., *MRS Bull*, **1998**, *23*, 16-20.

(83) Hargittai, M.; Hargeittai, I. *Struct. Chem.* **2009**, *20*, 537-540.

(84) Suresh, S.; Ramanand, A.; Jayararman, D.; Mani, P., *Rev. Adv. Mater. Sci.*, **2012**, *30*, 175-183.

(85) Matlack, K.H.; Kim, J.-Y.; Jacobs, L.J.; Qu, J., *Journal of Nondestructive Evaluation*, **2015**, *34*, 273.

(86) Suresh, S.; Ramanand, A.; Jayararman, D.; Mani, P., *Rev. Adv. Mater. Sci.*, **2012**, *30*, 175-183.

(87) New, G. *Introduction to Nonlinear Optics*, Cambridge University Press, New York, **2011**.

(88) Kurtz, S.K.; Perry, T.T.,", *J. Appl. Phys.* **1968**, *39*, 3798-3813.

(89) Manenkov, A.A., *Opt. Eng.*, **2014**, *53*, 010901.

(90) Yu, J.; Xiang, X.; He, S.; Yuan, X.; Zheng, W.; Lü, H.; Zu, X., *Adv in Cond Matter Phys*, **2014**, 364627.

(91) Schunemann, P.G.; Pollak, T.M., *MRS Bull.* **1998**, *23*, 23-27.

(92) Harasaki, A.; Kiyoshi, K., *Jpn. J. Appl. Phys.*, **1997**, *36*, 700-703.

(93) Bhar, G.C.; Smith, R.C., *Phys. Stat. Sol.*, **1972**, *13*, 157-168.

(94) Wood, R.M. *Laser-induced Damage in Optical Materials*, Hilger, Boston, **1986**.

(95) Giles, N.C.; Bai, L.; Chirila, M.M.; Garces, N.Y.; Stevens, K.T.; Schunemann, P.G.; Setzler, S.D.; Pollak, T.M., *J. Appl. Phys.*, **2003**, *93*, 8975.

(96) Boyd, G.D.; Buehler, E.; Storz, F.G., *Appl. Phys. Lett.*, **1971**, *18*, 301-304.

(97) Rosmus, K.A.; Brant, J.A.; Wisneski, S.D.; Clark, D.J.; Kim, Y.S.; Jang, J.I.; Brunetta, C.D.; Zhang, J.-H.; Srnec, M.N.; Aitken, J.A., *Inorg. Chem.*, **2014**, *53*, 7809-7811.

(98) Poser, J.D.; Meyer, H.-J., *Z. Anorg. Allg. Chem.*, **2012**, *638*, 1293-1296.

(99) Sutorik, A.C.; Kanatzidis, M.G., *Chem. Mater.*, **1997**, *9*, 387-398.

(100) Kanatzidis, M.G.; Pöttgen, R.; Jeitschko, W., *Angew, Chem. Int. Ed.*, **2005**, *44*, 6996-7023.

(101) Schäfer, H., *Chemical Transport Reactions*, Academic Press, NY, USA, **1964**.

(102) Faktor, M.M; Garrett, I., *Growth of Crystals from Vapor*, Chapman and Hall Ltd., London, UK, **1974**.

(103) Zuo, R.; Wang, W. *J. Cryst. Growth* **2002**, *236*, 687-694.

(104) Zuo, R.; Wang, W. *J. Cryst. Growth* **2002**, *236*, 695-710.

(105) Capper, P., *Bulk Crystal Growth: Methods and materials.* Springer Handbook of Electrinic and Photonic Materials. Springer Handbooks, Springer, Cham, **2017**.

(106) Wang, S.; Gao, Z.; Zhang, X.; Zhang, X.; Li, C.; Dong, C.; Lu, Q.; Zhao, M.; Tao, X., *Cryst. Growth Des.*, **2014**, *14*, 5957-5961

(107) Kamijoh, T.; Kuriyama, K., *J. Cryst. Growth*, **1979**, *46*, 801-803.

(108) Jia, N.; Wang, S.; Gao, Z.; Wu, Q.; Li, C.; Zhang, X.; Yu, T.T.; Lu, Q.; Tao, X., *Cryst. Growth Des.*, **2017**, *17*, 5875-5880.

(109) Vijayakumar, P.; Magesh, M.; Arunkumar, A.; Babu, G.A.; Ramasamy, P.; Abhaya, S., *J. Cryst. Growth*, **2014**, *388*, 17-21.

(110) Tupitsyn, E.; Bhattacharya, P.; Rowe, E.; Matei, L.; Cui, Y.; Buliga, V.; Groza, M.; Wiggins, B.; Burger, A.; Stowe, A.,", *J. Cryst. Growth*, **2014**, *393*, 23-27.

(111) Guo, L.; Xu, Y.; Zheng, H.; Wue, W.; Dong, J.; Zhang, B.; He, Y.; Zha, G.; Chung, D.Y.; Jie, W.; Kanatzidis, M., *Cryst. Growth Des.*, **2018**, *18*, 2864-2870.

(112) Wang, S.; Zhang, X.; Zhang, X.; Li, C.; Gao, Z.; Lu, Q.; Tao, X., *J. Cryst. Growth*, **2014**, *410*, 150-155.

(113) Magesh, M.; Arunkumar, A.; Vihayakumar, P.; Babu, G.A.; Ramasamy, P., *Opt. Laser Technol.*, **2014**, *56*, 177-181.

(114) Eksma Optics, http://eskmaoptics.com/out/media/IR.pdf (Accessed March 9, 2019)

Chapter 2: Synthesis and Magnetic Properties of Li_2MnGeS_4 Single Crystals Grown via Iodine Vapor Transport

2.1 Introduction

Diamond-like semiconductors (DLSs) are useful in a variety of applications due to their attractive physicochemical properties. DLSs are currently commercially available for use in infrared nonlinear optical (IR-NLO) applications (*1-6*), solar cells (*7-11*) and LEDs (*12-15*). They are considered promising thermoelectric (*16-19*), and magnetoelectronic materials (*20-22*) as well as solid-state electrolytes for lithium-ion batteries (*23*). Recently, there has been a movement towards generating smaller and more compact devices, requiring materials to be prepared as either thin films or nanoparticles, although sizable single crystals are still vital in several fields, including nonlinear optics. More importantly, the preparation of pure, single crystals is paramount for studying a material's intrinsic properties without influence from secondary phases and grain boundaries.

Magnetic properties are relevant for quaternary DLSs of the formula I_2-II-IV-VI_4, when the II element is a magnetic ion. The magnetic properties of several quaternary DLSs have been reported, including those that are antiferromagnetic (*24-32*), ferrimagnetic (*29,32*) and ferromagnetic (*33*). The discovery of new magnetic materials is of interest in the quest for new spintronic devices (*34-37*). The issues encountered for these materials are that magnetic measurements can be complicated by the presence of polymorphs and are very sensitive to secondary phases, which in some cases can dominate the magnetic response (*32,38-41*). It is, therefore, preferable to collect magnetization data from single crystals.

From very small single crystals of <0.2 mm on an edge, it was previously found that Li_2MnGeS_4 crystallizes in the noncentrosymmetric orthorhombic space group $Pna2_1$ with the

lithium cobalt (II) silicate structure type that is derived from lonsdaleite. From a polycrystalline sample that was deemed to be ~97% phase pure, it was determined that Li_2MnGeS_4 is an outstanding candidate for IR-NLO applications due to several favorable attributes. (*42,43,44*) Magnetic measurements of Li_2MnGeS_4 were previously precluded by the presence of a secondary phase, Mn_2GeS_4 (*45*), in the powder samples. To further investigate the properties of this material, sizeable single crystals were warranted.

Our attention was drawn to iodine vapor transport (IVT) to produce crystals of Li_2MnGeS_4 because this method has been successful for the preparation of many quaternary DLSs dating back to the 1970s. (*28,46,47*) Some quaternary DLSs made via IVT include Cu_2-II-IV-VI_4, where II = Zn, Cd, Fe, Mn, Ni, Co, Hg, IV=Sn, Ge, Si and VI=S, Se. (*28,46,47*) To the best of our knowledge, IVT has not been reported for the preparation of lithium-containing DLSs. In fact, we have not been able to find any literature describing the use of IVT to prepare any lithium-containing chalcogenides. Large single crystals of lithium-containing DLSs, such as $LiInS_2$ (*48-50*), $LiInSe_2$ (*51-55*), $LiGaSe_2$ (*56*), and $LiGaTe_2$ (*56*), are typically grown via the Bridgman method. This method allows the starting materials to be housed in a reaction vessel, typically graphite (*48-56*) carbon-coated quartz (*52,54*), pyrolytic boron nitride (*55*), or glassy carbon (*55*), which will not react with lithium. One reason that IVT might not have been reported as a synthetic route for lithium-containing DLSs is that lithium can react with the fused-silica reaction vessel, due to its rather high oxophilicity. What makes IVT more challenging than Bridgman growth is that the entire reaction vessel must be protected when using oxophilic materials. This issue has been rectified in our work by using a homemade, graphite-tube containment system that spans the entire length of the reaction vessel. These reactions produced sizable (2 x 1 x 1 mm^3) single crystals of Li_2MnGeS_4 that were used for magnetic studies and specific heat measurements. Single crystals

were confirmed by collecting procession images using a single crystal X-ray diffractometer, while energy dispersive spectroscopy (EDS) and X-ray powder diffraction (XRPD) were utilized to verify the stoichiometry and phase purity of the product, respectively.

2.2 Materials and Methods

2.2.1 Synthesis via Iodine Vapor Transport

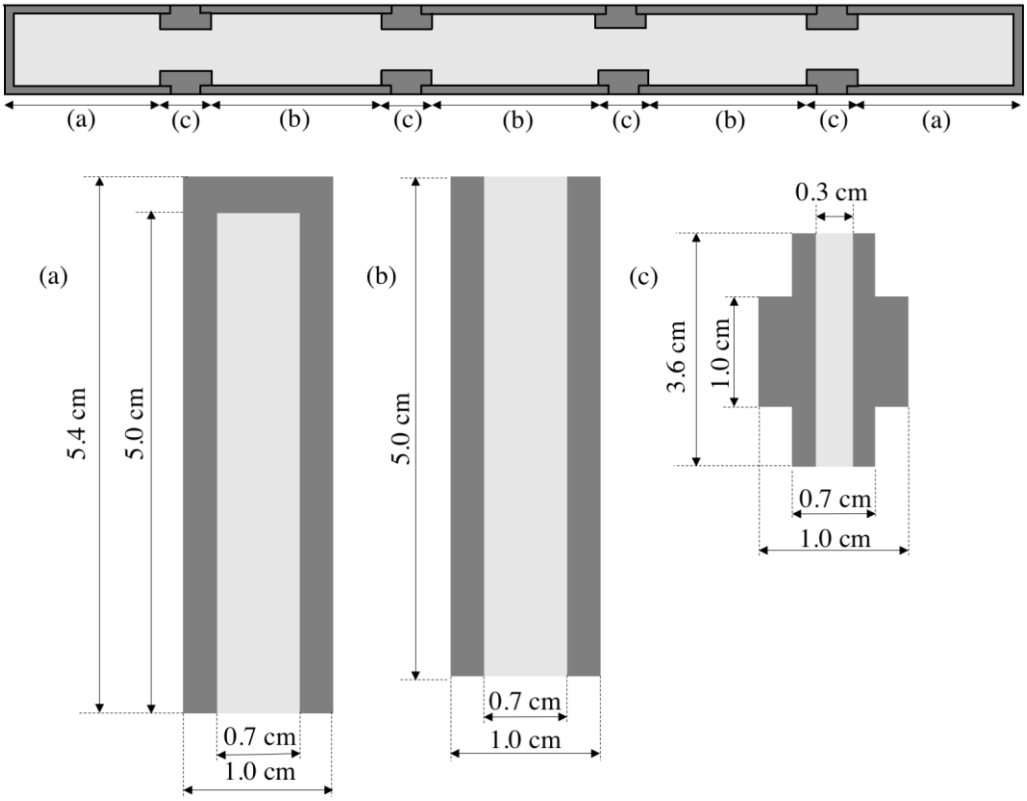

Figure 2.1: (Top) Entire graphite-tube containment system indicating the endcaps, expansion pieces and connectors, labelled a, b and c, respectively. (Bottom) Expanded views with dimensions of each piece of the containment system (a) endcap, (b) expansion piece, and (c) connector.

Sizable single crystals were prepared through IVT in a unique, graphite-tube containment system. The containment system consisted of two endcaps, three expansion pieces and four connectors. Figure 2.1 displays a technical schematic of the containment system and each individual piece. The endcaps, expander pieces and connectors were machined from solid graphite rods with an outer diameter of 1.0 cm (NAC-500 fine-grain, high-density extruded graphite rods

from NAC Carbon Products, Inc.). A containment system with multiple connectors was chosen for two reasons. There were limitations in the machining process, as a drill bit long enough to mill a 33.0 cm long graphite tube was not available and attempts to create a graphite tube longer than 5.0 cm resulted in cracking of the rod. Secondly, using multiple connectors allows for easy extraction of the crystals. Most IVT reactions are carried out in fused-silica tubes, which can be cleanly cut to extract the crystals, but this is not a preferred procedure for graphite tubes, which typically produce graphite dust and small fragments when they are broken. The crystals used for the analyses were harvested from the high-temperature end of the reaction vessel.

The reactions were prepared by weighing powders of Li_2S (1.2 mmol, 98%, 99.9% Li, Strem), Mn (1 mmol, chips were ground using a diamonite mortar and pestle, 99.8%, Alfa Aesar), Ge (1 mmol, pieces were ground using a diamonite mortar and pestle, 99.999%, Strem) and S (3 mmol, sublimed powder, 99.5% Fisher Scientific). The reagents were combined and ground for 10 minutes in an agate mortar and pestle and funneled into one of the end caps, along with 5 mg/cm^3 of crystalline I_2 (~0.0581 g, Alfa Aesar). The pieces of the graphite-tube containment system were assembled to a length of 33 cm. The graphite-tube containment system was housed in a 12 mm o.d. fused-silica tube that was flame-sealed under a vacuum of 10^{-4} mbar to a length of approximately 36 cm. During flame sealing, the bottom of the reaction vessel was submerged in liquid nitrogen, to ensure that the iodine did not sublimate.

The sealed reaction vessel was heated in a programmable, two-zone, high-temperature tube furnace. A two-zone furnace was used to allow for control of the temperature gradient between the high- and low- temperature zones. The high-temperature zone of the furnace was programed to heat to 800 °C in 13.5 hours, dwell at 800 °C for 144 hours, and cool to 750 °C at a rate of 1 °C/hour, after which the zone was cooled ambiently. The low-temperature zone was programed to

heat to 500 °C in 13.5 hours, dwell for 144 hours, and cool to 450 °C at a rate of 1 °C/hour, after which the zone was cooled ambiently.

Upon completion of the heating program, the resulting crystals were extracted from the graphite tube by soaking it in methanol. This process detached the crystals from the graphite tube and dissolved any excess Li_2S. A second washing with hexane removed any I_2 present on the surface of the crystals.

2.2.2 Single Crystal X-ray Diffraction

Procession images were collected using a Bruker SMART Apex 2 CCD single-crystal X-ray diffractometer with graphite-monochromatized Mo-K_α radiation using a tube power of 50 kV and 30 mA. The data used to produce the procession images were collected from 20 second frames over a range of 3.1-27.5° theta.

2.2.3 Scanning Electron Microscopy (SEM) and Energy Dispersive Spectroscopy (EDS)

The morphology of the single crystals was investigated by means of SEM. Crystals were adhered to an aluminum specimen stub using conductive carbon tape. A Hitachi S-3400N scanning electron microscope was utilized to collect the micrographs. The working distance was 10 mm, the filament current was 85 kV and the probe current was 80 kV. The micrographs were obtained using an accelerating voltage of 5 kV; however, the accelerating voltage was set to 15 kV for EDS. A Bruker Quantax model 400 energy dispersive spectrometer equipped with a XFlash 5010 EDS detector having a resolution of 129 eV was used to assess an approximate elemental ratio and obtain elemental maps of the crystals. The EDS spectra were amassed using a three-minute live time, and the elemental mapping was accomplished using a fifteen-minute live time. The EDS data

were normalized using the equation, $\textbf{Normalized Ratio} = \frac{\left(\frac{\text{Wt\% Element}}{\text{Mass Element}}\right)}{\left(\frac{\text{Wt\% Manganese}}{\text{Mass Manganese}}\right)}$, and the error was calculated using the equation, $\textbf{Error} = \left(\frac{\text{Wt\%}}{\text{Mass}}\right)\sqrt{\left(\frac{\text{Wt\% Error}}{\text{Wt\%}}\right)^2 + \left(\frac{\text{Mass Error}}{\text{Mass}}\right)^2}$.

2.2.4 Magnetization and Specific Heat Measurements

The DC magnetization measurements on a single crystal of Li_2MnGeS_4 were carried out in a magnetic field up to 9 T on a Quantum Design Physical Property Measurement System (PPMS) with the Vibrating Sample Magnetometer (VSM) attachment. The specific heat of the crystal was measured by the thermal-relaxation calorimeter of the PPMS using the two-τ model.

2.3 Results and Discussion

2.3.1 Iodine Vapor Transport Synthesis

The development of this process was carried out by trial and error due to the absence of literature on applying IVT to the synthesis of lithium-containing DLSs. Although we know lithium metal to be highly oxophilic, initial IVT reactions were carried out in fused-silica tubes using enough binary and elemental starting materials to obtain 1 mmol of product, 5 mg/cm^3 of crystalline iodine and a temperature gradient of 100 °C. (*46*) Fused-silica was used because it was thought that the lithium might not react with it during IVT, as presumably lithium iodine species may form first. (*57-60*) These reactions resulted in severe damage to the reaction vessel. In subsequent reactions, half the length of the fused-silica reaction vessel was carbon-coated by pyrolyzing acetone, leaving a clean section of tubing for proper sealing. The carbon-coated section was kept at the high-temperature zone, where the lithium was expected to be more reactive. This

also proved unsuccessful, as the entire tube incurred damage, which made evident the necessity for a fully protected vessel. The graphite-tube containment system was created to solve this problem, Figure 2.1.

Other variables such as temperature gradient between zones, the amount of reactants and the amount of I_2 were adjusted, in addition to the graphite-tube containment system length, until the optimal conditions were determined. Reactions in which the containment system length was less than 33 cm produced no transport and the products were binary and/or ternary compounds; Li_2MnGeS_4 was not present. Little transport occurred and the products were microcrystalline powders when $\Delta T < 250°C$. Next in an effort to obtain better transport and larger single crystals, the starting materials were halved. This resulted in transport of the materials, but unfortunately it did not produce any sizable single crystals; crystals less than 1 mm^3 were harvested. Further endeavors to increase transport and crystal size included changing the amount of I_2, up to a maximum of 10 mg/cm^3, which also increased transport; however, this change still did not result in crystals of sufficient size. Adjusting both the quantity of reactants and the I_2 resulted in more transport, but the resulting crystals were still less than 1 mm^3. The key to making sizable crystals by IVT was the increase of the tube length to 33 cm in combination with a ΔT of 300 °C. These optimized reaction parameters, as described in Section 2.1, resulted in single crystals with dimensions of approximately 2 x 1 x 1 mm^3, Figure 2.2.

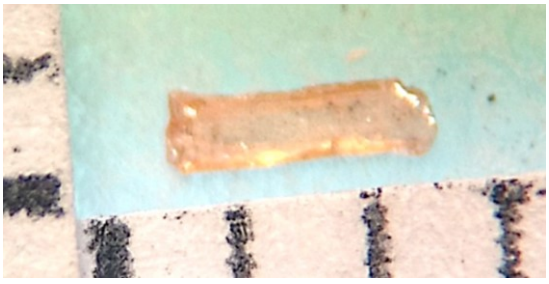

Figure 2.2: Digital image of a Li_2MnGeS_4 single crystal produced from the optimized IVT reaction against a millimeter scale.

2.3.2 Crystallinity and Phase Purity

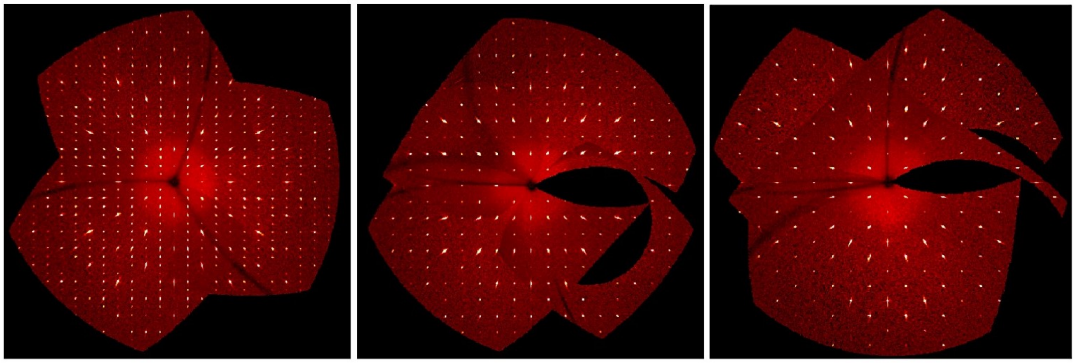

Figure 2.3: Procession images obtained for a Li_2MnGeS_4 single crystal.

To confirm that the as-obtained samples were single crystals, procession images were collected with a single crystal X-ray diffractometer. It can be seen in Figure 2.3 that the observed reflections (bright spots) are aligned in rows for each plane and the lack of additional spots between the clear lines indicates that the crystal is indeed a single crystal. Preliminary unit cell analysis indicated a primitive, orthorhombic unit cell with dimensions that agreed well with those previously reported for Li_2MnGeS_4. (*43*)

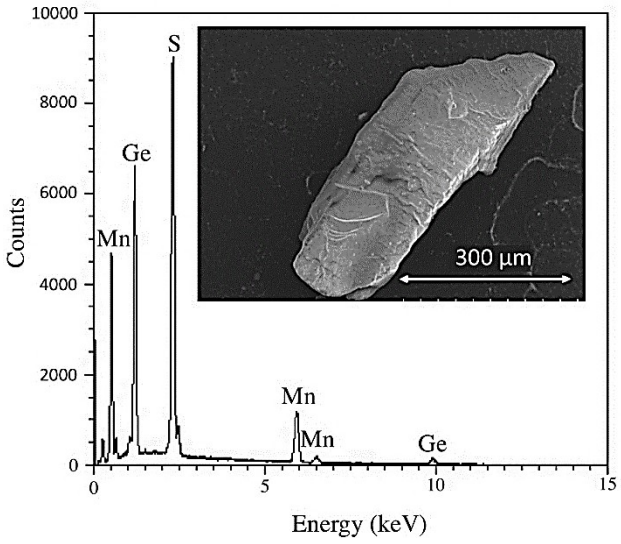

Figure 2.4: EDS spectrum of Li_2MnGeS_4 with the inlayed SEM micrograph of the crystal.

2.3.3 Morphology and Composition

The SEM micrographs demonstrate that Li_2MnGeS_4 crystalizes as relatively smooth rectangular crystals, displayed in the inlay of Figure 2.4. The EDS spectrum indicates that the crystals contained manganese, germanium and sulfur in approximately the expected ratios, Figure 2.4. Lithium cannot be identified by EDS

due to restrictions of the technique. The weight percentages obtained from the analysis are 40.30%, 23.88%, and 34.21% for manganese, germanium and sulfur respectively. The remaining 1.61% is carbon from the carbon tape. Assuming one equivalent of manganese per formula unit, the formula $Li_xMn_{1.000(3)}Ge_{1.335(6)}S_{3.43(1)}$ was calculated. While EDS is a semi-quantitative technique, more accurate results can be obtained by inductively coupled plasma optical emission spectrometry (ICP-OES). In previous work, Brant et. al. confirmed the stoichiometry of the crystals, including the lithium content, using ICP-OES. (*43*)

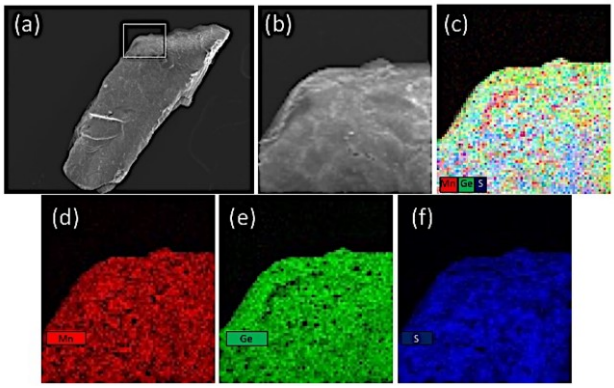

Figure 2.5: (a) SEM micrograph of mapped crystal highlighting the mapped area of 7200 μm^3. (b) SEM close-up of the mapped area. (c) Overlay of the mapping of Mn (red), Ge (green), S (blue). (d,e,f) Elemental mapping of Mn, Ge and S, respectively.

EDS mapping was utilized to assess the distribution of the elements in the crystal. The overlay of the elemental maps demonstrates even distribution of the elements indicating that the composition of the crystal is homogeneous, Figure 2.5.

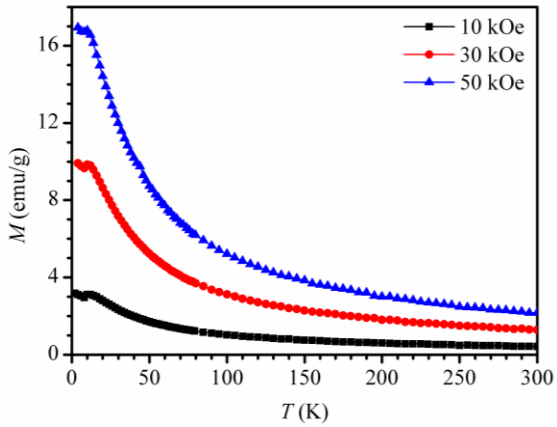

Figure 2.6: Magnetization as a function of temperature for Li_2MnGeS_4 under ZFC mode at field strengths of 10, 30 and 50 kOe displayed in black, red and blue respectively.

2.3.4 Magnetism

To determine the magnetic properties of Li_2MnGeS_4, the magnetization was measured as a function of temperature under zero-field-cooling (ZFC) mode from 10 kOe to 50 kOe, Figure 2.6. Similar behavior is observed for the measurements taken under various magnetic field strengths. Therefore, from this point on, our discussion will

be exclusive to the data obtained using a field strength of 10 kOe, Figure 2.7. The curve for the magnetization as a function of temperature (M-T curve), indicates that this material is antiferromagnetic at low temperature, due to the small positive susceptibility below the critical temperature, the Néel temperature, T_N. It responds as a paramagnetic material above the critical temperature, because the susceptibility decreases with increasing temperature. (*61,62*) The cusp at 10 K corresponds to the T_N of Li_2MnGeS_4. The inverse magnetic susceptibility as a function of temperature was plotted and used to calculate the Weiss temperature (θ) of -35 K by fitting the paramagnetic region from 30 to 300 K with the Curie-Weiss law. (*61,62*) The negative Weiss temperature suggests that the interactions between Mn^{2+} ions are weakly antiferromagnetic. The effective magnetic moment of the Mn^{2+} ions (μ_{Mn}) was determined to be 5.6 μ_B , close to the theoretical value for Mn^{2+} ions, 5.9 μ_B. (*63*) The differences in the magnetization versus temperature curves for the ZFC and field-cooling conditions at 10 kOe are negligible.

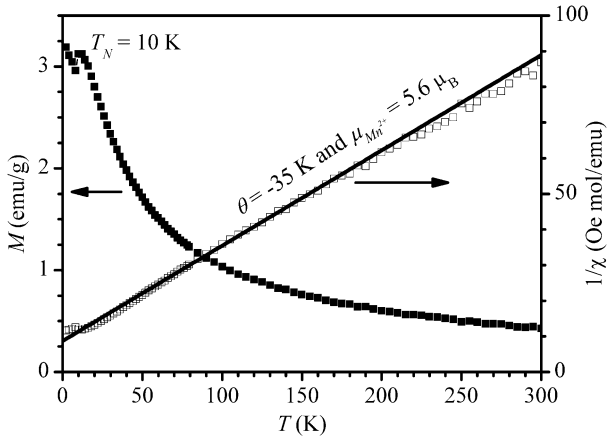

Figure 2.7: (Left) Magnetization as a function of temperature for Li_2MnGeS_4. (Right) Inverse magnetic susceptibility as a function of temperature for Li_2MnGeS_4.

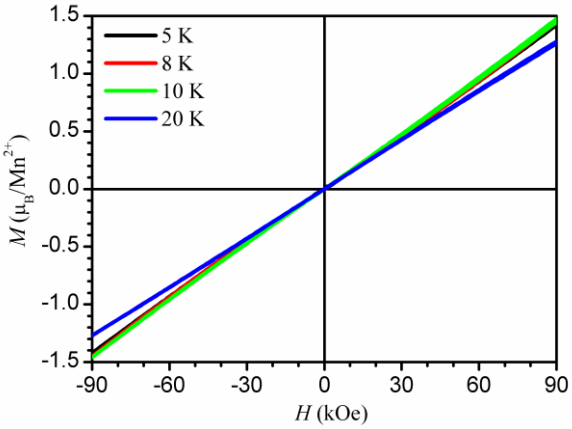

Figure 2.8: Magnetization versus field curve for Li_2MnGeS_4 at 5 K, 8 K, 10 K and 20 K in black, red, green and blue respectively.

The magnetization versus field curve for Li_2MnGeS_4 is presented in Figure 2.8. Below the T_N, antiferromagnetic ordering is demonstrated as evident by the linear behavior with a positive

Table 2.1: Magnetic properties for select I_2-II-IV-VI_4 DLSs.

I_2-II-IV-VI_4 DLS	Ordering Temperature	Ordering Type	Reference
$Li_2MnSnSe_4$	8.6 K	antiferromagnetic	*24*
Li_2MnGeS_4	10 K	antiferromagnetic	this work
Li_2FeGeS_4	~6.0 K	antiferromagnetic	*31*
Li_2FeSnS_4	~4.0 K	antiferromagnetic	*31*
$Cu_2MnSiSe_4$	9 K	antiferromagnetic	*32*
$Cu_2MnSiTe_4$**	22 K 36 K	antiferromagnetic antiferromagnetic	*32* *32*
Cu_2MnGeS_4	8.25-10 K	antiferromagnetic	*20,32,33,66*
$Cu_2MnGeSe_4$	11 K	antiferromagnetic	*32*
$Cu_2MnGeTe_4$**	33 K 130 K	antiferromagnetic, ferrimagnetic	*32* *32*
Cu_2MnSnS_4	8.8 K	antiferromagnetic	*25*
$Cu_2MnSnSe_4$**	13 K 24 K	antiferromagnetic ferromagnetic	*32* *33*
$Cu_2MnSnTe_4$**	148 K ~250 K	ferrimagnetic ferrimagnetic	*32* *32*
Cu_2FeGeS_4	12.0 K	antiferromagnetic	*28*
$Cu_2FeGeSe_4$	20.0 K	antiferromagnetic	*29*
$Cu_2FeGeTe_4$*	160.1 K	ferrimagnetic	*29*
Cu_2FeSnS_4	6.1 K	antiferromagnetic	*26*
$Cu_2FeSnSe_4$	19.0 K	antiferromagnetic	*27*
$Ag_2MnSiSe_4$	65 K	ferrimagnetic	*32*
$Ag_2MnSiTe_4$**	80 K 155 K	ferrimagnetic ferrimagnetic	*32* *32*
$Ag_2MnGeSe_4$	64 K	ferrimagnetic	*32*
$Ag_2MnGeTe_4$**	90 K 191 K	ferrimagnetic ferrimagnetic	*32* *32*
Ag_2MnSnS_4	8.8 K	antiferromagnetic	*30*
$Ag_2MnSnSe_4$**	10 K 92 K	antiferromagnetic ferrimagnetic	*32* *32*
$Ag_2MnSnTe_4$**	110 K 99 K	ferrimagnetic ferrimagnetic	*32* *32*

* Secondary phases were noted as being present

slope at 5 K, 8 K, and 10 K. (*61,62*) The retention of a positive linear slope at 20 K indicates the material is paramagnetic above the T_N. (*61,62*) From the plot in Figure 2.8, the magnetic moment of the Mn^{2+} ions is determined to be ~1.45 μ_B under a field of 90 kOe, remarkably smaller than the expected value, due to being far from magnetic saturation.

The compositionally similar DLS, Cu_2MnGeS_4 crystallizes in a different space group, $Pmn2_1$, and adopts the wurtz-stannite structure type. (*64*, *65*) In comparison, Cu_2MnGeS_4 is also antiferromagnetic below its Néel temperature, with T_N in the range of 8.25 K to 10 K, and the corresponding magnetic moment has been reported in the range of 5.83-5.90 μ_B. (*20,33,66*) The similarity of these results suggests that changing the monovalent ion in the DLS formula, I_2-II-IV-VI_4, does not have a significant effect on the magnetic properties. While Li_2MnGeS_4 and Cu_2MnGeS_4 crystalize in different space groups, the Mn-Mn distance is approximately 5.4 Å for both. (*43,64*) Cu_2FeSnS_4 (*67*) and Li_2FeGeS_4 (*68*) are of the stannite and wurtz-kesterite structure types, respectively, have similar distances between magnetic ions and are also antiferromagnetic with T_N ~6 K. Table 2.1 lists several quaternary DLSs of the formula I_2-II-IV-VI_4 that also contain magnetic ions. Antiferromagnetism with relatively low T_N are the most commonly observed magnetic properties for these types of materials.

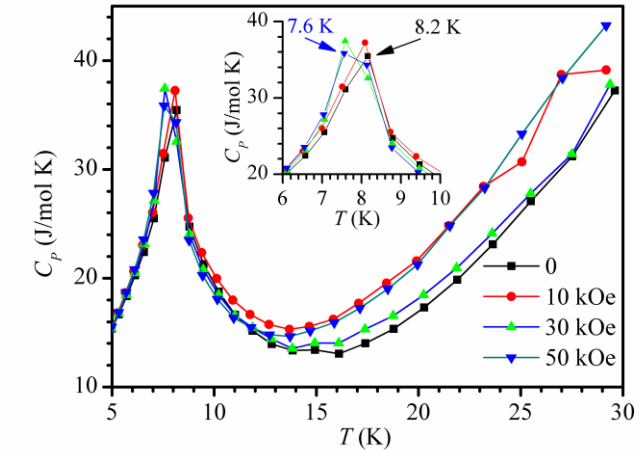

Figure 2.9: Specific heat as a function of temperature for Li_2MnGeS_4 under fields of 0 kOe to 50 kOe with a close-up of the specific heat as a function of temperature around the Néel temperature.

2.3.5 Specific Heat

The specific heat (C_p) as a function of temperature was measured under magnetic fields of 0-50 kOe, Figure 2.9. As the field strength increases from 0 to 50 kOe, T_N decreases. The low T_N suggests a weak magnetic coupling between Mn^{2+} ions, which can be shifted by an external magnetic field, from a T_N of 8.2 K at 0 kOe to a T_N of 7.6 K at 50 kOe.

Above the T_N, the specific heat can be considered as the sum of the electronic (C_e), lattice (C_{latt}) and magnetic (C_{mag}) specific heats by; $\mathbf{C_P = C_e + C_{latt} + C_{PM} = \gamma T + \beta T^3 + \sigma T^{-2}}$, where T is temperature, and $\boldsymbol{\gamma, \beta}$ **and** $\boldsymbol{\sigma}$ denote the electronic, lattice and paramagnetic coefficients, respectively. The fit of the data from 9-30 K yielded $\boldsymbol{\gamma}$ = 0.11 J/molK^2, $\boldsymbol{\beta}$ = 0.00126 J/molK^4 and $\boldsymbol{\sigma}$ = 1710 JK/mol, allowing for the separation of the magnetic specific heat from the electronic, lattice and the total specific heats, as illustrated by the plot in Figure 2.10.

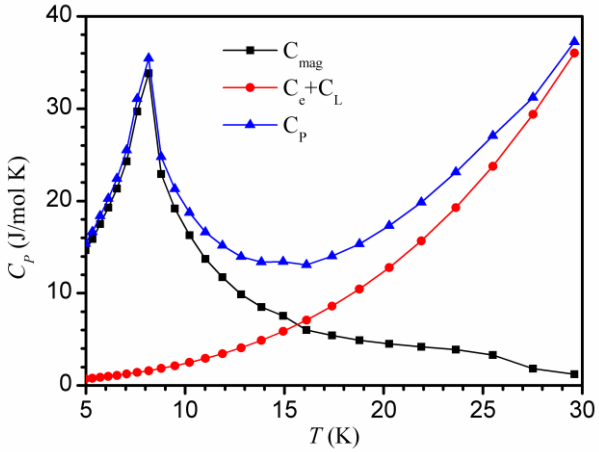

Figure 2.10: Plot of magnetic specific heat (C_{mag}) separated from the electronic (C_e) and lattice (C_{latt}) specific heat, and total specific heat (C_p).

2.4 Conclusions

In summary, the use of an interior graphite-tube containment system made it possible to synthesize single crystals of Li_2MnGeS_4 using IVT. The crystals were used to determine the intrinsic magnetic properties of Li_2MnGeS_4, free from secondary phases. Li_2MnGeS_4 is an antiferromagnetic material, as are the majority of I_2-II-IV-VI_4 DLSs with II being a magnetic ion. Still many other I_2-II-IV-VI_4 compounds are yet to be discovered and/or characterized magnetically. If changes in the composition and/or doping could raise the T_N to more practical temperatures, these materials could be candidates for antiferromagnetic spintronic devices. (*34-37, 69, 70*)

While the crystals reported here are sizable, they are not large enough for laser-induced damage threshold (LIDT) measurements. In previous work by Brant et. al., the LIDT for

polycrystalline Li_2MnGeS_4 could not be determined, as the sample holder (fused-silica tube) incurred optical damage before the material, meaning that the LIDT is >16 GW/cm^2. In this work we have progressed from crystals that are tenths of a millimeter to those that are a couple of millimeters in size. This encourages further studies to grow even larger single crystals of Li_2MnGeS_4 that could be used to measure other intrinsic properties including LIDT and thermal conductivity.

The success of our interior graphite-tube containment system opens up the possibility to grow other lithium-containing chalcogenides via IVT in order to either measure their intrinsic properties or to use as seed crystals for further crystal growth. A few candidate materials for IVT utilizing the graphite-tube containment system include Li_2CdGeS_4 (*71*), $Li_2MnSnSe_4$ (*24*), and $Li_4HgGe_2S_7$ (*72*), which are of interest for IR-NLO applications.

2.5 References

(1) Okorogu, A.O.; Mirov, S.B.; Lee, W.; Crouthamel, D.I.; Jenkins, N.; Dergachev, A.Y.; Vodopyanov; Badikov, V.V., *Opt. Commun.*, **1998**, *155*, 307-312.

(2) Boyd, G.D.; Buechler, E.; Storz, F.G., *Appl. Phys. Lett.*, **1971**, *18,* 301-304.

(3) Schunemann, P.G.; Pollack, T.M., *MRS Bull.*, **1998**, *23,* 23-27.

(4) Catella, G.C.; Burlage, D., *MRS Bull.*, **1998**, *23*, 28-36.

(5) Wang, S.; Gao, Z.; Yin, X.; Liu, G.; Ruan, H.; Zhang, G.; Shi, Q.; Dong, C.; Tao, X., *J. Cryst. Growth*, **2013**, *262*, 308-311.

(6) Ohmer, M.;Pandey, R.; Bairamov, B.H., *MRS Bull.*, **1998**, *23*, 16-22.

(7) Rockett, A.A., *Curr. Opin. Solid State Mater. Sci.*, **2010**, *14*, 143-148.

(8) Stanbery, B.J., *Crit. Rev. Solid State Mater. Sci.,* **2010**, 27, 73-117.

(9) Fella, C.M.; Romanyuk, Y.E.; Tiwari, A.N., *Sol. Energ. Mat. Sol.*, **2013**, *119*, 276-277.

(10) Shin, B.; Gunawan, O.; Zhu, Y.; Bojarczuk, N.A.; Chey, S.J.; Guha, S., *Prog. Photovoltaics*, **2013**, *21*, 72-76.

(11) Wagner, S.; Bridenbaugh, P.M., *J. Cryst. Growth*, **1977**, *39*, 151-159.

(12) Ponce, F.A.; Bour, D.P., *Nature*, **1997**, *386,* 351-359.

(13) Gessmann, T.; Schubert, E.F.; *J. App. Phys.*, **2004**, *95,* 2203-2216.

(14) Dupuis, R.D., *J. Lightwave Technol.*, **2008**, *26*, 1154-1171.

(15) Chang, M.-H.; Das, D.; Varde, P.V.; Pecht, M., *Microelectron. Reliab.*, **2012**, *52*, 762-782.

(16) Yao, J.; Takas, N.J.; Schliefert, M.L.; Paprocki, D.S.; Blanchard, E.R.; Gou, H.; Mar, A.; Exstrom, C.L.; Darveau, S.A.; Poudeu, P.F.F.; Aitken, J.A., *Phys. Rev. B*, **2011**, *84*, 075203-

(17) Ortiz, B.R.; Peng, W.; Gomes, L.; Gorai, P.; Zhu, T.; Smiadak, D.M.; Snyder, G.S.; Stevanović, V.; Ertekin, E.; Zevalkink, A.; Toberer, E.S., *Chem. Mater.*, **2018**, *30*, 3395-3409.

(18) Cho, J.Y.; Shi, X.; Salvador, J.R.; Yang, J.; Wang, H., *J. Appl. Phys.,* **2010***, 108*, 073713.

(19) Qui, P.; Qin, Y.; Zhang, Q.; Li, R.; Yang, J.; Song, Q.; Tang, Y.; Bai, S.; Shi, X.; Chen, L., *Adv. Sci.*, **2018**, *5*, 1700727.

(20) Nénert, G.; Palstra, T.T.M., *J. Phys.: Condens. Matter, 2009, 21*, 176002.

(21) Erwin, S.C., Žutić, I., *Nat. Mater.*, **2004**, *3*, 410-414.

(22) Zhao, Y.-J.;Zunger, A., *Phys. Rev. B.*, **2004**, *69*, 104422-104430.

(23) Brant, J.A.; Devlin, K.P.; Bischoff, C.; Watson, D.; Martin, S.W.; Gross, M.D.; Aitken, J.A., *Solid State Ionics*, **2015**, *278*, 268-274.

(24) Li, X.; Li, C.; Zhou, M.; Wu, Y.; Yao, J., *Chem. Asian J.*, **2017**, *12*, 3172-3177.

(25) Fries, T.; Shapira,Y.; Palacio, F.; Morón, C.; McIntyre, G.J.; Kershow, R.; Wold, A.; McNiff, E.J., *Phys. Rev. B*, **1997**, *56*, 5424.

(26) Caneschi, A.; Cipriani, C.; Denedetto, F.D.; Sesoli, R., *Phys. Chem. Miner.*, **2004**, *31*, 190-193.

(27) Quintero, E.; Quintero, M.; Moreno, E.; Lara, L.; Morocoima, M.; Pineda, F.; Grima, P.; Tovar, R.; Bocaranda, P.; Henao, J.A.;. Macías, *J. Phys. Chem. Solids*, **2010**, *71*, 993-998.

(28) Guen, L.; Glaunsinger, W.S., *J. Solid State Chem.*, **1980**, *35*, 10-21.

(29) Quintero, M.; Tovar, R.; Barreto, A.; Quintero, E.; Rivero, A.; Gonzalez, J.; Porras, G.S.; Ruiz, J.; Bocaranda, P.; Broto, J.M.; Rakoto, H.; Barbaste, R., *Phys. Sat. Sol.*, **1998**, *209*, 135-143.

(30) Friedrich, D.; Greil, S.; Block, T.; Heletta, L.; Pöttgen, R.; Pfitzner, A., *Z .Anorg. Allg. Chem.,* **2018**

(31) Brant, J.A.; Cruz, C.; Yao, J.; Douvalis, A.P.; Bakas, T.; Sorescu, M.; Aitken, J.A., *Inorg. Chem.,* **2014**, 53, 12265-12274.

(32) Chen, X.L.; Lamarche, A.-M.; Lamarche, G.; Woodlley, J.C., *J. Magn. Magn. Mater.*, **1993**, *118* 119-128.

(33) Guen, L.; Glaunsinger, W.S.; Wold, A., *Mater. Res. Bull.*, **1979**, *14*, 463-467.

(34) Jungwirth, T.; Sinova, J.; Manchon, A.; Marti, X.; Wunderlich, J.; Felser, C., *Nat. Phys.*, **2018**, *14*, 200-203.

(35) Němec, P.; Fiebig, M.; Kampfrath, T.; Kimel, A.V., *Nat. Phys.*, **2018**, *14*, 229-241.

(36) M.B. Jungfleisch, W. Zhang, A. Hoffmann, Perspectives of antiferromagnetic spintronics, Phys. Lett. A 382 (2018) 865-871. https://doi.org/10.1016/j.physleta.2018.01.008

(37) Baltz, V.; Manchon, A.; Tsoi, M.; Moriyama, T.; Ono, T.; Tserkovnyak, Y., *Rev. Mod. Phys.*, **2018**, *90*, 1-179.

(38) Ando, K., *Mater Sci.*, **2006**, *312*, 1883-1885.

(39) Kundaliya, D.C.; Ogale, S.B.; Lofland, S.E.; Dhar, S.; Metting, C.J.; Shinde, S.R.; Ma, Z.; Varughese, B.; Ramanujachary, K.V.; Salamanca-Riba, L.; Venkatesan, T., *Nat. Mater.*, **2004**, *3*, 709-714.

(40) Lawes, G.; Risbud, A.S.; Ramirez, A.P.; Seshadri, R., *Phys. Rev.*, **2005**, *B 71*, 045201.

(41) Skomia, P.; Goraus, J.; Koperski, J.; Wojtyniak, M.; Slebarski, A., *Intermetallics*, **2017**, *85*, 144-148.

(42) Bundy, F.P.; Kasper, J.S., *J. Chem. Phys.*, **1967**, *46*, 3437-3446.

(43) Brant, J.A.; Clark, D.J.: Kim, Y.S.; Jang, J.I.: Weiland, A.; Aitken, J.A., *Inorg. Chem.,* **2015***, 54*, 2809-2819.

(44) Yamaguchi, H.; Akatsuka, K.; Setoguchi, M.; Takaki, Y., *Acta Cryst.*, **1979**, *B35*, 2680-2682.

(45) Duc, T.; Vincent, H.; Bertaut, E.F.; Qui, V.V., *Solid State Commun.*, **1969**, *7*, 641-645.

(46) Schäfer, W.; Nitsche, R., *Mat. Res. Bull.*, **1974**, *9*, 645-654.

(47) Nitsche, R.; Sargent, D.F.; Wild, P., *J. Cryst. Growth*, **1967**, 1, 52-53.

(48) Wang, S.; Gao, Z.; Zhang, X.; Zhang, X.; Li, C.; Dong, C.; Lu, C.; Zhao, M.; Tao, X., *Cryst. Growth Des.*, **2014**, *14*, 5957-5961.

(49) Kamijoh, T.; Kuriyama, K., *J. Cryst. Growth*, **1979**, *46* 801-803.

(50) Magesh, M.; Vijayakumar, P.; Arunkumar, A.; Babu, G.A.; Ramasamy, P., *Mater. Chem. Phys.,* **2015**, 149-150, 224-229.

(51) Jia, N.; Wang, S.; Gao, Z.; Wu, Q.; Li, C.; Zhang, X.; Yu, T.T.: Lu, Q.; Tao, X., *Cryst. Growth Des.*, **2017**, *17*, 5875-5880.

(52) Guo, L.; Xu, Y.; Zheng, H.; Wue, W.; Dong, J.; Zhang, B.; He, Y.; Zha, G.; Chung, D.Y.; Jie, W.; Kanatzidis, M., *Cryst. Growth Des.*, **2018**, *18*, 2864-2870.

(53) Vijayakumar, P.; Magesh, M.; Arunkumar, A.; Babu, G.A.; Ramasamy, P.; Abhaya, S., *J. Cryst. Growth*, **2014**, *388*, 17-21.

(54) Wang, S.; Zhang, X.; Zhang, X.; Li, C.; Gao, Z.; Lu, Q.; Tao, X., *J. Cryst. Growth,* **2014**, *410*, 150-155.

(55) Magesh, M.; Arunkumar, A.; Vijayakumar, P.; Babu, G.A.; Ramasamy, P., *Opt. Laser Technol.*, **2014**, *56*, 177-181.

(56) Tupitsyn, E; Bhattacharya, P.; Rowe, E.; Matei, L.; Cui, Y.; Buliga, V.; Groza, M.; Wiggins, B.; Burger, A.; Stowe, A., *J. Cryst. Growth*, **2014**, *393*, 23-27.

(57) Schäfer, H., Chemical transport reactions, Academic Press, NY, **1964**.

(58) Faktor, M.M., Garrett, I., Growth of crystals from vapor, Chapman and Hall Ltd., London, UK **1974**.

(59) Zuo, R.; Wang, E., *J. Cryst. Growth*, **2002**, *236,* 687-694.

(60) Zuo, R.; Wang, W., *J. Cryst. Growth*, **2002**, *236*, 695-710.

(61) Spaldin, N.A., Magnetic materials fundamentals and applications, 2nd ed., Cambridge, UK, **2011**.

(62) West, A.R., Solid state chemistry and its applications, John Wiley & Sons Ltd, London, UK, **1984**.

(63) Lide, D.R., CRC handbook of chemistry and physics, CRC Press Inc., Boca Raton, FL, **1993**.

(64) Bernert, T.; Pfitzner, A., *Z. Kristallogr.*, **2005**, *220*, 968-972.

(65) Parthé, E.; Yvon, K.; Deitch, R.H., *Acta. Crystallog*., **1969**, *B25*, 1164-117.

(66) Quintero, M.; Quintero, E.; Moreno, E.; Grima-Gallardo, P.; Marquina, J.; Alvarez, S.; Rincón, C.; Rivero, D.; Morocoima, M.; Henao, J.A.; Macias, M.A.; Briceño, J.M.; Rodriguez, N., *Rev. LatinAm. Metal. Mat.*, **2017**, *37*, 27-34.

(67) Bonassi, P.; Bindi, L.; Bernardini, G.P; Menchetti, S., *Can. Mineral.*, **2003**, 41, 639-647.

(68) Brunetta, C.D.; Brant, J.A.; Rosmus, K.A.; Henline, K.M.; Karey, E.; MacNeil, J.H.; Aitken, J.A., *J. Alloys Compd.*, **2013**, *574,* 495-503.

(69) Gomonay, O.; Baltz, V.; Brataas, A.; Tserkovnyak, Y., *Nat. Phys.*, **2018**, *14*, 213-216.

(70) Šmejkal, L.; Mokrousov, Y.: Yan, B.; MacDonald, A.H., *Nat. Phys.*, **2018**, *14*, 242-251.

(71) Brant, J.A.; Clark, D.J.; Kim, Y.S.; Jang, J.I.; Zhang, J.-H.; Aitken, J.A., *Chem. Mater.*, **2014**, *26*, 3045-3048.

(72) Wu, K.; Yang, Z.; Pan, S., *Chem. Commun.*, **2017**, *53*, 3010.

Chapter 3: Synthesis, Structure and Properties of $Cu_4MnGe_2S_7$ and Cu_2MnGeS_4: Biaxial, Quaternary Diamond-like Semiconductors Displaying Second Harmonic Generation in the Infrared

3.1 Introduction

Diamond-like semiconductors (DLSs) have gained interest for their use in infrared (IR) nonlinear optical (NLO) applications, including those of interest for military (*1-7*) and medical (*8-12*) use. The military applications include IR countermeasure systems (*1-5*) and standoff detection of chemical and biological weapons (*6,7*), while medical uses encompass minimally invasive laser surgery (*8,9*) and disease detection. (*10-12*) All current commercially-available IR-NLO materials are ternary DLSs, such as $AgGaS_2$ (AGS), $AgGaSe_2$ (AGSe) (*13*), and $ZnGeP_2$ (ZGP). (*14*)

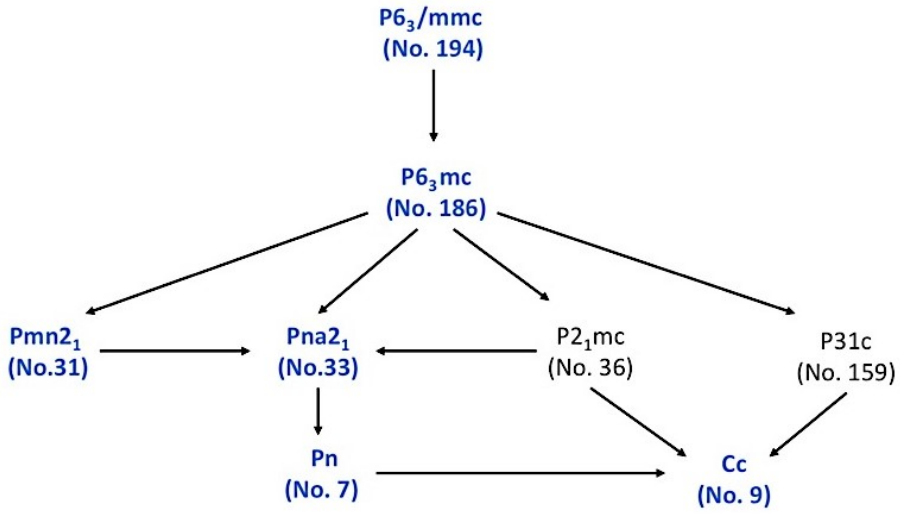

Figure 3.1: Derivation of space groups for DLSs starting from the space group for hexagonal diamond. Blue indicates space groups have been identified for DLSs; no DLSs have been found to crystalize in the space groups in grey.

However, these materials have drawbacks, which inhibit practical applications; thus there is a need for new candidate materials. (*15-19*)

To this end, much NLO research has been devoted to identifying attractive materials. Recently, many new metal chalcogenides have been discovered with high SHG, including

$Ba_3CsGa_5Se_{10}Cl_2$ (*20*), $BaGa_4Se_7$ (*21*), $Na_2Hg_3Sn_2S_8$ (*22*), γ-$NaAsSe_2$ (*23*), Li_2HgSnS_4 (*24*), $Li_4HgGe_2S_7$, (*25*) Li_2MnGeS_4, (*26*) Li_2CdGeS_4, (*27*) Cu_2ZnSiS_4 (*28*) and others. (*29-41*) Diamond-like materials are a promising area to search for new candidate IR-NLO materials, as their synthesis is predictable, they are intrinsically noncentrosymmetric (NCS), and the properties can be tuned.

The predictability and NCS structure result from the adherence to four guidelines used to target the synthesis of I_2-II-IV-VI_4 DLSs, of which the first three guidelines also hold true for I_4-II-IV_2-VI_7 DLSs. The first guideline is that all ions must adopt tetrahedral coordination. (*42,43*) The average number of valence must be equal to 4 and the average number of valence electrons per anion must equal 8. (*42,43*) The fourth guideline is Pauling's second rule, which states that the charge of the anion must be compensated by the cations within the first coordination sphere. (*44*) This final guideline is followed by all I_2-II-IV-VI_4 DLSs, while some of the anions in I_4-II-IV_2-VI_7 DLSs do not obey Pauling's second rule. Adherence to these guidelines has resulted in hundreds of DLSs derived from either cubic or hexagonal diamond (*42-46*), Figure 3.1 displays this derivation starting with hexagonal diamond.(*42,45*)

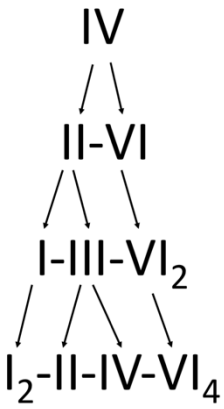

Figure 3.2: Cross substitution diagram for DLSs.(*42,45)*

Multiple avenues for property tuning is another reason that DLSs are a good area to search for new candidate IR-NLO materials. There are multiple ways in which a DLS can be tuned. Doping can be used to alter the properties (*47*), along with the choice of elements. The properties of DLSs have also been tuned by progression from binary to ternary and quaternary materials. (*42-45*) Each time an additional element has been added

to the general formula, the degree of tunability has increased, Figure 3.2. Changing the stoichiometry is another option for tuning properties.

Table 3.1 Published I_4-II-IV_2-VI_7 DLSs.

Compound	Space Group	Reference
$Li_4MnGe_2S_7$	*Cc*	*48*
$Li_4MnSn_2S_7$	*Cc*	*48*
$Li_4HgGe_2S_7$	*Cc*	*49*
$Ag_4HgGe_2S_7$	*Cc*	*50*
$Ag_4CdGe_2S_7$	*Cc*	*50*
$Cu_4NiSi_2S_7$	*C*2	*51*
$Cu_4NiGe_2S_7$	*C*2	*51*

This work investigated the differences between two quaternary DLSs, $Cu_4MnGe_2S_7$ and Cu_2MnGeS_4. The effect of changing stoichiometry in quaternary DLSs has not yet been investigated, as there are relatively few published I_4-II-IV_2-VI_7 materials, and the corresponding properties are not always available for the analogous I_2-II-IV-VI_4. Table 3.1 is a compilation of the I_4-II-IV_2-VI_7 quaternary DLSs that have been published to date.

This paper presents the crystal structure of the new DLS $Cu_4MnGe_2S_7$, which is compared to Cu_2MnGeS_4. (*52-54*) In prior work, Cu_2MnGeS_4 has been investigated for its magnetic properties and is known to crystalize in the P*mn*2_1 space group, have a bandgap of 2.035 eV, and be an antiferromagnetic material; however, its NLO properties have not been reported. (52-54) Here we report the SHG, phase matchability, optical bandgap, electronic structure, transparency windows in the infrared, and the thermal stability of $Cu_4MnGe_2S_7$ and Cu_2MnGeS_4. The laser induced damage threshold (LIDT) is also reported for Cu_2MnGeS_4.

3.2. Experimental

3.2.1 Synthesis

3.2.1.1 Cu_2MnGeS_4 Synthesis

To prepare phase-pure $Cu_4MnGe_2S_7$ via high-temperature, solid-state synthesis Cu (4 mmol, powder, 99.999%, Strem), Mn pieces (2 mmol, 99.98%, washed with 10% nitric acid in methanol before being ground using a diamonite mortar and pestle, Alfa Aesar), Ge pieces (2 mmol, 99.999%, ground using a diamonite mortar and pestle, Strem) and S (8 mmol, sublimed powder, 99.5%, Fisher Scientific) were weighed out and ground with an agate mortar and pestle until visually homogeneous. The combined starting materials were then pressed into an 8 mm pellet, using a Carver mechanical press at 2 metric tons of pressure. The pellet was placed in a 12 mm o.d. carbon-coated, fused-silica tube and sealed under vacuum of 10^{-4} mbar. The sealed reaction vessel was heated in a programmable furnace to 850 °C in 12 hours, held at 850 °C for 168 hours and then cooled to 650 °C at a rate of 2 °C/hour, after which it was cooled to room temperature ambiently.

3.2.1.2 $Cu_4MnGe_2S_7$ Synthesis of Single Crystals

Single crystals of $Cu_4MnGe_2S_7$ were prepared through high-temperature, solid-state synthesis. The reactions were prepared by weighing out Cu (8 mmol, powder, 99.999%, Strem), Mn pieces (2 mmol, 99.98%, washed with 10% nitric acid in methanol before being ground using a diamonite mortar and pestle, Alfa Aesar), Ge pieces (4 mmol, 99.999%, ground using a diamonite mortar and pestle, Strem) and S (14 mmol, sublimed powder, 99.5%, Fisher Scientific) and grinding them with an agate mortar and pestle until visually homogeneous. The ground starting materials were then placed in a 9 mm o.d. fused-silica tube, which was housed in a 12 mm o.d. fused-silica tube

and sealed under vacuum of 10^{-4} mbar. The sealed reaction vessel was heated in a programmable furnace to 850 °C in 12 hours, held at 850 °C for 168 hours and then cooled to 650 °C at a rate of 2 °C/hour, after which it was cooled to room temperature ambiently. The reaction products were identified as $Cu_4MnGe_2S_7$, Cu_2MnGeS_4 (*52*) and Cu_2GeS_3 (*55*) via X-ray powder diffraction. Dark red triangular prisms were identified as $Cu_4MnGe_2S_7$ and selected under a light microscope.

3.2.1.3 $Cu_4MnGe_2S_7$ Synthesis of Phase-Pure Material

To prepare phase-pure $Cu_4MnGe_2S_7$ via high-temperature, solid-state synthesis Cu (4 mmol, powder, 99.999%, Strem), Mn pieces (2 mmol, 99.98%, washed with 10% nitric acid in methanol before being ground using a diamonite mortar and pestle, Alfa Aesar), Ge pieces (2 mmol, 99.999%, ground using a diamonite mortar and pestle, Strem) and S (8 mmol, sublimed powder, 99.5%, Fisher Scientific) were weighed out and combined in a vial and shaken until visually homogeneous. The combined starting materials were then pressed into an 8 mm pellet, using a Carver mechanical press at 2 metric tons of pressure. The pellet was placed in a 12 mm o.d. carbon-coated, fused-silica tube and sealed under vacuum of 10^{-4} mbar. The sealed reaction vessel was heated in a programmable furnace to 1075 °C in 12 hours, dwelled at 1075 °C for 216 hours, and cooled to 875 °C at a rate of 2°C/hour, after which the reaction was cooled to room temperature ambiently.

3.2.2 Single Crystal X-ray Diffraction

The single-crystal X-ray diffraction data for $Cu_4MnGe_2S_7$ were collected using a Bruker SMART Apex 2 CCD single-crystal diffractometer. The instrument was equipped with graphite-monochromatized Mo-K_α radiation and the tube power was 50 kV and 30 mA. A dark, red

triangular prism of $Cu_4MnGe_2S_7$ with dimensions of 0.11 x 0.06 x0.06 mm was selected for data collection. Table 3.2 contains the pertinent crystallographic data and experimental details. These data were collected using 20 second frames over the range of 2.4-27.5° theta. From the collected data, a total of 2390 reflections were obtained with 2059 being unique ($R_{(int)}$=0.0269). The data integration was accomplished using the SAINT program, with the analytical absorption correction performed using SADABS. (*56*) The systematic absences were identified using XPREP and two possible space groups were suggested, C*c* and C2/*c*; the NCS space group Cc was selected as all I_4-II-IV_2-VI_7 DLSs possess NCS structures with aligned tetrahedral units. XPREP was used to prepare files for SHELX, the software package that was used for structure solution and refinement. (*57*) Fourteen crystallographically unique atoms were located in the structure, all of which reside on general positions. Both the Flack

Table 3.2: Crystallographic data and experimental details for $Cu_4MnGe_2S_7$

Chemical Formula	$Cu_4MnGe_2S_7$
Formula Weight (g mole^{-1})	678.70
Temperature (°C)	25
Wavelength (Å)	0.71073
Space Group	C*c* (No. 9)
a (Å)	16.7443(3)
b (Å)	6.47893(9)
c (Å)	9.8060(1)
β(°)	93.188(1)
Volume (Å^3)	1062.16(3)
Z	4
D_{calc} (g cm^{-3})	4.244
μ (cm^{-1})	15.901
Flack parameter	-0.003(15)
R1 [I>2σ(I)], R1 (all data)	0.0270, 0.0335
wR2[I>2σ(I)], wR2(all data)	0.0595, 0.0640

$$wR2 = \left\{\frac{\Sigma[w(F_0^2 - F_c^2)^2]}{\Sigma[w(F_o^2)^2]}\right\}^{\frac{1}{2}}, \quad R1 = \Sigma\big||F_o| - |F_c|\big|/\Sigma|F_o|$$

parameter and extinction coefficient were refined. The CrystalMaker software package was used to generate all of the crystal structure figures in this publication. (*58*)

3.2.3 X-ray Powder Diffraction (XRPD)

The X-ray powder diffraction data were collected using a PANalytical X'Pert Pro MPD X-ray diffractometer equipped with the X'cellerator detector. This instrument operates with Cu $\mathbf{K_\alpha}$ radiation with a wavelength of 1.541871 Å. The data were collected over a range of 5° to 145° 2θ using a tube power of 45 kV and 40 mA. The data collection was completed using a step size of 0.0085556 and a scan rate of 0.010644 °/s. The instrument optics included 0.02 rad. soller slits, and a fixed anti-scatter slit of ½°. The incident beam path also contained a divergent slit fixed at ¼° and the diffracted beam path also included a nickel filter. The samples were prepared for analysis by grinding them in an agate mortar and pestle for 5 minutes, after which they were top-filled onto a zero-background holder. To identify the crystalline phases in the samples, the search-match capabilities of the X'Pert HighScore Plus (*59*) software coupled with the International Centre for Diffraction Data (ICDD) powder diffraction file (PDF) database were used. (*60*)

3.2.4 Second-Harmonic Generation (SHG)

Powdered samples of $Cu_4MnGe_2S_7$ and Cu_2MnGeS_4 were sieved into discrete particle size ranges of 0 – 20 μm, 20 – 45 μm, 45 – 63 μm, 63 –75 μm, 75 – 90 μm, 90 – 106 μm, 106 – 125 μm, and 125 – 150 μm to examine the phase-matching behavior of the samples. The powders in each size range were enclosed in quartz capillary tubes that were subsequently flame sealed under vacuum to prevent exposure to air and moisture during measurements. Each tube was loaded into a homemade sample holder that was mounted on a Z-scan translation stage. SHG measurements of the samples were compared with those of a reference nonlinear optical (NLO) material, AGSe,

which was provided by Gooch and Housego. It should be noted that this optical-quality sample typically yields a SHG response that is two times stronger than that recorded for homemade samples. (*27*)

The phase matching (PM) behavior of Cu_2MnGeS_4 was assessed using an incident wavelength of 3100 nm, where the AGSe reference is PM. $Cu_4MnGe_2S_7$ showed a very low nonlinear response and the signal-to-noise ratio was not acceptable at long incident wavelengths; therefore, the SHG response of $Cu_4MnGe_2S_7$ was recorded with an incident wavelength of 1600 nm, rather than 3100 nm. In this case, the incident wavelength of 1600 nm produced the largest response. For both samples, the SHG signal was collected using a reflection geometry and a fiber-optic bundle, which was coupled to a selective-grating (1800, 600, and 300 grooves/mm) spectrometer equipped with a CCD camera. We confirmed that any surface-induced effects, as well as SHG signals from other optical components were negligible. Any thermal load on the samples by the laser pulses tuned below the bandgap was negligible due to its slow repetition rate of 50 Hz. All measurements were carried out at room temperature and the pulse width, τ, was 30 ps. The details about the excitation source are available elsewhere. (*27*)

3.2.5 Laser-Induced Damage Threshold (LIDT)

The LIDT for Cu_2MnGeS_4 was assessed using a wavelength of 1064 nm, which is the primary wavelength for picosecond difference frequency generation (DFG) for obtaining mid-IR coherent light. It was not possible to estimate the LIDT for $Cu_4MnGe_2S_7$ because the sample showed a very low nonlinear response. The Cu_2MnGeS_4 sample of the largest particle size was exposed to an input intensity that was increased from 0.2 GW/cm^2 to 2.5 GW/cm^2.

3.2.6 Optical Diffuse Reflectance UV-vis-NIR Spectroscopy

The optical diffuse reflectance spectra were collected for $Cu_4MnGe_2S_7$ and Cu_2MnGeS_4 using a Varian Cary 5000 spectrometer operating with a Harrick Praying Mantis diffuse reflectance accessory. Data were collected over the ultraviolet, visible and near infrared spectral regions (UV-vis-NIR), from 2500 to 200 nm. Firstly, data were collected for barium sulfate (Fisher, 99.92%) that was used as the 100% reflectance standard. Subsequently, the ground samples were placed on top of the barium sulfate standard and scanned at a rate of 600 nm/min. The raw data were collected as percent reflectance (%R) and converted to relative absorption (α_{KM}) since the scattering coefficient, s, is unknown using the Kubelka-Munk transformation. (*61*)

3.2.7 Electronic Structure Calculations

Density functional theory (DFT) simulations were performed within the generalized gradient approximation (GGA) as implemented by Perdew-Burke-Ernzerhof (PBE) (*62*) using the Vienna *Ab inito* Simulation Package (VASP). (*63,64*) A 500 eV planewave cutoff and projector augmented-wave (PAW) pseudopotentials (*65*) were used for all elements in the calculations for $Cu_4MnGe_2S_7$ and Cu_2MnGeS_4 with the following valence electron configurations: Cu ($3d^{10}4s^1$), Mn ($3d^6 4s^1$), Ge ($3d^{10}4s^2 4p^2$), and S ($3s^2 3p^4$). The **Γ**-centered k-point meshes and 2x4x3 and 4x4x4 grids were used for $Cu_4MnGe_2S_7$ and Cu_2MnGeS_4, respectively. Gaussian smearing (0.05 eV width) for sampling and integrations within the Brillouin zone were used. For the density of states calculations, the tetrahedron method with Blöchl corrections was implemented.

Full lattice relaxations were carried out until the residual forces on the individual atoms were less than 5.0 meV $Å^{-1}$. Since it is known that Cu_2MnGeS_4 exhibits antiferromagnetic (AFM) spin order, spin-polarized calculations with opposite spins on adjacent Mn atoms, i.e. in a G-type

AFM configuration, were initially used. On-site Coulomb interactions are not included due to the half-filled d^5 and fully-filled d^{10} electronic configurations of Mn and Cu ions, respectively. Spin-orbit interactions were omitted in the simulations.

3.2.8 FT-IR Spectroscopy

A Thermo Nicolet 380 FT-IR spectrometer was used to collect the FT-IR spectra of Cu_2MnGeS_7 and $Cu_4MnGe_2S_7$. The OMNIC software was employed to both collect and analyze the data, which were collected from 64 scans from 400-4000 cm^{-1}. For collection, the samples were formed into KBr pellets. Prior to the creation of the pellets, FT-IR grade KBr (Strem) was dried for 3 hours at 110 °C and cooled in a desiccator. (*66*) The pellet consisted of approximately 250 mg of KBr and 2.5 mg of sample, which were ground in an agate mortar and pestle until visually homogeneous. (*66*) The pellet was pressed in a 12 mm die under 8 metric tons of pressure for 15 minutes. (*66)*

3.2.9 Differential Thermal Analysis (DTA)

The thermal behaviours of $Cu_4MnGe_2S_7$ and Cu_2MnGeS_4 were studied using a Shimatzu DTA-50, coupled with the TA60-WS data collection program. The instrumentation was calibrated using a three-point calibration with indium, zinc and gold metals. To analyse the samples, approximately 25 mg of $Cu_4MnGe_2S_7$ and Cu_2MnGeS_4 were vacuum sealed into carbon-coated, fused-silica ampoules. The Al_2O_3 reference ampoules of comparable masses were used. Both the sample and reference were heated at a rate of 10°C min^{-1} from 25°C-1000°C, and held at the maximum temperature for one minute, after which both were cooled at the same rate while under a constant flow of nitrogen. To assess the reproducibility of the thermal events, two cycles of this process were performed.

3.3. Results and Discussion

3.3.1 Crystal Structure

$Cu_4MnGe_2S_7$ crystalizes in the noncentrosymmetric monoclinic space group C*c* with the $Cu_5Si_2S_7$ structure type. (*67*, *68*) The structure of $Cu_4MnGe_2S_7$ contains fourteen crystallographically unique atoms, including four copper, one manganese, two germanium and seven sulfur, all located on general positions. In comparison, Cu_2MnGeS_4 crystallizes in the orthorhombic space group P*mn*2_1 (*52*) with the wurtz- stannite (*69*) structure, and has six crystallographically unique atoms, including one copper, one manganese, one germanium and three suflur. The unit cells of Cu_2MnGeS_4 and $Cu_4MnGe_2S_7$ both consisting of corner-sharing MS_4 tetrahedra can be seen in Figure 3.3.

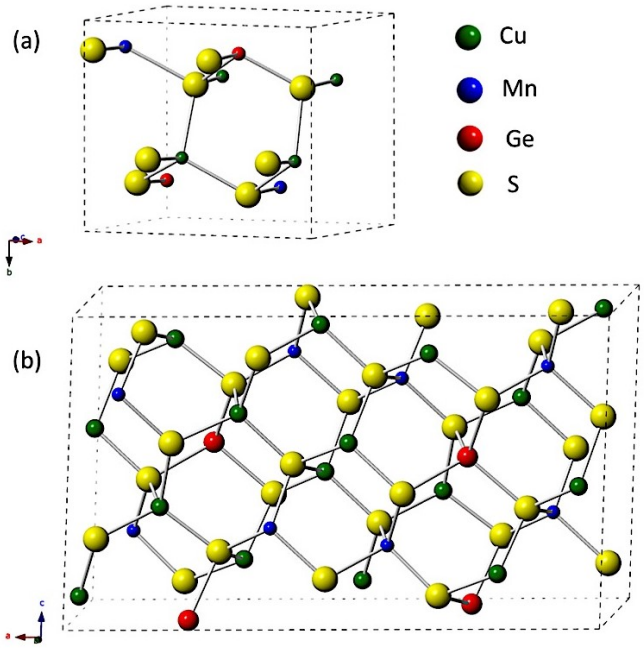

Figure 3.3: Unit cells of (a) Cu_2MnGeS_4 and (b) $Cu_4MnGe_2S_7$ with the copper, manganese, germanium and sulfur atoms shown in green, blue, red and yellow, respectively.

In Cu_2MnGeS_4 all sulfur anions follow Pauling's second rule, being bound to two copper, one manganese and one germanium cation. In $Cu_4MnGe_2S_7$ four of the sulfur anions, S(3), S(4), S(6) and S(7), also follow Pauling's second rule. Atoms S(1), S(2) and S(5) have different cation neighbours and do not following Pauling's second rule, which states that the charge of the anion is compensated by the charge of the cations within one coordination sphere. (*44*) Atoms S(2) and S(5) are coordinated to three copper and one germanium cation, producing a local cationic charge

Table 3.3: Extended connectivity table for $Cu_4MnGe_2S_7$ showing calculated horizontal and vertical bond strength sums.

	4S(1)	4S(2)	4S(3)	4S(4)	4S(5)	4S(6)	4S(7)	Horizontal Bond Strength Sum
4Cu(1)				4 x ¼	4 x ¼	4 x ¼	4 x ¼	∑ = 4
4Cu(2)	4 x ¼	4 x ¼	4 x ¼		4 x ¼			∑ = 4
4Cu(3)		4 x ¼	4 x ¼	4 x ¼		4 x ¼		∑ = 4
4Cu(4)	4 x ¼	4 x ¼			4 x ¼		4 x ¼	∑ = 4
4Mn(1)			4 x ½	4 x ½		4 x ½	4 x ½	∑ = 8
4Ge(1)	4 x 1	4 x 1	4 x 1	4 x 1				∑ = 16
4Ge(2)	4 x 1				4 x 1	4 x 1	4 x 1	∑ = 16
Vertical Bond Strength Sum	∑ = 10 (10 > 8)	∑ = 7 (7 < 8)	∑ = 8	∑ = 8	∑ = 7 (7 < 8)	∑ = 8	∑ = 8	

of +1.75 and a net charge of -0.25 per tetrahedron, which is an under compensation of 12.5%. Conversely, the charge of the S(1) anion in $Cu_4MnGe_2S_7$ is over charge compensated by 25%, +0.50 per tetrahedron resulting from S(1) being bound to two copper and two germanium cations. An extended connectivity table displaying the calculated horizontal and vertical bond strength sums for $Cu_4MnGe_2S_7$ can be found in Table 3.3.

The local charge imbalances present in the $Cu_4MnGe_2S_7$, in some cases, lead to distortions in the bond lengths and angles, as displayed in Table 3.4. It is interesting to note that Mn is only connected to sulfur anions where Pauling's second rule is adhered to. The M-S bond distances, in which the sulfur is undercompensated for in terms of charge, are predicted to shorten, while the M-S bond distances where the sulfur is overcompensated are forecasted to be longer. We examined the M-S bond distances in the structure to look for these effects.

In the case of copper, the Cu-S(2) and Cu-S(5) bond distances are predicted to be shorter than the Cu-S distances for sulfur atoms where Pauling's second rule is followed; yet, this is not always

Table 3.4: Average bond distances, average bond angles and angle ranges for Cu_2MnGeS_4 and $Cu_4MnGe_2S_7$.

	Cu_2MnGeS_4 (*52*)	$Cu_4MnGe_2S_7$
Space Group	P*mn*2_1	C*c*
Cu-S bond average	2.3265(3) Å	2.3225(5) Å
Mn-S bond average	2.4487(4) Å	2.436(1) Å
Ge-S bond average	2.2274(4) Å	2.2246(7) Å
S-Cu-S angle average	109(3)°	109.37(2)°
S-Cu-S angle range	104.76°-112.26°	101.12(8)°-115.17(8)°
S-Mn-S angle average	109.5(6)°	109.46(4)°
S-Mn-S angle range	108.77°-109.92°	106.2(1)°-112.3(1)°
S-Ge-S angle average	109(1)°	109.42(2)°
S-Ge-S angle range	107.44°-110.56°	104.21(8)°-115.21(8)°

the case. The shortest among all Cu-S distances is clearly the Cu(2)-S(5) distance at 2.285(2) Å, agreeing with the prediction. On the other hand, the next shortest Cu-S distances of 2.293(2) Å for Cu(4)-S(5) and 2.296(2) Å for Cu(3)-S(2), are identical to the Cu(2)-S(3) bond distance, where S(3) obeys Pauling's second rule. The reality that some of the Cu-S distances for the undercompensated sulfurs are not the shortest, or significantly shorter, than average can be rationalized by the fact that the undercompensation of S(2) and S(5) is only 12.5%. In contrast, the shortening of bonds for the undercompensated sulfur anions is more consistent and substantial in the case of Ge-S distances, where Ge(1)-S(2) and Ge(2)-S(5) are the shortest Ge-S bond distances in the structure at 2.200(2) Å and 2.189(2) Å, respectively; the next longest Ge-S bond distance is found for Ge(1)-S(3) at 2.216(2) Å.

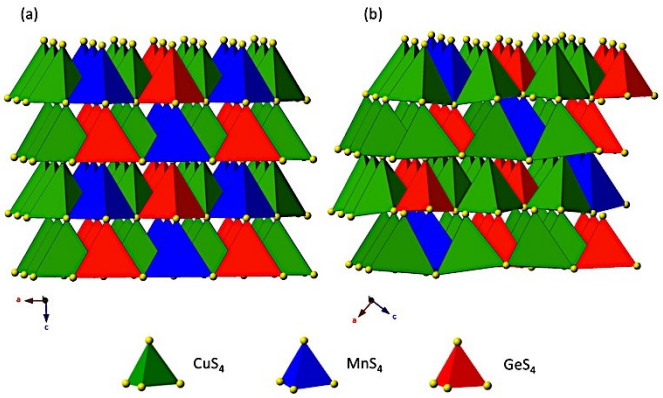

Figure 3.4: Cation ordering representation of (a) Cu_2MnGeS_4 and (b) $Cu_4MnGe_2S_7$, with CuS_4, MnS_4, and GeS_4 represented in green, blue and red, respectively.

More marked distortions are observed for the M-S(1) distances, where S(1) is 25% overcompensated by the nearest neighbor cations. As expected, the Cu(2)-S(1) and Cu(4)-S(1) bond distances are the longest in the structure at 2.409(2) Å and 2.390(2) Å. The third longest distance is found for Cu(3)-S(3) at 2.343(2) Å. The same effect is noticeable for the Ge-S(1) distances that are 2.295(2) Å and 2.312(2) Å for Ge(1) and Ge(2) respectively, while the third longest distance found for Ge(1)-S(4) is 2.229(2) Å. Although $Cu_4MnGe_2S_7$ has three sulfur anion environments that violate Pauling's second rule, the resulting distortions are surprisingly so subtle that the compound still looks very much like a diamond-like semiconductor and should be considered as such.

Not only do the crystal structures of $Cu_4MnGe_2S_7$ and Cu_2MnGeS_4 differ in sulfur anion environments, but also in their cation ordering patterns. Like most DLSs of the formula I_2-II-IV-VI_4, Cu_2MnGeS_4 has an easily identifiable repeating pattern of MS_4 tetrahedra. As displayed in Figure 3.4a, when viewed along the *b*-axis, rows of the same type of MS_4 tetrahedra are observed.

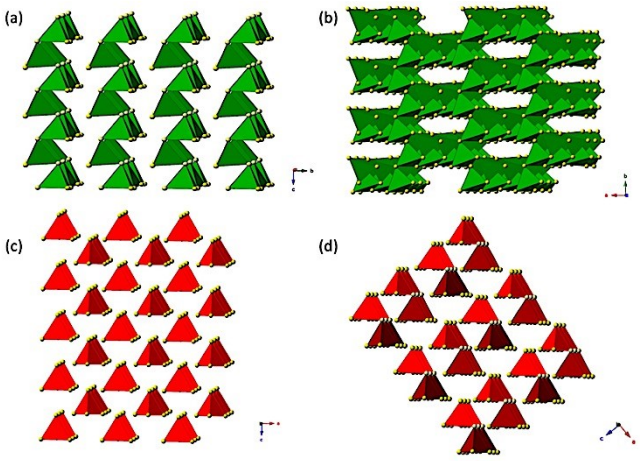

Figure 3.5: Cu_2MnGeS_4 tetrahedral connectivity of only the (a) CuS_4 tetrahedra and (c) GeS_4 tetrahedra. $Cu_4MnGe_2S_7$ tetrahedral connectivity of only the (b) CuS_4 and (d) GeS_4 tetrahedra.

Presented in Figure 3.4a across the *a*-axis, from left to right the repeating pattern of CuS_4, MnS_4, CuS_4, GeS_4 tetrahedra are seen, and across the *c*-axis, from top to bottom of the figure, columns of CuS_4 tetrahedra are observed, interrupted by columns of alternating MnS_4 and GeS_4 tetrahedra. To view the cation ordering pattern of Cu_2MnGeS_4 in its entirety, a 4 x 2 view of the metal-sulfur tetrahedra is needed. The cation ordering pattern of $Cu_4MnGe_2S_7$ is more complicated than that of Cu_2MnGeS_4. An analogous view of the cation ordering of $Cu_4MnGe_2S_7$ along the *b*-axis is shown in Figure 3.4b. Like the cation ordering pattern of Cu_2MnGeS_4, rows of the same metal-sulfur tetrahedra are observed along the *b*-axis of $Cu_4MnGe_2S_7$. The repeating pattern across the figure (left to right) is much larger in comparison to Cu_2MnGeS_4, and is comprised of seven metal-sulfur tetrahedra. This pattern consists of a repeating sequence of CuS_4, MnS_4, CuS_4, GeS_4, CuS_4, CuS_4, GeS_4, which is not repeated until four rows down. To view the entire repeating pattern, a section of 7 x 4 metal-sulfur tetrahedra is therefore necessary.

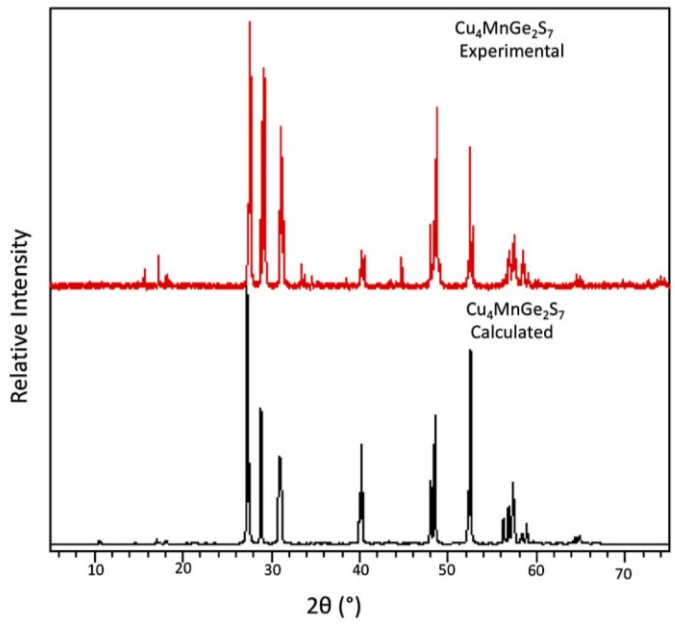

Figure 3.6: XRPD pattern comparison of the collected and the calculated patterns for $Cu_4MnGe_2S_7$, red and black, respectively.

Since the cation ordering patterns in Cu_2MnGeS_4 and $Cu_4MnGe_2S_7$ differ the connectivity of the various MS_4 tetrahedra also differ, Figure 3.5. In the Cu_2MnGeS_4 structure, the GeS_4 and MnS_4 tetrahedra are isolated from one another, while the CuS_4 tetrahedra create a two-dimensional structure in the ac-plane by corner sharing. Conversely, the

CuS_4 tetrahedra of $Cu_4MnGe_2S_7$ form a three-dimensional network through corner sharing, while the GeS_4 tetrahedra form dimers, $[Ge_2S_7]^{6-}$.

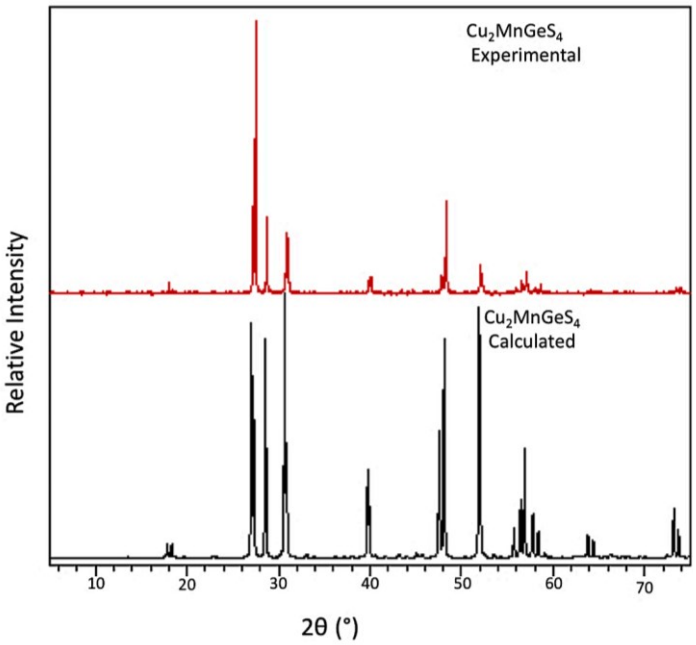

Figure 3.7: XRPD pattern comparison of the collected and the calculated patterns for Cu_2MnGeS_4, red and black, respectively.

3.3.2 X-ray Powder Diffraction (XRPD)

The phase purity of both $Cu_4MnGe_2S_7$ and Cu_2MnGeS_4 was assessed through the collection of XRPD patterns. Figures 3.6 and 3.7 compare the XRPD pattern for the collected data with a calculated XRPD pattern generated from the single crystal data and the data reported by Bernert et. al. (*52*) for $Cu_4MnGe_2S_7$ and Cu_2MnGeS_4, respectively. All the peaks from the collected data of $Cu_4MnGe_2S_7$ match with those calculated, indicating that the material is phase pure. The powder pattern for Cu_2MnGeS_4 contains two unaccounted for peaks at 13.75 and

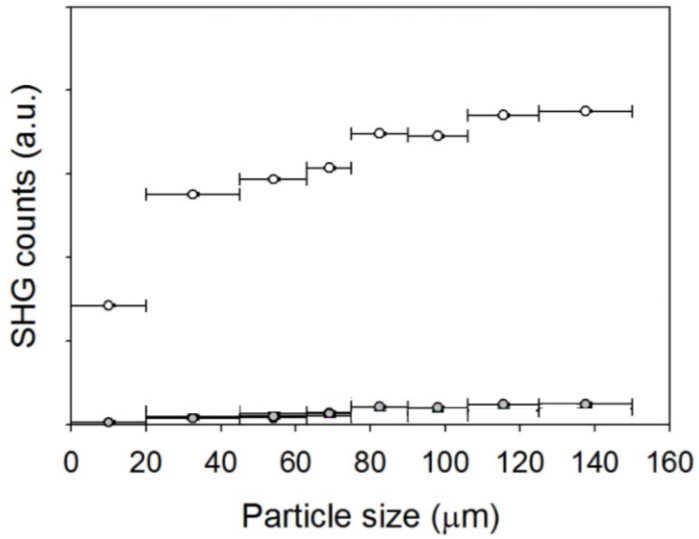

Figure 3.8: SHG counts as a function of particle size with incident λ=3100 nm for Cu_2MnGeS_4 and $AgGaSe_2$ shown in grey and open circles, respectively.

19.80° 2θ, which could not be matched with any known phase; therefore, the sample of Cu_2MnGeS_4 that was used for the property measurements was not completely phase pure.

3.3.3 Second-Harmonic Generation (SHG) and Phase Matchability

Figure 3.8 shows the PM behavior of Cu_2MnGeS_4 and the reference, AGSe, at 3100 nm. Both the diamond-like semiconductor and the reference material are PM. This is evident because the SHG counts increase with increasing particle size. It should be noted that the type of phase matching cannot be determined using the Kurtz-Perry powder technique. The wavelength of 3100 nm was ideal to estimate the $\chi^{(2)}$ of the sample, since both the sample and the reference are PM and do not undergo any multiphoton absorption effects at this wavelength. Then $\chi^{(2)}$, far away from any optical resonance, is purely real with normal dispersion, i.e., the imaginary part of $\chi^{(2)}$ is negligible. Using the Kurtz-Perry powder method, (*70*) the near-static value of $\chi^{(2)}$ can be calculated by comparing with the reference;

$$\chi_S^{(2)} = \chi_R^{(2)} \left(\frac{I_S^{SHG}}{I_R^{SHG}}\right)^{1/2}, \qquad (1)$$

where I_S^{SHG} and I_R^{SHG} are the experimentally measured SHG counts from the sample and the reference, respectively. Using the $\chi^{(2)}$ value of 66 pm/V for AGSe, (*71,72*) the $\chi^{(2)}$ of Cu_2MnGeS_4 was estimated to be 16.9 ± 2.0 pm/V. While this value is markedly lower than AGSe, it is on-par with the commercially available $LiInS_2$ and $LiInSe_2$, which have $\chi^{(2)}$ values reported in the ranges of ~6-15 pm/V (*73-76*) and ~17-22 pm/V (*75,77*) respectively. In comparison, the $\chi^{(2)}$ values of the related compounds $Li_2CdGeSe_4$ and $Li_2CdSnSe_4$ with similar bandgaps of 2.5 eV and 2.2 eV, are slightly higher at 25.6 and 25.3 pm/V, respectively. (*78*) The $\chi^{(2)}$ value for Cu_2MnGeS_4 is

considerably higher than that of the wider bandgap compound, Li_2MnGeS_4, which has a $\chi^{(2)}$ value of 6.6 pm/V. (*26*)

Figure 3.9 shows the SHG data as a function of particle size for $Cu_4MnGe_2S_7$ as compared to the optical-quality AGSe reference material. At this incident wavelength, both the sample and the reference are non-PM, as the measured SHG counts decrease with increasing particle size. However, interestingly, $Cu_4MnGe_2S_7$ shows a slight increase for the particle sizes larger than 63-75 μm, which may correspond to an oscillating PM factor. A comparison to AGSe suggests that the coherence length of $Cu_4MnGe_2S_7$ is longer than that of AGSe. The experimental coherence length could not be determined but should be smaller than 20 μm. Using the Kurtz powder method, (*70*) the near-static value of $\chi_S^{(2)}$ of the sample can be calculated by comparing with the reference, simply assuming the same coherence length of the sample and the reference, using Equation 1. This calculation yields $\chi_S^{(2)}$ ~1.63 ± 0.17 pm/V at the smallest particle size. As $Cu_4MnGe_2S_7$ shows oscillation (Figure 3.9), Equation (1) is not quite precise, because the coherence lengths are different for the sample and the reference. In Figure 3.9, we therefore plot the $\chi_S^{(2)}$ values calculated for every size of AGSe and $Cu_4MnGe_2S_7$. It shows a rather significant uncertainty with the mean value being 2.33 ± 0.86 pm/V.

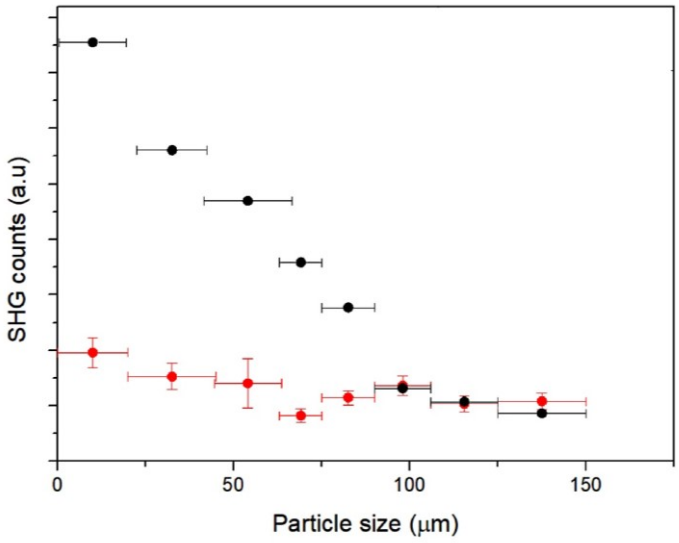

Figure 3.9: SHG counts as a function of particle size with incident λ=1600 nm for $Cu_4MnGe_2S_7$ and $AgGaSe_2$ displayed in red and black respectively. $AgGaSe_2$ is scaled down by a factor of 420.

Although the SHG response of Cu_2MnGeS_4 is on par with several commercially available materials and new IR-NLO candidates, it is a poor performer based on its bandgap energy. It has been observed that the $\chi^{(2)}$ of a sample is inversely proportional to its bandgap energy with some power exponents. In a study by Jackson and coworkers, NLO data from 53 compounds were considered and the authors proposed that, while a single power law expression could not be used to fit all data, 95% of the data points on a plot of $\chi^{(2)}$ versus bandgap energy could be predicted using two power laws within a factor of 4. (*79*) The energy intervals for the two power laws are 0 to 1.2 eV and 1.2 to 8.4 eV. Jackson and coworkers went further to state that when the experimentally measured $\chi^{(2)}$ of the sample differs from the prediction by less than a factor of 2, the sample is considered an average performer in terms of bandgap; however, if the $\chi^{(2)}$ calculated via experiment deviates from what is predicted by more than a factor of 2, it is considered to be a weak performer based on its bandgap value. Using Jackson's equation for the wider bandgap samples, ($\chi^{(2)} = (501)E^{-2.7}$ where is $\chi^{(2)}$ in units of pm/V and E is energy expressed in eV), (*79*) AGSe is predicted to have a $\chi^{(2)}$ of 115 pm/V; therefore, the actual value is off by a factor of 1.75 making AGSe an average-to-weak performer. On the other hand, Cu_2MnGeS_4 is considered a very weak performer because the calculated $\chi^{(2)}$ value of nearly 68 pm/V, differs from the experimentally determined value by a factor of ~4. The experimentally determined $\chi^{(2)}$ for $Cu_4MnGe_2S_7$ is far away from the predicted value; in fact, the compound is one of the weakest performers of all the quaternary diamond-like semiconductors that we have studied to date. Only one other quaternary DLS with the 4-1-2-7 stoichiometry has been studied to date in terms of NLO properties. (*49*) While a $\chi^{(2)}$ value was not determined in that study, $Li_4HgGe_2S_7$ boasts an impressive SHG response of 1.5 x AGSe using incident radiation of 2.09 μm. Even taking into

account that the authors in this study likely used a homemade AGSe reference, the SHG is still very strong for this compound with E_g=2.75 eV.

3.3.4 Laser-Induced Damage Threshold (LIDT)

To determine the LIDT of Cu_2MnGeS_4, the SHG counts for the sample with the largest particle size ($d = 137.5 \pm 12.5$ μm) were measured as a function of input intensity (I) at 1064 nm, Figure 3.10. It should be noted that AGSe is two-photon active at this incident wavelength. In fact, we have observed highly efficient photoluminescence (PL) emission driven by two-photo absorption (2PA) for this sample, where the emission edge is consistent with its bandgap energy of 1.72 eV (~720 nm). The black line in Figure 3.10 signifies the ideal case, ($I_{SHG} \propto I^2$), when no damage occurs, i.e. there is no loss of expected SHG signal due to 2PA or other absorption effects. Clearly, however, the collected SHG counts appreciably diverge from the black line, indicating that 2PA is quite significant. We estimated the 2PA coefficient (β) of AGSe by fitting the experimental data using a simple model given by

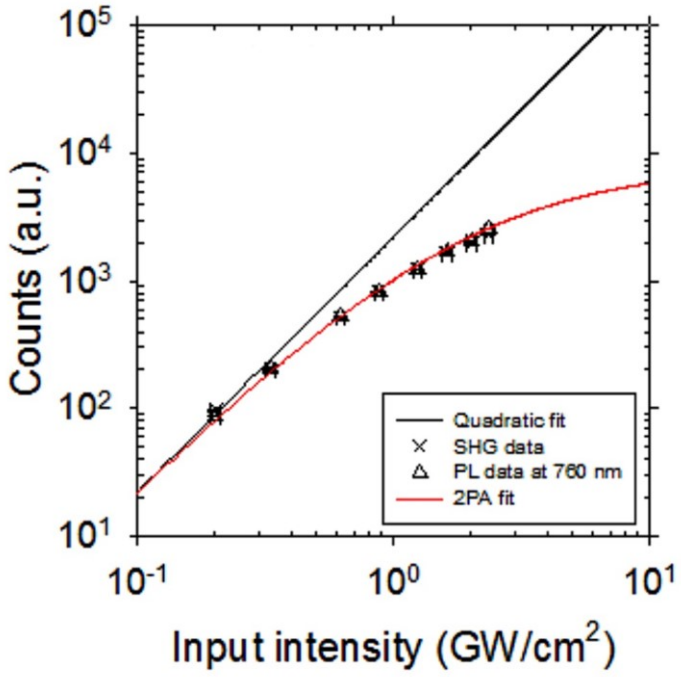

Figure 3.10: SHG counts as a function of input pulse energy of $AgGaSe_2$.

$$I_{SHG} = a\left(\frac{I}{1+\beta dI}\right)^2, \qquad (2)$$

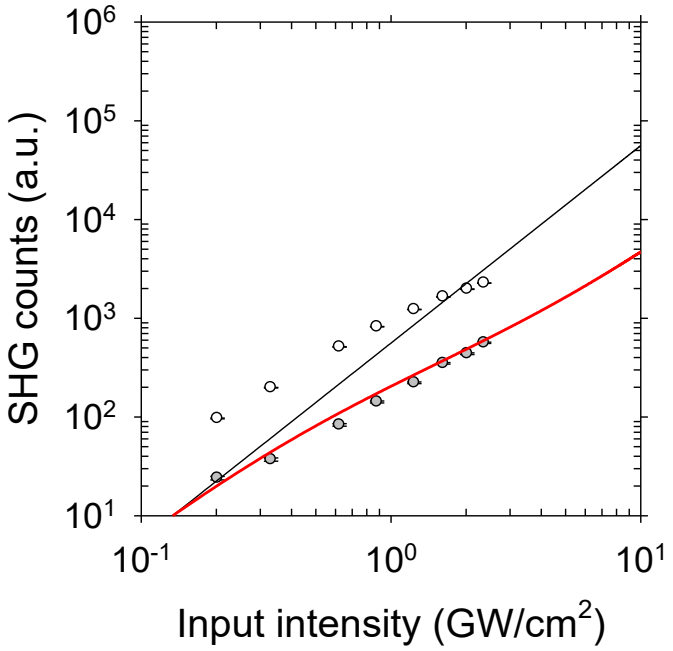

Figure 3.11: SHG counts as a function of input pulse energy of $AgGaSe_2$ and Cu_2MnGeS_4 displayed in white and grey, respectively.

where a is the proportionality constant capturing the second-order nonlinearity and $d = 137.5 \pm 12.5$ μm is the particle size for our reflection geometry. (*80*) The fit value of $\beta = 40.0 \pm 3.4$ cm/GW agrees well with our previous measurements for AGSe, (*27,81*) as well as a theoretical value predicted by a two-band model within a factor of 2. (*82*) The input intensity where the 2PA fit noticeably deviates from the black line can be assigned to a LIDT of about 0.2 GW/cm^2 for AGSe. Figure 3.11 shows the SHG counts for Cu_2MnGeS_4 under the same experimental setup. The SHG response of Cu_2MnGeS_4 is weaker than that of AGSe, which is reasonable considering that Cu_2MnGeS_4 has a wider bandgap. The LIDT of Cu_2MnGeS_4 is unfortunately poor, about two times lower than that of AGSe based on the 2PA coefficient estimated below. However, the material displays salient saturable absorption (SA). To fit the overall trend, we modified Eq. (2) by incorporating the effect of SA,

$$I_{SHG} = a\left(\frac{I}{1 + \beta d I/(1 + I/I_s)}\right)^2, \qquad (3)$$

where I_s is an additional fitting parameter known as the saturation intensity. The intensity-dependent SHG data were fit using Eq. (3), yielding $\beta = 85.0 \pm 5.4$ cm/GW and $I_s = 3.4$

GW/cm^2. We confirmed that Cu_2MnGeS_4 does not exhibit any PL under 2PA, implying that relaxation pathways of optical excitation are basically nonradiative.

3.3.5 Optical Diffuse Reflectance UV-vis-NIR Spectroscopy

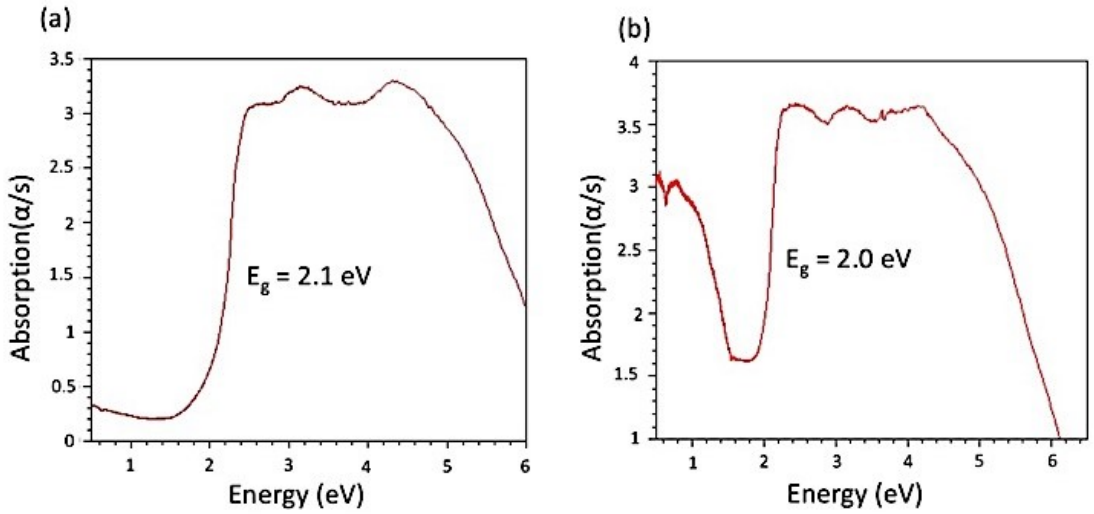

Figure 3.12: UV-vis-NIR spectra of (a) Cu_2MnGeS_4 and (b) $Cu_4MnGe_2S_7$.

The optical diffuse reflectance UV-vis-NIR spectra were collected to estimate the bandgaps of both $Cu_4MnGe_2S_7$ and Cu_2MnGeS_4. The reflectance data were converted to absorption using the Kubelka-Munk transformation (*61*) and plotted as a function of energy (eV), Figure 3.12. The bandgaps of each sample were determined by identifying the absorption edge and extrapolating it to the baseline. The optical bandgap of $Cu_4MnGe_2S_7$ was found to be 2.0 eV. The bandgap of Cu_2MnGeS_4 is slightly larger at 2.1 eV. This result is in good agreement with Chen and coworkers who determined the optical bandgap of Cu_2MnGeS_4 to be 2.035 eV, which was obtained from absorption spectra collected from a cut and polished single crystal. (*83*)

3.3.6 Electronic Structure

The calculated band structure as well as the total and partial densities of states of $Cu_4MnGe_2S_7$ are displayed in Figure 3.13. The spin-up and spin-down calculations are very similar

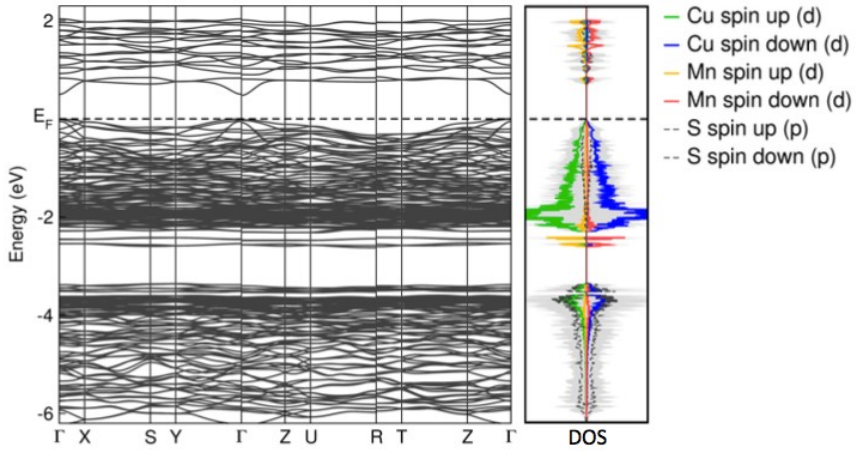

Figure 3.13: Calculated band structure, total and partial density of states for $Cu_4MnGe_2S_7$. The contribution from Ge is significantly smaller than the other atomic species within this energy window and is therefore not shown in the figure.

and in both cases the valence band maximum is dominated by the copper orbital contributions, while the conduction band minimum is a product of the manganese orbitals. In comparison, the valence band maximum is also due to the copper orbitals and the conduction band minimum is a result of the manganese orbitals for Cu_2MnGeS_4, Figure 3.14.

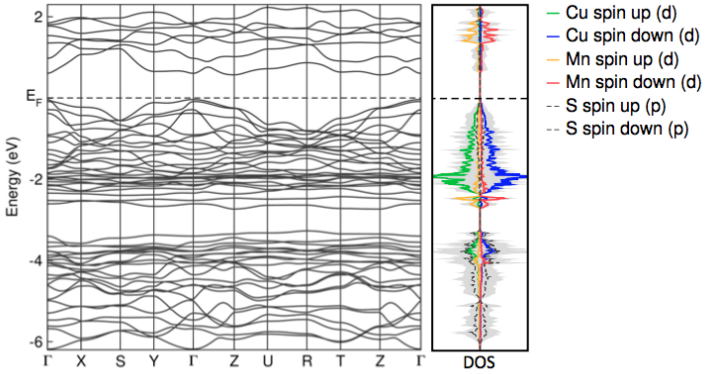

Figure 3.14: Calculated band structure, total and partial density of states for Cu_2MnGeS_4. The contribution from Ge is significantly smaller than the other atomic species within this energy window and is therefore not shown in the figure.

3.3.7 Optical Transparency at IR

The optical transparency ranges of $Cu_4MnGe_2S_7$ and Cu_2MnGeS_4 were determined using FT-IR spectroscopy, Figure 3.15. In both cases, the FT-IR spectra are devoid of peaks except for two at 4.5 and

15.5 μm, which can be accounted for by CO_2 resulting from the data collection method. Both $Cu_4MnGe_2S_7$ and Cu_2MnGeS_4 were determined to have a transparency window of approximately ~4.5-25 μm with transparency of ~70%, and 60%, respectively. In both cases, the window of transparencys appears to continue further than the detection limit of FT-IR (25 μm), which suggests that these materials could have use as THz generators.

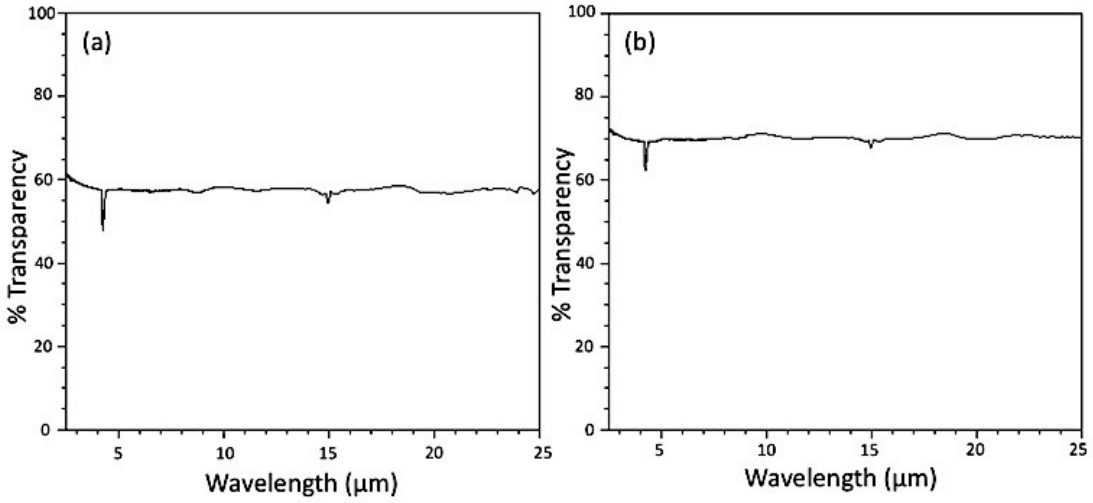

Figure 3.15: FT-IR spectra of (a) Cu_2MnGeS_4 and (b) $Cu_4MnGe_2S_7$.

3.3.8 Differential Thermal Analysis (DTA)

Differential thermal analysis was conducted to study the thermal behaviour of the two diamond-like semiconductors. Figure 3.15 displays the first DTA cycle for each compound. It was determined that Cu_2MnGeS_4 melts incongruently at 830 °C, Figure 3.16a. The X-ray powder diffraction pattern of the DTA residue shows that Cu_2MnGeS_4 is the predominant phase after DTA; however, there are two additional diffraction peaks that appear that could not be assigned to any known phase, appearing around 38.5 and 44.5° 2θ. Likewise, $Cu_4MnGe_2S_7$ appears to melt incongruently, however, at higher temperature, ~977 °C, Figure 3.16 b. The peak at ~966 °C in the cooling cycle has been tentatively assigned to the recrystallization temperature. The X-ray powder diffraction pattern of the DTA residue shows that the sample is still mainly $Cu_4MnGe_2S_7$;

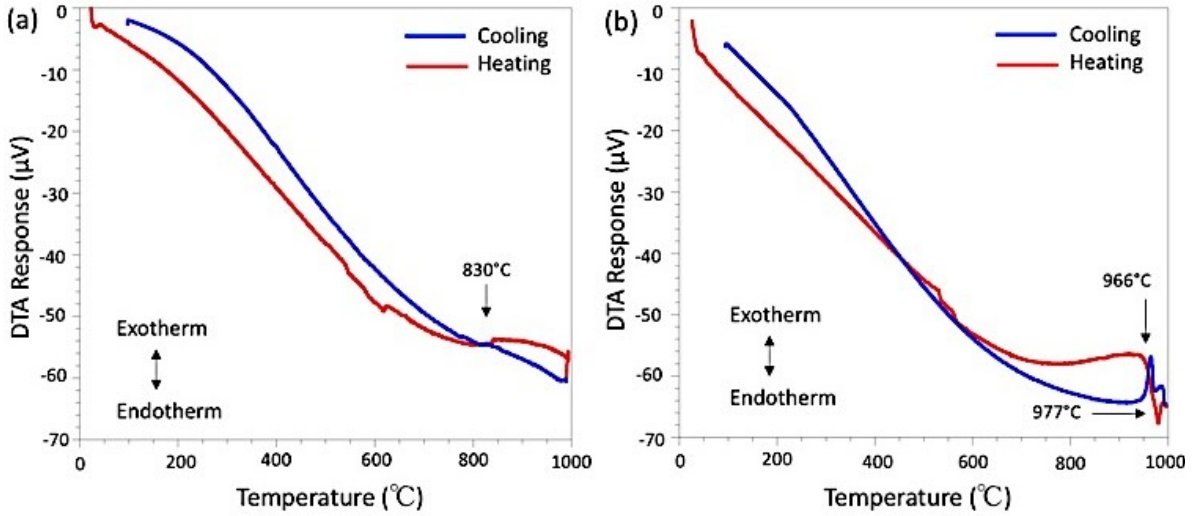

Figure 3.16: Differential thermal analysis of (a) Cu_2MnGeS_4 and (b) $Cu_4MnGe_2S_7$.

however, Cu_2GeS_3 (*55*) and CuS (*84*) are clearly present as well as the same unidentified peaks that were observed for Cu_2MnGeS_4. The differences in DTA results are not surprising, as the maximum temperature used to synthesize $Cu_4MnGe_2S_7$ is 225 °C higher than that used for Cu_2MnGeS_4. The second DTA cycle for both compounds displayed additional exotherms and endotherms.

3.4. Conclusions

Since Cu_2MnGeS_4 is phase matchable with a reasonably strong $\chi^{(2)}$ value, it has potential for wave-mixing applications in the mid-IR, although it is not a top candidate for high-powered laser applications due to the relatively low LIDT albeit an order of magnitude larger than that of AGSe. The $\chi^{(2)}$ value for Cu_2MnGeS_4 is greater than that reported for $LiInS_2$, and $LiInSe_2$, which are commercially available. (73-76) The $\chi^{(2)}$ value for $Cu_4MnGe_2S_7$ is a lot lower than Cu_2MnGeS_4, AGSe and other compounds that are commercially available for IR-NLO applications. In fact, the response of $Cu_4MnGe_2S_7$ is one of the lowest of all the quaternary DLSs that we have investigated

to date. Nevertheless, $Cu_4MnGe_2S_7$ and Cu_2MnGeS_4, both have wide ranges of optical transparency and high thermal stability.

3.5 References

(1) Hopkins, F.K., *Opt. Photonics News*, **1998**, *9*, 32-38.

(2) Hecht, J., *Laser Focus World*, **2014**, *50*, 31-38.

(3) Knuteson, D.J.; Singh, N.B.; Kanner, G.; Berghmans, A.; Wagner, B.; Kahler, D.; McLaughlin, S.; Suhre, D.: Gottlieb, M., *J Cryst. Growth*, **2010**, *312*, 1114-1117.

(4) Miller, M.J.; Mott, A.G.: Ketchel, B.P., *Proc. SPIE*, **1998**, *3472*, 24-29.

(5) Zuclich, J.A.; Lund, D.J.;. Stuck, B.E., *Health Phys.*, **2007**, *92*, 15-23.

(6) Clewes, R.J.; Howle, C.R.: Stothard, D.J.M.: Dunn, M.H.; Robertson, G.; Miller, W.; Malcolm, G.; Maker, G.; Cox, R.; Williams, B.; Russell, M., *Proc. SPIE*, **2012**, *8456*, 85460X.

(7) Todd, M.W.; Provencal, R.A.; Owano, T.G.; Paldus, B.A.; Kachanov, A.; Vodopyanov, K.L.; Hunter, M.; Coy, S.L.; Steinfeld,J.I.; Arnold, J.T., *Appl. Phys. B*, **2002**, *75*, 367-376.

(8) Stoeppler, G.; Schellhorn, M.; Eichhorn, M., *Laser Physics*, **2012**, *22*, 1095-1098.

(9) Haidar, S.; Miyamoto, K.; Ito, H., *Optics Comm.*, **2004**, *241*, 173-178.

(10) Aitken, J.A.; Brant, J.A.; Clark, D.J.; Kim, Y.S.: Jang, J.I., "Impact of bandgap on infrared optical nonlinearity in novel quaternary chalcogenides: Cu_2CdSnS_4, α/β-Cu_2ZnSiS_4 and Li_2CdGeS_4." *Nonlinear Optics: Fundamentals, Applications, and Technological Advances*; Wilkins, F.; NOVA Science Publishers, UK, **2014,** 1-61.

(11) Wang, C.; Sahay, P., *Sensors*, **2009**, *9*, 8230-8262.

(12) Persijn, S.; Harren, F.: vander Veen, A., *Appl. Phys. B*, **2010**, *100*, 383-390.

(13) Catella, G.C.; Burlage, D. *MRS Bull.,* **1998**, *23*, 28-36.

(14) Schunemann, P.G.; Pollak, T.M., *MRS Bull.,* **1998**, *23*, 23-27.

(15) Giles, N.C.; Bai, L.; Chirila, M.M.; Garces, N.Y.; Stevens, K.T.; Schunemann, P.G.; Setzler, S.D.; Pollak, T.M., *J. Appl. Phys.*, **2003**, *93*, 8975.

(16) Wood, R.M. *Laser-induced Damage in Optical Materials*, Hilger, Boston, **1986**.

(17) Harasaki, A.; Kiyoshi, K., *Jpn. J. Appl. Phys.*, **1997**, *36*, 700-703.

(18) Bhar, G.C.; Smith, R.C., *Phys. Stat. Sol.*, **1972**, *13*, 157-168.

(19) Boyd, G.D.; Buehler, E.; Storz, F.G., *Appl. Phys. Lett.*, **1971**, *18*, 301-304.

(20) Li, Y.-T.; Lui, F.-P.; Hu, L.; Chen, L.; Lin, H.; Zhou, L.-J.; Wu, L.-M., *Adv. Optical Mater.,* **2015**, *3*, 957-966.

(21) Yao, J.; Mei, D.; Bai, L.; Lin, Z.; Yin, W.; Fu, P.; Wu, Y., *Inorg. Chem.*, **2010**, *49*, 9212-9216.

(22) Wu, K.; Yang, Z.; Pan, S., *Chem. Mater.*, **2016**, *28*, 2795-2801.

(23) Bera, T.K.; Jang, J.I.; Song, J.-H.; Malliakas, C.D.; Freeman, A.J.; Ketterson, J.B.; Kanatzidis, M.G., *J. Am Chem. Soc.*, **2010**, *132*, 3484-3495.

(24) Wu, K.; Pan, S., *Crystals*, **2017**, *7*, 107.

(25) Wu, K.; Yang, Z.; Pan, S., *Chem. Commun.*, **2017**, *53*, 3010.

(26) Brant, J.A.; Clark, D.J.; Kim, Y.S.; Jang, J.I.: Weiland, A.; Aitken, J.A., *Inorg. Chem.*, **2015**, *54*, 2809-2819.

(27) Brant, J.A.; Clark, D.J.; Kim, Y.S.; Jang, J.I.: Zhang, J.-H.; Aitken, J.A., *Chem. Mater.*, **2014**, *26*, 3045-3048.

(28) Rosmus, K.A.; Brant, J.A.; Wisneski, S.D.; Clark, D.J.; Kim, Y.S.; Jang, J.I.; Brunetta, C.D.; Zhang, J.-H.; Srnec, M.N.; Aitken, J.A. *Inorg. Chem.*, **2014**, *53*, 7809-7811.

(29) Wu, Q.; Meng, X.; Zhong, C.; Chen, X.; Qin, J., *J. Am. Chem. Soc.*, **2014**, *136*, 5683-5686.

(30) Guangmao, L.; Wu, K.; Liu, Q.; Yang, Z.; Pan, S., *J. Am. Chem. Soc.*, **2016**, *138*, 7422-7428.

(31) Chung, I.; Song, J.-H.; Jang, J.I.; Freeman, J.A.; Kanatzidis, M.G., *J. Solid State Chem.*, **2012**, *195*, 161-165.

(32) Luo, Z.-Z.; Lin, C.S.; Zhang, W.-L.; Zhang, H.; He, Z.-Z., *Chem. Mater.*, **2014**, *26*, 1093-1099.

(33) Zhang, G.; Li, Y.; Jiang, K.; Zeng, H.; Lui, T.; Chen, X.; Qin, J.; Lin, Z.; Fu, P.; Wu, Y.; Chen, C., *J. Am. Chem. Soc.*, **2012**, *134*, 14818-14822.

(34) Li, X.; Li, C.; Gong, P.; Lin, Z.; Yao, J.; Wu, Y., *J. Mater. Chem.*, **2015**, *3*, 10998.

(35) Zhen, N.; Wu, K.; Wang, Y.; Li, Q.; Gao, W.; Hou, D.; Yang, Z.; Jiang, H.; Dong, Y.; Pan, S., *Dalton Trans*, **2016**, *45*, 10681.

(36) Wu, K.; Su, X.; Pan, S.; Yang, Z., *Inorg. Chem.*, **2015**, *54*, 2772-2779.

(37) Lin, H.; Chen, L.; Zhou, L.-J.; Wu, L.-M., *J. Am. Chem. Soc.*, **2013**, *135*, 12914-12921.

(38) Lin, H.; Zheng, Y.-J.; Hu, X.-N.; Chen, H.; Yu, J.-S.; Wu, L.-M., *Chem. Asian J.*, **2017**, *12*, 453-458.

(39) Liang, F.; Kang, L.; Lin, Z.; Wu, Y., *Cryst. Growth Des.*, **2017**, *17*, 2254-2289.

(40) Chung, I.; Kanatzidis, M.G., *Chem. Mater.*, **2014**, *26*, 849-869.

(41) Shi, Y.-F.; Chen, Y.; Chen, M.-C.; Wu, L/-M.; Lin, H.; Zhou, L.-J.; Chen, L., *Chem. Mater.*, **2015**, *27*, 1876-1884.

(42) Parthé, E., *Crystal Chemistry of Tetrahedral Structures*, Gordon and Breach Science Publishing, New York, NY, **1964**.

(43) Goryunova, N.A., *The Chemistry of Diamond-like Semiconductors*, The MIT Press, Cambridge MA, **1964**.

(44) Pauling, L., *J. Am. Chem. Soc.*, **1929**, *51*, 1010-1026.

(45) Pamplin, B, *Prog. Cryst. Growth Charact.*, **1981**, *3*, 179-192.

(46) Pamplin, B., *J. Phys. Chem. Solids.*, **1964**, *25*, 675-684.

(47) West, A.R., *Solid State Chemistry and its Applications*, John Wiley & Sons Ltd., London, UK, **2004**.

(48) Kaib, T.; Haddadpour, S.; Andersen, H.F.; Mayrhofer, L.; Järvi, T.T.; Moseler, M.; Möller, K.-C.; Dehnen, S., *Adv. Funct. Mater.*, **2013**, *23*, 5693-5699.

(49) Wu, K.; Yang, Z.; Pan, S., *Chem. Commun.*, **2017**, *53*, 3010-3013.

(50) Gulay, L.D.; Olekseyuk, I.D.; Parasyuk, O.V., **2002**, *340*, 157-166.

(51) Schäfer, W.; Scheunemann, K.; Nitsche, R., *MRS. Bull.*, **1980**, *15*, 933-937.

(52) Bernert, T.; Pfitzner, A., *Z. Kristallogr.,* **2005**, *220*, 968-972.

(53) Chen, X.L.; Lamarche, A.-M.; Lamarche, G.; Woolley, J.C., *J. Phys.: Condens. Matter*, **1993**, *5*, 7143-7154.

(54) Chourio, M.; Romero, H.; Betancourt, L.; Sargredo, V., *Crystal Frowth and Magnetic Properties of the Cu_2MnGeS_4 Semiconductor, In: Morán-López J.L., Sanchez J.M. (eds) New Trends in Magnetism Materials, and Their Applications.* Springer, Boston MA, **1994**.

(55) De Chalbaud, L.M.; Diaz de Delgado, G.; Delgado, J.M.; Mora, A.E.; Sagredo, V., *Mat. Res. Bull.*, **1992**, *32*, 1371-1376.

(56) SAINT and SADABS are part of the Apex2 software package v2.1-4 Program for Data Collection and Reduction on Bruker AXS CCD Area Detector Systems. *Apex2 software package v2.1-4*; Bruker Analytical X-ray Systems, Inc., Madison, WI, **2005**.

(57) SHELXTL, release 6.14; Bruker AXS; Madison, WI, **2005**.

(58) CrystalMaker, version 9, CrystalMaker Software Limited, Oxfordshire, UK.

(59) X.p.H. Plus, PANalytical. B.V., Almelo, the Netherlands.

(60) J. Faber and T. Fawcett, Acta Crystallogr., Sect. B: Struct. Sci., 2002, 58, 325–332

(61) Džimbeg-Malčić, V.; Barbarić-Mikočević, Ž.; Itrić, K., *Technical Gazette*, **2011**, *18*, 117-124.

(62) Perdew, J.P.; Burke, K.; Ernzerhof, M., *Phys. Rev. Lett.*, **1996**, *77*, 3865.

(63) Kresse, G.; Furthmüller, J. *Phys. Rev. B*, **1996**, *54*, 11169.

(64) Kresse, G.; Joubert, D., *Phys. Rev. B*, **1999**, *59*, 1758.

(65) Blöchl, P.E., *Phys. Rev. B.*, **1994**, *50*, 17953.

(66) Measurement Methods for Powder Samples: Shimadzu (Shimadzu Corporation), http://www.shimadzu.com/an/ftir/support/ftirtalk/talk8/intro.html

(67) Dogguy, P.M.; Jaulmes, S.; Laruelle, P.; Rivet, J., *Acta Cryst.,* **1982**, *B38m*, 2014-2016.

(68) Dogguy, M., *Mater. Chem. Phys.*, **1983**, *9*, 405-412.

(69) Parthé, E.; Yvon, K.; Deitch, R.H., *Acta. Cryst.*, **1969**, *B25*, 1164-1174.

(70) Kurtz, S.K.; Perry, T.T., *J. Appl. Phys.* **1968**, *39*, 3798-3813.

(71) Nikogosyan, D.N., "*Nonlinear optical crystals: A complete survey*", 1st edition, Springer, New York, **2005**.

(72) Bhar, G.C., *Jpn. J. Appl. Phys. Part I, Supplement,* **1993**, *32*, 653–659.

(73) Yelisseyev, A.; Isaenko, L.; Lovanov, S.; Zondy, J.-J., in Advanced Solid State Lasers, Eds. Injeyan, H; Marshall, C., Vol 34 of OSA Trends in Optics and Photonics Series Optical Society of America: Washington, D. C., **2000**, 561–569.

(74) Boyd, G.D.; Kasper, H.M.; MacFee, J.H., *J. Appl. Phys.*, **1973**, *44*, 2809–2812.

(75) Chen, W.; Cousin, J.; Sigrist, M.W.; Gao,X.; Zondy, J.-J.; Isaenko, L.; Yelisseyev, A.; Lobanov, S., Lasers and Electro-Optics Society, 2006. 19th Annual Meeting of the IEEE, Oct., **2006** (Montreal Canada) 88–89.

(76) Knippels, G.M.H.; van der Meer, A.F.G.; MacLeod, A.M.; Yelisseyev, A.; Isaenko, L.; Lobanov, S.; Thénot, I.; Zondy, J.-J., *Opt. Lett.*, **2001**, *26*, 617–619.

(77) Ebrahim-Zadeh, M., "Mid-infrared optical parametric oscillators and applications" in *NATO Science for Peace and Security Series B: Physics and Biophysics. Mid-Infrared Coherent Sources and Applications*, Eds. Ebrahim-Zadeh, M; Gorokina, IT. Springer: Dordrecht, The Netherlands, **2008**, 347–375.

(78) Zhang, J.-H.; Clark, D.J.; Weiland, A.; Stoyko, S.S.; Kim, Y.S.; Jang, J.I.; Aitken, J.A., *Inorg. Chem. Front*, **2017**, *4*, 1472-1484.

(79) Jackson, A.J.; Ohmar, M.C.; LeClair, S.R., *Infrared Phys. Technol.*, **1997**, *38*, 233-244.

(80) Jang, J.I.; Park, S.; Harrison, C.M.; Clark, D.J.; Morris, C.D.; Chung, I.; Kanatzidis, M.G., *Opt. Lett*, **2013**, *38*, 1316-1318.

(81) Saouma, F.O.; Stoumpos, C.C.; Wong, J.; Kanatzidis, M.G.; Jang, J.I., *Nature Commun*., **2017**, *8*, 742.

(82) Sheik-Bahae, M.; Hutchings, D.C.; Hagan, D.; van Stryland, E.W., *IEEE J. Quantum Electron*., **1991**, *27*, 1296–1309

(83) Chen, X.L.; Lamarche, A.-M.; Lamarche, G.; Woolley, J.C., *J. Pys.: Condens. Matter*, **1993**, *5*, 7143-7154.

(84) Kazinets, M.M., *Kristallogratiya*, **1970**, *14*, 704.

Chapter 4: Crystal and Electronic Structure of $Cu_4CdSi_2S_7$: A New Diamond-like Semiconductor that Violates Pauling's Second Rule

4.1 Introduction

Diamond-like semiconductors (DLSs) are an attractive class of materials due to the predictability of their structures and formulae, which can be determined using several guidelines. For common DLSs such as the I_2-II-IV-VI_4 materials, four principles can be employed, while only three of these apply to the slightly distorted I_4-II-IV_2-VI_7 DLSs, such as the title compound. The roman numerals in the above formulae represent the valence of the elements.

The structures of all DLSs are derived from the structure of either cubic or hexagonal diamond. (1,2) To begin, all of the atoms must be tetrahedrally coordinated and by nature of being diamond-like, all of the tetrahedral units must align along one crystallographic direction. (1,2) The valence electron rules require that the average number of valence electrons equals four and the average number of valence electrons per anion is eight. (1-3) In the case of the common DLSs, the material should also follow Pauling's second rule, which states that the charges of the anions are compensated by the valence bonds of the cations within the first coordination sphere. (4) However, Pauling's second rule is not followed by I_4-II-IV_2-VI_7 DLSs and the number of diamond-like phases in violation of Pauling's second rule, such as the title compound are steadily growing. Table 4.1 lists all of the I_4-II-IV_2-VI_7 (*5*-*8*) DLS discovered to date and their counterpart I_2-II-IV-VI_4 (*3*,*9*-*14*) DLSs that have been reported.

Table 4.1: I_4-II-IV_2-VI_7 DLSs and their I_2-II-IV-VI_4 counterparts.

I_4-II-IV_2-VI_7 DLS	Space Group	Reference	I_2-II-IV-VI_4 DLS	Space Group	Reference
$Li_4MnGe_2S_7$	C*c*	*5*	Li_2MnGeS_4	P*na*2_1	*9*
$Li_4MnSn_2S_7$	C*c*	*5*	Li_2MnSnS_4	P*na*2_1 P*n*	*10*
$Li_4HgGe_2S_7$	C*c*	*6*	Li_2HgGeS_4	P*na*2_1	*11*
$Ag_4HgGe_2S_7$	C*c*	*7*	Ag_2HgGeS_4	P*na*2_1	*12, 13*
$Ag_4CdGe_2S_7$	C*c*	*7*	Ag_2CdGeS_4	P*na*2_1 P*mn*2_1	*3, 14*
$Cu_4NiSi_2S_7$	C2	*8*			
$Cu_4NiGe_2S_7$	C2	*8*			
$Cu_4CdSi_2S_7$	Cc	This Work	Cu_2CdSiS_4	P*na*2_1	*5*

The chemical flexibility and stable structure of DLSs also makes them attractive for many applications. DLSs are currently being used in several fields including infrared nonlinear optics (*15-27*), solar cells (*28-32*), and LEDs. (*33-36*) They are also of interest for thermoelectric, (*37-40*) magnetoelectronic, (*41-43*) and spintronic (*44,45*) devices, as well as solid-state electrolytes for lithium-ion batteries. (*46-48*) However, the continued commercial use of DLSs requires greater tunability.

Tunability of DLSs can be achieved several ways. Doping is one traditional way in which the properties of a semiconductor can be tuned. (*49*) Each cation and anion position represents another

opportunity for doping. DLSs have also been tuned through the progression from binary (II-VI) (*50*) to ternary (I-III-VI_2) (*51,52*) and quaternary (I_2-II-IV-VI_4) (*53,54*) materials. (*1,2,55*) Each time another element is added to the formula, another level of adjustability is introduced. Systematic studies are being conducted to reveal structure-property and composition-property correlations in these materials in order to tailor DLSs for particular applications. Altering the stoichiometry of DLSs is an additional way of property tuning that has been underutilized. For example, analogous quaternary DLSs have been synthesized using the I_2-II-IV-VI_4 and I_4-II-IV_2-VI_7 stoichiometries, see Table 4.1. The majority of reported quaternary DLSs are of the I_2-II-IV-VI_4 stoichiometry. The I_4-II-IV_2-VI_7 materials are relatively scarce. To the best of our knowledge, literature comparing I_2-II-IV-VI_4 and I_4-II-IV_2-VI_7 compounds is not available. This is likely due to the limited number of I_4-II-IV_2-VI_7 DLSs that have been encountered thus far, and the fact that many of the I_2-II-IV-VI_4 DLSs reported decades ago were not studied in detail. This work contributes a new member to the growing family of I_4-II-IV_2-VI_7 distorted DLSs. Here, we demonstrate how the change in stoichiometry from I_2-II-IV-VI_4 to I_4-II-IV_2-VI_7 can alter the crystal and electronic structures.

4.2 Experimental

4.2.1 $Cu_4CdSi_2S_7$ Synthesis of Single Crystals

Single crystals of $Cu_4CdSi_2S_7$ were obtained through high-temperature, solid-state synthesis. The reaction was prepared by weighing Cu (4 mmol, 99.999%, Strem), Cd (1 mmol, 99.999%, Strem), Si lump (2 mmol, ground using a diamonite mortar and pestle, 99.999+%, Alfa Aesar) and S (7 mmol, sublimed powder, 99.5%, Fisher Scientific) and grinding the reactants for 10 minute in an agate mortar and pestle. The ground reactants were housed in a carbon-coated tube

(made by pyrolyzing acetone), that was vacuum sealed under a pressure of 10^{-4} mbar in a 12 mm o.d. fused-silica reaction vessel. The vessel was then heated to 1000 °C in 12 hours, held at 1000 °C for 96 hours, and cooled at a rate of 2 °C/hour to room temperature. The products of this reaction included $Cu_4CdSi_2S_7$, Cu_2CdSiS_4, Cu_2SiS_3 and CuS. $Cu_4CdSi_2S_7$ was identified as dark-blue, needle-shaped crystals. Single crystals for X-ray diffraction were selected under an optical microscope.

Table 4.2: Select crystallographic data and experimental details for $Cu_4CdSi_2S_7$.

Chemical Formula	$Cu_4CdSi_2S_7$
Formula Weight (g mole^{-1})	647.16
Temperature (K)	298
Wavelength (Å)	0.71073
Space Group	C*c* (No. 9)
a (Å)	16.5966(6)
b (Å)	6.4052(2)
c (Å)	9.7731(4)
β(°)	93.262(3)
Volume (Å^3)	1037.24(7)
Z	4
D_{calc} (g cm^{-3})	4.144
μ (cm^{-1})	11.663
Flack parameter	0.93(3)
R[I>2σ(I)], R(all data)	0.0393, 0.0474
wR2[I>2 σ (I)], wR2(all data)*	0.0934, 0.0974

$$*wR2 = \left\{\frac{\Sigma\left[w(F_o^2 - F_c^2)^2\right]}{\Sigma\left[w(F_o^2)^2\right]}\right\}^{\frac{1}{2}}, \quad R1 = \Sigma\big||F_o| - |F_c|\big|/\Sigma|F_o|$$

4.2.2 Single-Crystal X-ray Diffraction

The single crystal data for $Cu_4CdSi_2S_7$ were collected with a Bruker SMART Apex 2 CCD single crystal X-ray diffractometer equipped with graphite-monochromatized Mo-$\mathbf{K_\alpha}$ radiation. The tube power was set at 50 kV and 30 mA. The single crystal of $Cu_4CdSi_2S_7$ used for data collection was a dark-blue, needle-like crystal with dimensions of 0.30 x 0.02

x 0.01 mm. The data were collected for 20 seconds per frame over the range of 2.4-27.5° theta. This resulted in the compilation of 2368 reflections of which 2092 were unique with a $R_{(int)}$ of 0.0368. The data were integrated by means of the SAINT program. (*56*) XPREP was used to identify the systematic absences, which suggested two possible space groups, C*c* and C2/*c*. The noncentrosymmetric space group C*c* was selected as all DLSs possess noncentrosymmetric structures. The SAINT program was also used to prepare the files for SHELX, the software package used to solve (SHELXS) and refine (SHELXTL) the structure. (*57*) The structure of $Cu_4CdSi_2S_7$ contains fourteen crystallographically unique atoms, which all reside on general positions. The Flack parameter and extinction coefficient were refined and all atoms were refined anisotropically including the lithium atoms. The pertinent crystallographic data and experimental details are listed in Table 4.2. All the crystal structure figures in this publication were generated using the CrystalMaker software package. (*58*)

4.2.3 X-ray Powder Diffraction

X-ray powder diffraction data were collected using a PANalytical X'Pert Pro MPD X-ray powder diffractometer equipped with the X'cellerator detector and employing Cu K_α radiation with a wavelength of 1.541871 Å. The tube power was 45 kV and 40 mA. Data were collected over the range of 5° to 145° 2θ, with a step size of 0.0085556 and a scan rate of 0.010644 °/s. The incident beam path included a fixed divergent slit at ¼°, a 0.02 radian soller slit and a fixed anti-scatter slit of ½°. The diffracted beam path included a nickel filter, a 0.02 radian soller slit, and a fixed anti-scatter slit of ½°. The samples were prepared by grinding for 5 minutes and then top-filling into a zero-background holder. The crystalline phases present in the sample were identified

using the search match capabilities of the X'Pert HighScore Plus (*59*) software coupled with the International Centre for Diffraction Data (ICDD) powder diffraction file (PDF) database. (*60*)

4.2.4 Scanning Electron Microscopy (SEM) and Energy Dispersive Spectroscopy (EDS)

The morphology of the crystals were investigated by means of SEM. Crystals were adhered to an aluminum specimen stub using conductive carbon tape. A Hitachi S-3400N scanning electron microscope was utilized to collect the micrographs. The working distance was 10 mm, the filament current was 85 kV and the probe current was 80 kV. The micrographs were obtained using an accelerating voltage of 5 kV; however, the accelerating voltage was set to 15 kV for EDS. A Bruker Quantax model 400 energy dispersive spectrometer equipped with an XFlash 5010 EDS detector having a resolution of 129 eV was used to assess an approximate elemental ratio. The EDS spectra were amassed using a three-minute live time.

4.2.5 Electronic Structure Calculations

The electronic structure calculations for both $Cu_4CdSi_2S_7$ and Cu_2CdSiS_4 were completed using the WIEN2K (*61*) software package that employs density functional theory and the full-potential linearized augmented plane wave method. The structures of $Cu_4CdSi_2S_7$ and Cu_2CdSiS_4 used for the calculations were obtained from the single crystal X-ray diffraction data reported in this paper and the work of Chapuis et al., respectively. (*53*) In both cases, no geometry or volume optimizations were performed. The exchange and correlation effects were handled with the Perdew-Burke-Ernzerhof of generalized gradient approximation (PBE-GGA). (*62*) The calculations were performed using 2000 k-points for both $Cu_4CdSi_2S_7$ and Cu_2CdSiS_4,

respectively. The electronic band structure as well as the total and partial density of states (PDOS) were calculated for both compounds.

4.3 Results and Discussion

4.3.1 Crystal Structure

The new DLS $Cu_4CdSi_2S_7$ crystalizes in the noncentrosymmetric, monoclinic space group *Cc* with a structure that can be envisioned as a superstructure of hexagonal diamond. The compound is isostructural to the ternary DLS $Cu_5Si_2S_7$, (*63,64)* in addition to the I_4-II-IV_2-VI_7 compounds that crystalize in the *Cc* space group and are listed in Table 4.1. The first I_4-IV-IV_2-VI_7 compounds reported with this structure type were $Ag_4CdGe_2S_7$ and $Ag_4HgGe_2S_7$, published by Gulay and coworkers in 2002. (*65*) Each unit cell consists of fourteen crystallographically unique atoms, including four copper, one cadmium, two silicon and seven sulfur atoms, all residing on general positions. Each of the metal cations is bound to four sulfur anions and each of the sulfurs is connected to four metal cations. Four of the metal-sulfur tetrahedra consist of a sulfur anion bound to two copper cations, one cadmium cation and one silicon cation. This arrangement results in local charge neutrality, where the cations balance the -2 charge from the sulfur anion, in accordance with Pauling's second rule. The three other sulfurs reside in two different types of environments, where the breakdown of Pauling's second rule results in slight distortions of the corresponding tetrahedra. The charge for two of these sulfur anions, S(3) and S(4) is under compensated by 12.5%. These anions are coordinated to three copper cations and one silicon cation, which produce a local cationic charge of +1.75, resulting in net charge of -0.25 per tetrahedron. The third type of sulfur environment, S(7), results in a 25% over compensation of charge, +0.50 per tetrahedron. This is a consequence of the sulfur anion being bound to two copper

Table 4.3: Extended connectivity table for $Cu_4CdSi_2S_7$ used for understanding the connectivity of the ions and calculating the vertical bond strength sum.

	4S(1)	4S(2)	4(S3)	4S(4)	4S(5)	4S(6)	4(S7)
4Cu(1)	4x1/4		4x1/4	4x1/4			4x1/4
4Cu(2)		4x1/4		4x1/4	4x1/4	4x1/4	
4Cu(3)		4x1/4	4x1/4	4x1/4			4x1/4
4Cu(4)	4x1/4		4x1/4		4x1/4	4x1/4	
4Cd(1)	4x1/2	4x1/2			4x1/2	4x1/2	
4Si(1)		4x1		4x1	4x1		4x1
4Si(2)	4x1		4x1			4x1	4x1
Vertical Bond Strength Sum Total	∑=8	∑=8	∑=7 (7<8)	∑=7 (7<8)	∑=8	∑=8	∑=10 (10>8)

and two silicon cations. An extended connectivity table providing the vertical bond strength sums helps to explicitly show the connectivity of the ions and explain the charge distribution in $Cu_4CdSi_2S_7$ as well as predict the distortions of the tetrahedra, Table 4.3. The vertical bond strength sum shown at the bottom of the table considers the multiplicity of the ions. It is expected that sulfur anions with environments in agreement with Pauling's second rule will have a vertical bond strength sum of eight for this compound since the multiplicity of all atoms is four. For example, there are four S(1) atoms in one unit cell, so we multiply four by either the absolute value of the

Table 4.4: Complete bond distance table for $Cu_4CdSi_2S_7$.

Metal-Sulfur Bond	Bond Distances (Å)	Metal-Sulfur Bond	Bond Distances (Å)
Cu(1)-S(1)	2.288(4)	Cd(1)-S(1)	2.529(3)
Cu(1)-S(3)	2.328(4)	Cd(1)-S(2)	2.510(4)
Cu(1)-S(4)	2.286(4)	Cd(1)-S(5)	2.525(3)
Cu(1)-S(7)	2.442(4)	Cd(1)-S(6)	2.498(3)
Cu(2)-S(2)	2.315(4)	Si(1)-S(2)	2.110(8)
Cu(2)-S(4)	2.303(4)	Si(1)-S(4)	2.094(6)
Cu(2)-S(5)	2.349(4)	Si(1)-S(5)	2.126(7)
Cu(2)-S(6)	2.306(4)	Si(1)-S(7)	2.217(6)
Cu(3)-S(2)	2.341(4)	Si(2)-S(1)	2.124(6)
Cu(3)-S(3)	2.297(4)	Si(2)-S(3)	2.113(6)
Cu(3)-S(4)	2.308(4)	Si(2)-S(6)	2.122(7)
Cu(3)-S(7)	2.413(5)	Si(2)-S(7)	2.216(6)
Cu(4)-S(1)	2.345(3)		
Cu(4)-S(3)	2.290(4)		
Cu(4)-S(5)	2.309(4)		
Cu(4)-S(6)	2.323(4)		

charge on sulfur or eight minus the number of valence electrons on sulfur, ($8\text{-}e_S$). If the total sum from the table is eight, the anion has its charge compensated by the cations in the first coordination sphere. S(1), S(2), S(5) and S(6) fall into this category. However, the vertical bond strength sums for S(3), S(4) and S(7) do not yield the expected eight because Pauling's second rule is broken. The under compensated sulfur anions, S(3) and S(4), both have bond strength sums of 7, while

S(7), which is over compensated, has a bond strength sum of 10. Locally the metal sulphide tetrahedra do not charge balance, but the local charges are balanced overall in the unit cell to form a valence precise compound.

The metal-sulfur bond distances are displayed in Table 4.4 to assist in the following comparison of bond distances. The undercompensated sulfurs are not undercompensated by much (12.5%); therefore, shortening of the M-S bonds is not observed. There are some M-S bonds with sulfur atoms obeying Pauling's second rule that are comparable to those of M-S(3) and M-S(4). However, for the overcompensated sulfur the mismatch in charge is more significant, a 25% difference, and that overcompensation is manifested in significantly longer M-S bonds. The M-S(7) bonds are the longest in the structure.

It is predicted that when anions are undercompensated for in terms of charge, they will pull the metal atoms closer resulting in a shortening of the M-S bonds. However, due to the undercompensation only being 12.5% no measurable effect is observed. For example, Cu(1) is connected to both of the undercompensated sulfurs, and therefore, it would be expected that these two Cu-S bond distances would be the shortest in the tetrahedron; yet, they are not. The Cu(1)-S(4) bond distance of 2.286(4) Å is the same as the Cu(1)-S(1) bond distance of 2.288(4) Å, where S(1) is an anion for which Pauling's second rule holds true. The Cu(1)-S(3) bond distance of 2.328(4) Å is surprisingly longer than the Cu(1)-S(1) bond. However, the overcompensated sulfur, S(7), is overcompensated by 25%. In this case, we would expect the bond distances to be lengthened and, indeed, there is a marked difference in the M-S(7) bond distances. Illustrating this, the Cu(1)-S(7) bond distance is the longest in the Cu(1) tetrahedron, 2.442(4) Å. Cu(3) is connected to three sulfur anions that are in environments of local charge neutrality in addition to

S(7). The Cu(3) bond distances to S(3), S(4) and S(2) are 2.297(4), 2.308(4) and 2.341(4) Å, while the Cu(3)-S(7) bond distance is notably longer, 2.413(5) Å.

It is interesting to note that cadmium is only connected to the sulfur anions that are locally charge balanced. Si(1) and Si(2) are connected to both under- and over-compensated sulfur anions. Just as was observed for Cu-S, the Si-S bond distances for the undercompensated sulfurs are not statically different from those found for the sulfur anions with local charge neutrality. Also, in agreement with what was observed for copper, the distances between silicon and S(7) are markedly longer. For example the Si-S(4), S(2) and S(5) distances are 2.094(6), 2.110(8) and 2.126(7) Å, respectively, while the Si(1)-S(7) bond distances is 2.217(6) Å.

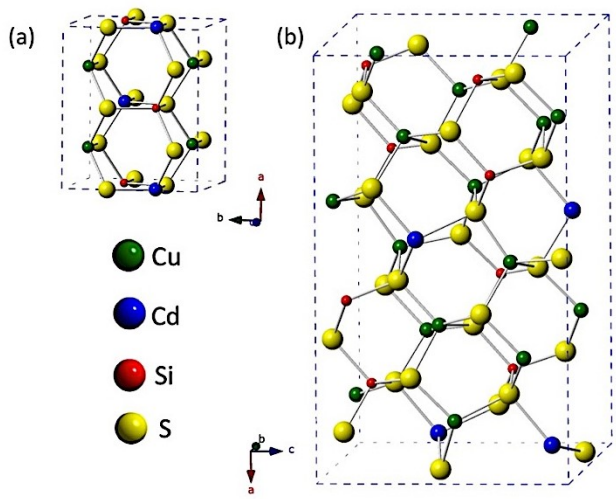

Figure 4.1: Comparison of the unit cells for (a) Cu_2CdSiS_4 and (b) $Cu_4CdSi_2S_7$ in which the copper, cadmium, silicon and sulfur atoms are respresnted in green, blue, red and yellow, respectively.

The related DLS Cu_2CdSiS_4 crystallizes with the wurtz-stannite structure type (*14*) in the orthorhombic, noncentrosymmetric space group P$mn2_1$ with six crystallographically unique atoms including one copper, one cadmium, one silicon and three sulfur atoms. (*53*) In this case, each sulfur anion is bound to two copper, one cadmium and one silicon cation. (*53*) This arrangement of cations and anions results in a locally charged-balanced environment for all sulfur anions. The tetrahedra in this structure are more regular. A comparison of the unit cells of $Cu_4CdSi_2S_7$ and Cu_2CdSiS_4 is displayed in Figure 4.1.

The local charge imbalances present in $Cu_4CdSi_2S_7$, which are not present in Cu_2CdSiS_4 cause subtle distortions of the MS_4 tetrahedra, Table 4.5. The difference in the average bond distances of the Cu-S and Cd-S bonds is the same within two standard deviations, although the Si-S bond distances differ by more than two standard deviations. The average S-M-S bond angles are the same for $Cu_4CdSi_2S_7$ and Cu_2CdSiS_4 within two standard deviations. The difference in the S-M-

Table 4.5: Average bond lengths, average angles and angle ranges found in Cu_2CdSiS_4 and $Cu_4CdSi_2S_7$.

	Cu_2CdSiS_4 (53)	$Cu_4CdSi_2S_7$
Space Group	P*mn*2_1	C*c*
Cu-S average bond distance	2.3(1) Å	2.328(1) Å
Cd-S average bond distance	2.544(9) Å	2.541(2) Å
Si-S average bond distance	2.119(6) Å	2.141(2) Å
S-Cu-S average bond angle	109.5(5)°	109.42(3)°
S-Cu-S bond angle range	108.84°-109.91°*	98.3(1)°-117.1(2)°
S-Cd-S average bond angle	109.5(5)°	109.48(4)°
S-Cd-S bond angle range	108.84°-109.91°*	105.1(1)°-114.2(1)°
S-Si-S average bond angle	109.5(5)°	109.5(1)°
S-Si-S bond angle range	108.84°-109.88°*	104.7(3)°-115.0(3)°

*Chapuis et al. did not report the errors for the bond lengths and angles determined from their crystal structure solution and refinement. (*53)*

angles is obvious when considering the ranges, which are greater for $Cu_4CdSi_2S_7$ than those of Cu_2CdSiS_4.

$Cu_4CdSi_2S_7$ and Cu_2CdSiS_4 also differ in their cation ordering. The larger unit cell and lower symmetry of $Cu_4CdSi_2S_7$ result in a more complex cation ordering pattern. When viewed down the b-axis of $Cu_4CdSi_2S_7$, the cation ordering presents rows of the same MS_4 tetrahedra. The MS_4 tetrahedra also make a pattern from left to right in the figure when viewed down the b-axis. The repeating pattern consists of seven MS_4 tetrahedra in the order: CuS_4, CdS_4, CuS_4, SiS_4, CuS_4, CuS_4, SiS_4. This pattern then repeats again after four rows. Cu_2CdSiS_4, viewed down the b-axis, also displays rows of the same type of MS_4 tetrahedra, although the repeating pattern is less complicated. The repeating pattern of MS_4 tetrahedra for Cu_2CdSiS_4, from left to right in Figure 4.2, consists of four MS_4 tetrahedra in the pattern; CuS_4, CdS_4, CuS_4, SiS_4.[53] This pattern repeats

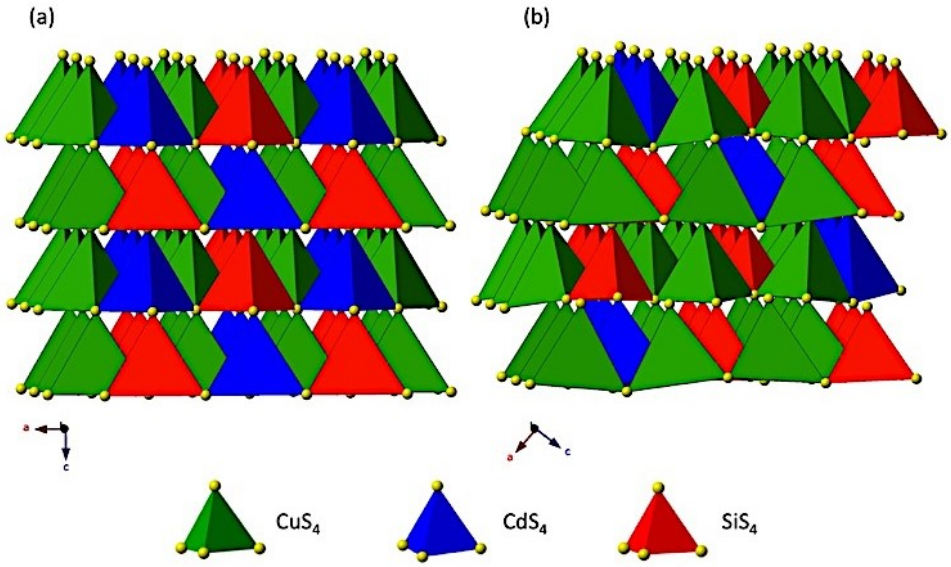

Figure 4.2: Cation ordering of (a) Cu_2CdSiS_4[53] and (b) $Cu_4CdSi_2S_7$ as viewed down the b-axis. The CuS_4, CdS_4 and SiS_4 tetrahedra are represented in green, blue and red, respectively.

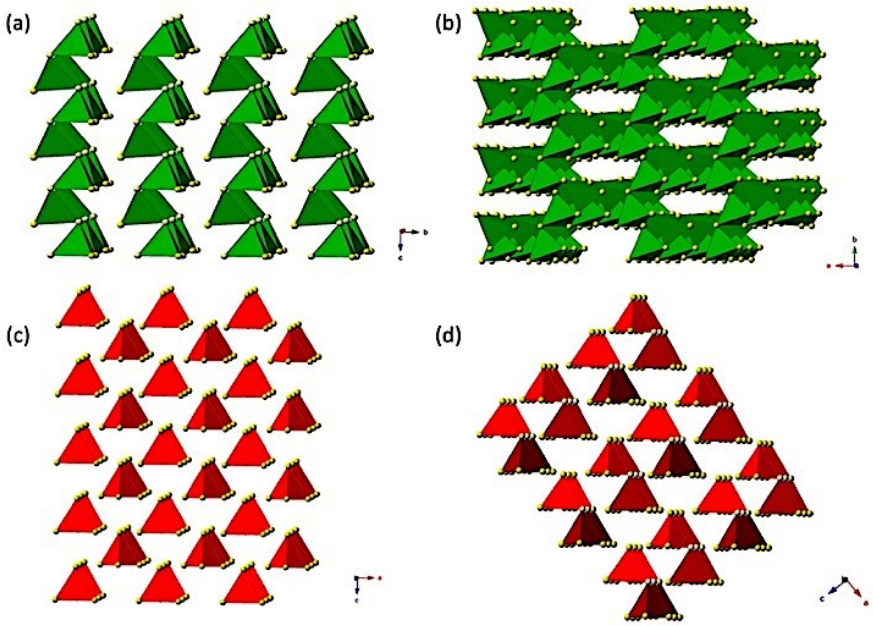

Figure 4.3: Tetrahedral connectivity of (a) CuS_4 and (c) SiS_4 for Cu_2CdSiS_4. (*53*) Tetrahedral connectivity of (b) Cu and (d) Si for $Cu_4CdSi_2S_7$. The crystallographically unique Si are indicated by two shades of red.

every third row. Figure 4.2 exemplifies the seven-by-four repeating pattern of MS_4 tetrahedra of $Cu_4CdSi_2S_7$ and the four-by-three repeating cation pattern of Cu_2CdSiS_4.

Closer inspection of the individual MS_4 tetrahedra shows further differences between $Cu_4CdSi_2S_7$ and Cu_2CdSiS_4. The CuS_4 tetrahedra of $Cu_4CdSi_2S_7$ connect with each other to produce a three-dimensional structure, while the CuS_4 tetrahedra of Cu_2CdSiS_4 (*53*) yield a two-dimensional structure, Figure 4.3. For $Cu_4CdSi_2S_7$, the SiS_4 tetrahedra alone result in corner sharing of two tetrahedra to form $[Si_2S_7]^{6-}$ units, Figure 4.3. The SiS_4 tetrahedra of Cu_2CdSiS_4 are not connected to one another. (*53*) The CdS_4 tetrahedra of both $Cu_4CdSi_2S_7$ and Cu_2CdSiS_4 (*53*) are also isolated from one another.

4. 3.2 Scanning Electron Microscopy (SEM) and Energy Dispersive Spectroscopy (EDS)

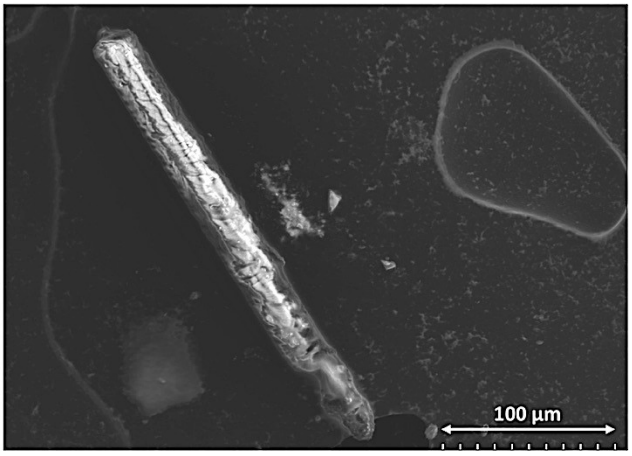

Figure 4.4: SEM micrograph of a needle-like crystal of $Cu_4CdSi_2S_7$.

Many attempts were made in an effort to obtain a phase-pure sample of $Cu_4CdSi_2S_7$. These attempts included altering the dwell temperature. dwell time, and cooling rate, including quenching the reactions. Adjusting the ratio of copper, cadmium, silicon and sulfur reactants was also attempted. Unfortunately, despite many different combinations of the above conditions, a phase-pure material was not produced; each of these changes resulted in a sample consisting of three or more phases. The fewest phases were obtained when a stoichiometric ratio of starting materials were used, the maximum temperature was 1100°C, a dwell time of 96 hours was used, and the reaction was cooled at a rate of 7.5°C/hour. This reaction resulted in three phases that were identified as Cu_2CdSiS_4, $Cu_4CdSi_2S_7$ and CdS using X-ray powder diffraction data. The analysis of the reaction products indicated that the major phase was Cu_2CdSiS_4 rather than $Cu_4CdSi_2S_7$, thus suggesting that Cu_2CdSiS_4 may be more stable. Single crystals were collected from the reaction products on which scanning electron microscopy (SEM) coupled with energy dispersive spectroscopy (EDS) were performed to semi-quantitatively assess the elemental ratio in the crystals. Figure 4.4 displays an SEM micrograph of the needle-like crystal on which the data were collected. The EDS data indicated a ratio of $Cu_{4.76(2)}Cd_{1.000(4)}Si_{1.78(1)}S_{6.89(3),}$ when the data are normalized to one equivalent of Cd.

4.3.3 Electronic Structure Calculations

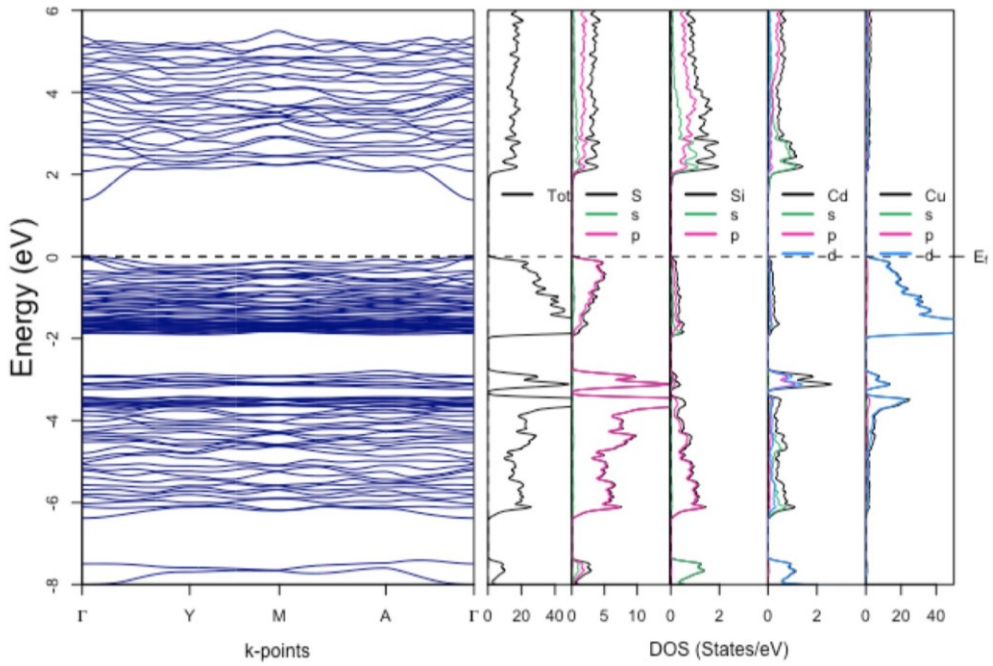

Figure 4.5: Electronic structure, density of states and partial density of states for $Cu_4CdSi_2S_7$. The *s*, *p* and *d* orbitals are displayed in green, red and blue respectively.

The calculated electronic band structure, total density of states (DOS) and partial density of states (PDOS) for $Cu_4CdSi_2S_7$ are displayed in Figure 4.5. The valence band maximum (VBMa) and the conduction band minimum (CBMi) are both located at the **Γ**-point within the Brillouin zone indicating that $Cu_4CdSi_2S_7$ is a direct bandgap material, as shown on the left-hand side of Figure 4.5. The value of the bandgap was calculated as 1.5 eV.

Careful examination of the PDOS has led to a better understanding of the origin of the bandgap. The bulk of the VBMa from 0 to -2 eV is a result of the copper *d* orbitals, with additional contributions from the sulfur *p* orbitals. The effect of the sulfur *p* orbitals becomes more prevalent deeper into the valence band from -3 to -6 eV. Lesser involvement in this area is a product of the copper *d*, silicon *p* and cadmium *d* orbtials. The CBMi is also dominated by the sulfur *p* orbitals

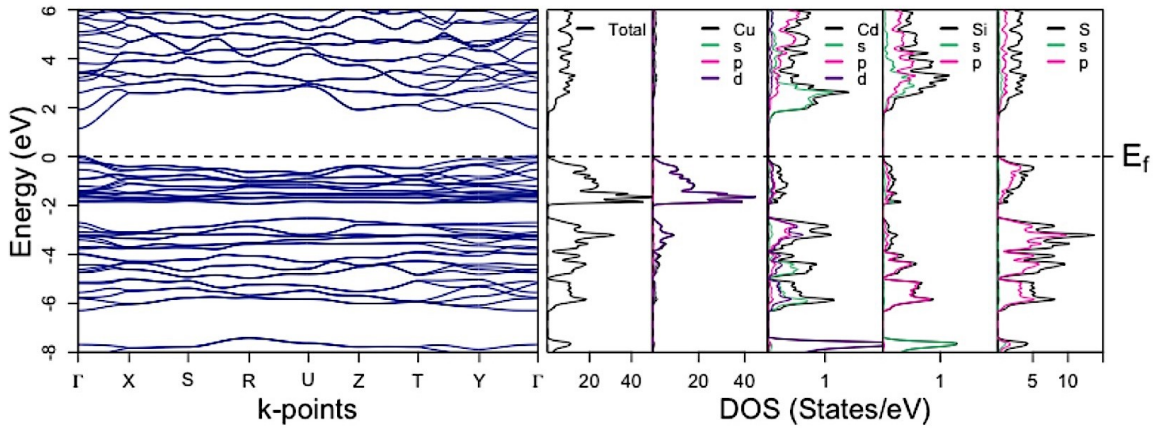

Figure 4.6: Electronic structure, total density of states and partial density of states for Cu_2CdSiS_4. The *s*, *p* and *d* orbitals are displayed in green, red and purple, respectively.

starting at 2 eV and continues into the conduction band past 6 eV. The silicon *s* and cadmium *s* orbitals also affect the CBMi, but to a smaller extent.

The band structure and DOS of Cu_2CdSiS_4 were also calculated, Figure 4.6. Similarly, to $Cu_4CdSi_2S_7$, Cu_2CdSiS_4 is calculated to have a direct bandgap at the **Γ**-point, although narrower at 1.13 eV. The orbital contributions, as exemplified by the PDOS for Cu_2CdSiS_4, are exceptionally similar to those of $Cu_4CdSi_2S_7$. The major impact to the VBMa in both cases is a result of the coper *d* and sulfur *p* orbitals, while the CBMi is dominated by the sulfur *p* orbitals in both cases. The differences between the PDOS come from the magnitude of the orbital impact, the DOS/eV contribution of the orbitals from $Cu_4CdSi_2S_7$ is greater than that of Cu_2CdSiS_4.

The major difference between $Cu_4CdSi_2S_7$ and Cu_2CdSiS_4 is a result of the different nearest neighbours in the coordination spheres of S(3), S(4) and S(7); therefore, the PDOS for each of the crystallographically unique sulfurs atoms was examined, Figure 4.7. Under meticulous scrutiny, minor differences in the PDOS arise from the sulfur anions are observed. These differences are most pronounced in the valence band from approximately -2 to -5 eV, while there is no notable difference in the conduction band.

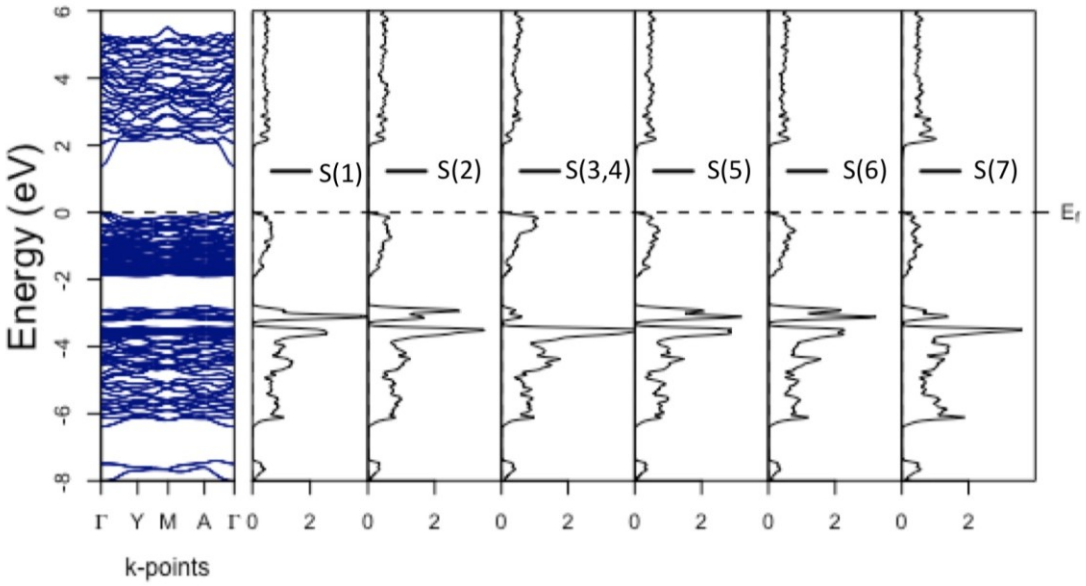

Figure 4.7: Density of states arise from the crystallographically unique sulfur atoms in $Cu_4CdSi_2S_7$.

Similar orbital contributions observed around the fermi levels of $Cu_4CdSi_2S_7$ and Cu_2CdSiS_4 are also seen among ternary copper-containing DLSs of the general formula Cu-III-VI_2. Six such DLSs include $CuAlS_2$, $CuGaS_2$, $CuInS_2$, $CuAlSe_2$, $CuGaSe_2$, $CuInSe_2$ which have been calculated to be direct bandgap semiconductors. (*66*) In each case, the VBMa is dominated by the copper *d* states and the sulfur *p* states. The largest contribution to the VBMa is from the copper *d* states in each case; between these six compounds the degree of the *d* orbitals involvement differs very little. The *s* states provide the largest contribution to the CBMi. This suggests that the monovalent and tetravalent ions have the largest impact on the VBMa and CBMi, and that the other elements could be changed with little effect on the electronic structure of the material.

4.4 Conclusions

$Cu_4CdSi_2S_7$ is a new DLS that crystalizes in the Cc space group and has been investigated to understand how changes in stoichiometry alter the structure of a quaternary DLS and its properties. The major structural differences between $Cu_4CdSi_2S_7$ and

Cu_2CdSiS_4 are due to the breaking of Pauling's second rule by $Cu_4CdSi_2S_7$. It is surprising that although $Cu_4CdSi_2S_7$ violates Pauling's second rule, the resulting distortions are very small. It is interesting, that despite the drop in symmetry from $Cu_4CdSi_2S_7$ to Cu_2CdSiS_4 and the breaking of Pauling's second rule, that the electronic structures are very similar. Further investigation of the differences between these materials was hindered by the inability to synthesize a phase-pure sample of $Cu_4CdSi_2S_7$. Other I_4-II-IV_2-VI_7 compounds have been discovered and it is possible that many more may exist, but have not been targeted.

4.5 References

(1) Goryunova, N.A., *The Chemistry of Diamond-like Semiconductors,* The MIT Press, Cambridge MA, **1964**.

(2) Parthé, E., *Crystal Chemistry of Tetrahedral Structures*, Gordon and Breach Science Publishing, New York, NY, **1964**.

(3) Brunetta, C.D.; Minsterman, C.W. III; Lake, C.H.; Aitken, J.A., *J. Solid State Chem.*, **2012**, *187*, 177-185.

(4) Pauling, L., *J. Am. Chem. Soc.*, **1929**, *51*, 1010-1026.

(5) Kaib, T.; Haddadpour, S.; Andersen, H.F.; Mayfofer, L.; Järvi, T.T.; Moseler, M.; Möller, K.-C.; Dehnen, S. *Adv. Funct. Mater.*, **2013**, *23*, 5693-5699.

(6) Wu, K.; Yang, Z.; Pan, S., *Chem. Commun.*, **2017**, *53*, 3010-3013.

(7) Gulay, L.D.; Olekseyuk, I.D.; Parasyuk, O.V., *J Alloys Compd*, **2002**, *340*, 157-166.

(8) Schäfer, W.; Scheunemann, K.; Nitsche, R., *Mat. Res. Bull.*, **1980**, *15*, 933-937.

(9) Brant, J.A.; Clark, D.J.; Kim, Y.S.; Jang, J.I.; Weiland, A.; Aitken, J.A., *Inorg. Chem.,* **2015***, 54, 2809-2819.*

(10) Devlin, K.P.: Glaid, J.A.: Brant, J.A.; Zhang, J.-H.; Srnec, M.N.; Clark, D.J.; Kim, Y.S.; Jang, J.I.; Daley, K.R.; Moreau, M.A.; Madura, J.D.; Aitken, J.A., *J. Solid State Chem.*, **2015**, *231*, 256-266.

(11) Wu, K.; Pan, S., *Crystals*, **2017**, *7*, 107.

(12) Parasyuk, O.V.; Gulay, L.D.: Piskach, L.V.; Gagalovska, O.P., *J. Alloys Compd.*, **2002**, *336*, 213-217.

(13) Haeuseler, H.; Himmrich, M., *Z. Naturforsch*, **1989**, *44b*, 1035-1036.

(14) Parthé, E.; Yvon, K.; Deitch, R.H. *Acta Cryst.*, **1969**, *B25*, 1164-1174.

(15) Todd, M.W.; Provencal, R.A.; Owano, T.G.; Paldus, B.A.; Kachanov, A.; Vodopyanov, K.L.; Hunter, M.; Coy, S.L.; Steinfeld, J.I.; Arnold, J.T., *Appl. Phys. B,* **2002**, *75*, 367-376.

(16) Williams, O.M., *Infrared Phys. Technol.*, **1998**, *39*, 473-486.

(17) Zuclich, J.A.; Lund, D.J.; Stuck, B.E., *Health Physics*, **2007**, *92*, 15-23.

(18) Knuteson, D.J.; Singh, N.B.; Kanner, G.; Berghmans, A.; Wagner, B.; Kahler, D.; McLaughlin, S.; Suhre, D.; Gottlieb, M., *J Cryst Growth*, **2010**, *312*, 1114-1117.

(19) Richardson, M.A.; Coath, J.A., *Opt Laser Technol,* **1998***, 30, 137-140.*

(20) Lu, W.; Liu, L.; Sun, J.; Pan, W., *Optik*, **2008**, *119*, 388-394.

(21) Chatterjee, U., *Pramana-J. Phys.*, **2014**, *82*, 29-38.

(22) Hopkins, F.K., *Opt. Photonics News*, **1998**, *9*, 32-38.

(23) Stoeppler, G.; Schellhorn, M.; Eichhorn, M., *Laser Phys.*, **2012**, *22*, 1095-1098.

(24) Tura, A.; Maran, A.; Pacini, G., *Diabetes Res. Clin. Pract.*, **2007**, *77*, 16-40.

(25) Amaral, C.E.F.; Wolf, B., *Med. Eng. & Phys.*, **2008**, *30*, 541-549.

(26) Haidar, S.; Miyamoto, K.; Ito, H., *Opt. Commun.*, **2004**, *241*, 173-178.

(27) Vaicikauskas, V.; Kaucikas, M.; Svedas, V., *Rev. Sci. Instrum.*, **2007**, *78*, 023106.

(28) Rockett, A.A., *Curr. Opin. Solid State Mater. Sci.*, **2010**, *14*, 143-148.

(29) Stanbery, B.J., *Crit. Rev Solid State Mater. Sci.*, **2010**, *27*, 73-117.

(30) Fella, C.M.; Romanyuk, Y.E.; Tirwari, A.N., *Sol. Energ. Mat. Sol.*, **2013**, *119*, 276-277.

(31) Shin, B.; Gunawan, O.; Zhu, Y.; Bojarczuk, N.A.; Chey, S.J.; Guha, S., *Prog. Photovoltaics*, **2013**, *21*, 72-76.

(32) Wagner, S.; Bridenbaugh, P.M., *J. Cryst. Growth*, **1977**, *39*, 151-159.

(33) Ponce, F.A.; Bour, D.P., *Nature*, **1997**, *386*, 351-359.

(34) Gessmann, T.; Schubert, E.F., *J App. Phys.*, **2004**, *95*, 2203-2216.

(35) Dupuis, R.D., *J. Lightwave Technol.*, **2008**, *26*, 1154-1171.

(36) Chang, H.-M.; Das, D.; Varde, P.V.; Pecht, M., *Microelectron. Reliab.*, **2012**, *52*, 762-782.

(37) Yao, J; Takas, N.J.; Schliefert, M.L.; Paprocki, D.S.; Clanchard, E.R.; Gou, H.; Mar, A.; Exstrom, C.L.; Darveau, S.A.; Poudeu, P.F.P.; Aitken, J.A., *Phys, Rev. B.*, **2011**, *B*, 84.

(38) Ortiz, B.R.; Peng, W.; Gomes, L.; Gorai, P.; Zhu, T.; Smiadak, D.M.; Snyder, G.J.; Stevanović, V.; Ertekin, E.; Zevalkink, A.; Toberer, E.S., *Chem. Mater*, **2018**, *30*, 3395-3409.

(39) Cho, J.Y.; Shi, X.; Salvador, J.R.; Yang, J.; Wang, H., *J. Appl. Phys.*, **2010**, *108*, 073713.

(40) Qui, P.; Qin, Y.; Zhang, Q.; Li, R.; Yang, J.; Song, Q.; Tang, Y.; Bai, S.; Shi, X.; Chen, L., *Adv. Sci.*, **2018**, *5*, 1700727.

(41) Cheng, Y.; Peng, B.; Hu, Z.; Zhou, Z.; Lui, M., *Phys, Lett. A*, **2018**, *382*, 3018-3025.

(42) V.K. Joshi, *Eng. Sci, Technol. Int. J.*, **2016**, *19*, 1503-1513.

(43) Leung, C.M.; Li, J.; Viehland, D.; Zhuang, X., *J. Phys, D: Appl. Phys.*, **2018**, *51*, 263002.

(44) Lu, J.W.; Chen, E.; Kabir, M.; Stan, M.R.; Wolf, S.A., *Int. Mater. Rev.*, **2016**, *61*, 456-472.

(45) Žutic, I.; Fabian, J.; Sarma, S.D., *Rev. Mod. Phys.*, **2004**, *76*, 323-410.

(46) Takada, K., *Acta Materialia*, **2013**, *61*, 759-770.

(47) Brant, J.A.; Devlin, K.P.; Bischoff, C.; Watson, D.; Martin, S.W.; Gross, M.D.; Aitken, J.A., *Solid State Ionics*, **2015**, *278*, 268-274.

(48) Brant, J.A.; Massi, D.M.; Holzwarth, N.A.W.; MacNeil, J.H.; Douvalis, A.P.; Bakas, T.; Martin,S.W.; Gross, M.D.; Aitken, J.A., *Chem. Mater.*, **2015**, *27*, 189-106.

(49) West, A.R., *Solid State Chemistry and its Applications*, John Wiley & Sons Ltd., London, UK, **2004**.

(50) Evans, H.T.; McKnight, E.T., *Am. Mineral.*, **1959**, *44*, 1210-1218.

(51) Adiwidjaja, G.; Loehm, J., *Acta Cryst. B*, **1970**, *26*, 1878-1879.

(52) Eckerlin, V.P., *Zeitschrift für anorganische und allgemeine Chemic*, **1967**, *353*, 225-235.

(53) Chapuis, G.; Niggli, A., *Acta, Cryst. B*, **1972**, *28*, 1626-1628.

(54) Rosmus, K.A.; Brunetta, C.D.; Srnec, M.N.; Karuppannan, B; Aitken, J.A., *Z. Anor. Allg. Chem.*, **2012**, *15*, 2578-2584.

(55) Pamplin, B., *Prog. Cryst. Growth Charact.*, **1981**, *3*, 179-192.

(56) SAINT is part of the Apex2 software package v2.1-4 Program for Data Collection and Reduction on Bruker AXS CCD Area Detector Systems. *Apex2 software package v2.1-4*; Bruker Analytical X-ray Systems, Inc., Madison, WI, **2005**.

(57) SHELXTL, release 6.14; Bruker AXS; Madison, WI, **2005**.

(58) CrystalMaker, version 9, CrystalMaker Software Limited, Oxfordshire, UK.

(59) X.p.H. Plus, PANalytical. B.V., Almelo, the Netherlands.

(60) Faber J.; Fawcett, T., Acta Crystallogr., Sect. B: Struct. Sci., **2002**, 58, 325–332

(61) Blaha, P.; Schwarz, K.; Madsen, G.K.H.; Kvasnicka, D.; Luitz, J., Vienna University of Technology, Austria, **2011**.

(62) Perdew, J.P.; Burke, S.; Ernzehof, M., *Phys. Rev. Lett.*, **1996**, 77, 3865-3868.

(63) Dogguy, P.M.; Jaulmes, S.; Laruelle, P.; Rivet, J., *Acta Cryst,* **1982**, *B38m*, 2014-2016.

(64) Dogguy, M., *Materials Chemistry and Physics*, **1983**, *9*, 405-412.

(65) Gulay, L.D.; Olekseyuk, I.D.; Parasyuk, O.V., *J. Alloys Compd.*, **2002**, *340*, 157-166.

(66) Jaffe, J.E.; Zunger, A., *Phys. Rev.* B, **1983**, *28*, 5822-5847.

Chapter 5: Li_2ZnSiS_4 a Diamond-like Material

5.1. Introduction

The area of nonlinear optics (NLO) is one that has attracted a lot of attention in recent years and spans multiple disciplines. A major focus of NLO research is the creation of frequency conversion crystals for use in the infrared (IR). For example, second harmonic generation (SHG) materials produce radiation with a wavelength half that of the incident laser, i.e. double the frequency. There is an intense interest in this area due to the applications in which these materials are used. Military and medical applications account for a large portion of this research. NLO crystals are a critical component of devices that are used for the detection of explosives, signal jamming of missiles, retinal scanning for identification and potentially illicit drug detection. (*1-7*) In the medical field, NLO materials can be used in laser surgery, and noninvasive disease detection/monitoring. (*8-12*) Yet, the development of new and improved applications is hindered by the limitations of the current commercially available IR-NLO crystals. One critical limitation is the laser-induced damage threshold (LIDT) of the materials, which is a measure of the laser intensity that a crystal can withstand before incurring optical damage. While many research groups focus on the second-order nonlinear optical susceptibility of NLO materials, the LIDT of a material is of paramount importance for commercial viability due to the great need for crystals that can operate with high powered lasers, P_{ave}> 1 kW. (*13*)

To this end, many new noncentrosymmetric (NCS) materials have been discovered with measureable SHG responses and significant LIDTs including sulfides, (*14-22*) selenides, (*22-26*) halides, (*27-30,32*) oxides (*28-33*) and iodides (*32-34*) some of which are listed in Table 5.1.

Table 5.1: Selected details concerning some compounds for which laser induced damage threshold (LIDT) has been recently assessed.

Compound	Bandgap (eV)	LIDT ($GW \cdot cm^{-2}$)	Wavelength (nm)	Pulse width	Reference
$Li_2Ga_2GeS_6$	~3.65	Not Provided	1064	Not Provided	*14*
$SnGa_4S_7$	3.10	0.1651	1064	8 ns	*15*
$Na_2Hg_3Si_2S_8$	2.86	0.054	1060	10 ns	*16*
$Na_2Hg_3Ge_2S_8$	2.68	0.036	1060	10 ns	*16*
$Na_2Hg_3Sn_2S_8$	2.45	0.125	1060	10 ns	*16*
$Ba_6Zn_7Ga_2S_{16}$	3.50	0.04047	1064	10 ns	*17*
$Na_2ZnGe_2S_6$	3.25	0.228	1064	10 ns	*18*
Li_2CdGeS_4	3.15	>4	1064	30 ps	*19*
Cu_2CdSnS_4	0.92	0.2	1064	30 ps	*20*
α-Cu_2ZnSiS_4	~3.0	2	1064	30 ps	*20*
β-Cu_2ZnSiS_4	~3.2	2	1064	30 ps	*20*
Li_2MnGeS_4	3.069(3)	>16	1064	30 ps	*21*
$Na_2In_4SSe_6$	1.92	0.0069	1064	10 ns	*22*
$PbGa_2SiSe_6$	2.17	Not Provided	1064	8 ns	*23*
$PbGa_2GeSe_6$	1.96	0.00561	1064	8 ns	*23*
$SnGa_4Se_7$	2.55	0.04	1064	8 ns	*15*
$NaGaIn_2Se_5$	2.00	0.0077	1064	10 ns	*22*
$NaIn_3Se_5$	2.17	0.0128	1064	10 ns	*22*
$RbGaSn_2Se_6$	1.80	0.01282	1064	8 ns	*24*
$RbInSn_2Se_6$	1.92	0.01160	1064	8 ns	*24*
$Na_4MgSi_2Se_6$	2.85	0.0458	1060	10 ns	*25*
$Na_4MgGe_2Se_6$	2.53	0.0358	1060	10 ns	*25*
$Li_2ZnGeSe_4$	1.8628(4)	~0.3	1064	30 ps	*26*
$Li_2ZnSnSe_4$	1.868(1)	~0.3	1064	30 ps	*26*
$CsHgBr_3$	3.0	0.226	1064	5 ns	*27*
$Pb_{17}O_8Cl_{18}$	3.44	0.408	1064	10 ns	*28*
$RbIO_2F_2$	4.2	0.156	1064	5 ns	*32*
$LiNa_5Mo_9O_{30}$	not given	1.2	1064	6 ns	*29*
Li_3VO_4	4.27	0.12550	1064	10 ns	*30*
$LiO_3Te(OH)_6$	Not given	0.731	1064	6 ns	*31*
$RbIO_3$	4.0	0.125	1064	5 ns	*32*
$K_2BiI_5O_{15}$	3.50	0.084	1064	5 ns	*33*
$Rb_2BiI_5O_{15}$	3.53	0.072	1064	5 ns	*33*
$Rb_2CdBr_2I_2$	3.35	0.19	1064	5 ns	*34*

The most common way to target a new candidate SHG material is to aim for the formation of acentric building blocks that may assemble into a noncentrosymmetric structure. This is important, as the lack of an inversion center is the primary requirement of all SHG materials. (*35*) Second-order Jahn-Teller distortions, (*35-40*) stereochemically active lone pairs (*35,41-46*) and borate $[BO_3]^{3-}$ units (*35*) are a few avenues that are pursued to achieve a noncentrosymmetric assembly of asymmetric building blocks. However, the formation of asymmetric building blocks does not guarantee packing into an overall structure that is NCS. Pursuing diamond-like materials (DLMs) is one way to ensure that a noncentrosymmetric material is created, since all DLMs are inherently NCS. All diamond-like structures are derived from either cubic or hexagonal diamond, which feature tetrahedral units aligned along one crystallographic direction. (*47, 48*) When designing a new DLM, four guidelines must be adhered to. Firstly, all the atoms must be tetrahedrally coordinated. (*47,48*) In choosing elements to use, the average number of valence electrons must equal four and the average number of valence electrons per anion must equal eight. (*47-49*) It is also ideal that the material follows Pauling's second rule, which states that the charge of an anion is compensated by the valence bonds of the cations within the first coordination sphere. (*50*) The success of this strategy is exemplified by the fact that all commercially available infrared NLO materials are DLMs, including $AgGaS_2$, $AgGaSe_2$, $ZnGeP_2$, $LiInS_2$ and $LiInSe_2$. (*51-53*)

In selecting elements to prepare new candidate IR-NLO materials with diamond-like structures it is important to consider the effect that each element will have on the material's properties. The general relationship between a material's bandgap, LIDT and SHG response is one point of focus for property optimization. Increasing the bandgap of a material is known to generally increase the LIDT; however, the relationship between SHG response and bandgap is inverse, where by increased bandgaps usually result in a smaller second-order nonlinear optical

susceptibility. (*54*) When considering I-III-VI_2 and I_2-II-IV-VI_4 DLMs, the choice of the monovalent cation is one way to manipulate the bandgap. The monovalent cations most commonly used for the creation of these DLMs are lithium, silver and copper. (*35*) Of these monovalent cations, lithium-containing compounds have shown larger bandgaps and correspondingly large LIDTs, such as $LiInSe_2$ that has a bandgap reported between 2.2-2.8 eV and a LIDT of 1.0 GW·cm^{-2}. (*35,55*)

Recently the wide bandgap (~3.0-3.2 eV) Cu_2ZnSiS_4, was found to exhibit a LIDT of 2 GW·cm^{-2} ($\lambda = 1064$ nm and $\tau = 30$ ps), over an order of magnitude larger than those of the commercially available $AgGaS_2$ and $AgGaSe_2$, which have narrower bandgaps of 2.76 eV, and 1.83 eV, respectively. (*20,56*) Therefore we chose to use lithium instead of copper to make the compound Li_2ZnSiS_4, which would be expected to have a wider bandgap and increased LIDT. However, before we could synthesize a phase-pure microcrystalline powder for property measurements, Zhou et al. obtained the SHG, LIDT and related measurements from millimeter-sized single crystals. (*57*) This chapter presents the crystal structure and characterization of Li_2ZnSiS_4 from a nearly phase-pure powder as compared to the results of Zhou et al.

5.2. Experimental

5.2.1 Synthesis

5.2.1.1 Synthesis of Single Crystals

Single crystals of Li_2ZnSiS_4 were prepared via high-temperature solid-state synthesis. The reactions were prepared by weighting Li_2S (1.2 mmol, 98%, 99.9% Li, Strem), Zn (1 mmol, 99.999%, Strem), Si lump (1 mmol, ground using a diamonite mortar and pestle, 99.999+%, Alfa

Aesar) and S (3 mmol, sublimed powder, 99.5%, Fisher Scientific), and grinding the reagent mixture for 10 minutes in an agate mortar and pestle. The ground starting materials were placed in a carbon-coated 9 mm o.d. fused-silica tube, which was then sealed in a 12 mm o.d. fused-silica tube under vacuum of 10^{-4} mbar. The reaction vessel was heated to 1000 °C in 12 hours, held at 1000 °C for 96 hours after which it was cooled to room temperature at a rate of 7.5 °C/hour. The resulting product was washed with degassed methanol, under N_2 gas to remove excess Li_2S. The reaction products were identified as Li_2ZnSiS_4, and ZnS (sphalerite type) by X-ray powder diffraction. Light peach prisms were identified as Li_2ZnSiS_4 and single crystals were selected under a light microscope.

5.2.1.2 Synthesis of Nearly Phase-Pure Material

Li_2ZnSiS_4 was prepared as a nearly phase-pure material via high-temperature, solid-state synthesis. The material was prepared by weighing out Li_2S (2 mmol, 98%, 99.9% Li, Strem), Zn (0.8 mmol, 99.999%, Strem), Si lump (1.7 mmol, ground using a diamonite mortar and pestle, 99.999+%, Alfa Aesar) and S (5 mmol, sublimed powder, 99.5%, Fisher Scientific), combining the reactants in an agate mortar and pestle, and then grinding for 10 minutes. The ground starting materials were housed in a 9 mm o.d. carbon-coated fused-silica tube that was produced by pyrolizing acetone. The carbon-coated tube was sealed under vacuum of 10^{-4} mbar in a 12 mm o.d. fused-silica tube. The reaction vessel was heated to 600 °C in 12 hours, dwelled at 600 °C for 96 hours, then cooled to room temperature at a rate of 7.5 °C/hour. The products were washed with degassed methanol under a N_2 environment to remove excess Li_2S and other air sensitive ternary phases that were assumed to be present due to the input millimolar ratio.

5.2.2 Single-Crystal X-ray Diffraction

The single crystal X-ray analysis was accomplished using a Bruker SMART Apex 2 CCD single-crystal diffractometer, with graphite-monochromatized Mo-K_α radiation using a tube power of 50 kV and 30 mA. Data were collected from a light peach prism with dimensions of 0.23 x 0.14 x 0.11 mm. Table 5.2 includes the pertinent crystallographic data and experimental details. For the data collection, 20 second frames were collected over a range of 3.1-27.5° theta. A total of 1418 reflections were obtained with 1372 being unique ($R_{(int)}$=0.017). The maximum and minimum effective transmission factors were calculated to be 0.421 and 0.555, respectively. The data were integrated using the SAINT program and an analytical absorption correction was accomplished with SADABS. (*58*) The systematic absences identified using XPREP suggested two possible space groups, *Pna*2$_1$ and *Pnam*; the noncentrosymmetric space group *Pna*2$_1$ was selected because all DLMs possess NCS structures with aligned tetrahedral units. XPREP was also used for the file preparation for SHELXS to solve the structure. The SHELXTL software package was used for structure refinement. (*59*) Eight atoms were located on general positions. During the refinement process, both the Flack parameter and

Table 5.2: Selected crystallographic data, experimental details and refinement statistics for Li_2ZnSiS_4.

Chemical Formula	Li_2ZnSiS_4
Formula Weight (g mol^{-1})	235.58
Temperature (°C)	25
Wavelength (Å)	0.71073
Space Group	*Pna*2$_1$ (No. 33)
a (Å)	12.9228(7)
b (Å)	7.7944(4)
c (Å)	6.1613(3)
Volume (Å^3)	620.60(6)
Z	4
D_{calcd} (g cm^{-3})	2.521
μ (cm^{-1})	53.5
Flack	0.034(11)
R[I>2σ(I)], R(all data)	0.013, 0.0138
wR2[I>2σ(I)], wR2(all data)	0.028, 0.0277

$$wR2 = \left\{\frac{\Sigma[w(F_0^2 - F_c^2)^2]}{\Sigma[w(F_0^2)^2]}\right\}^{\frac{1}{2}}, \quad R1 = \Sigma\big||F_o| - |F_c|\big|/\Sigma|F_o|$$

the extinction coefficient were refined. The program CrystalMaker was used to generate all the crystal structure figures in this chapter. (*60*)

5.2.3 X-ray Powder Diffraction (XRPD)

X-ray powder diffraction data were collected using a PANalytical X'Pert Pro MPD X-ray powder diffractometer equipped with the X'cellerator Detector and employing Cu K_α radiation with a wavelength of 1.541871 Å. The tube power was 45 kV and 40 mA and data were collected over the range of 5° to 145° 2θ, with a step size of 0.0085556 and a scan rate of 0.010644 °/s. The incident beam path included a divergent slit fixed at ¼°, a 0.02 radian soller slit and a fixed anti-scatter slit of ½°. The diffracted beam path included a nickel filter, a 0.02 radian soller slit, and a fixed anti-scatter slit of ½°. The samples were prepared by grinding for 5 minutes and then top-filled into a zero-background holder. The crystalline phases present in the sample were identified using the search match capabilities of the X'Pert HighScore Plus (*61*) software coupled with the International Center for Diffraction Data (ICDD) powder diffraction file (PDF) database. (*62*)

5.2.4 Optical Diffuse Reflectance UV-vis-NIR Spectroscopy

A Varian Cary 5000 spectrometer, equipped with a Harrick Praying Mantis diffuse reflectance accessory, was used to collect the optical diffuse reflectance spectrum of Li_2ZnSiS_4 over the ultraviolet, visible and near infrared spectral regions (UV-vis-NIR), from 2500 nm to 200 nm. First, barium sulfate (Fisher, 99.92%) was used as a 100% reflectance standard. The ground sample was placed on top of the barium sulfate standard and scanned at a rate of 600 nm/min. The

raw data were collected as percent reflectance (%R) and converted to relative absorption (α_{KM}) as the scattering coefficient, s, is unknown using a Kubelka-Munk transformation. (*63*)

5.2.5 Differential Thermal Analysis (DTA)

The Shimatzu DTA-50 differential thermal analyzer, along with the TA60-WS data collection program was used to assess the thermal stability of the title material. For this method, a three-point calibration was performed with indium, zinc, and gold. Approximately 0.025 g of sample was vacuum sealed in a carbon-coated, fused-silica ampule to prevent reactions with the sample vessel. The sample was compared to a reference of Al_2O_3 of comparable mass and heated at a rate of 10 °C min^{-1} from 25 °C – 1100 °C, held at the maximum temperature for one minute and then cooled at the same rate, while under a constant flow of nitrogen.

5.2.6 Electronic Structure

Electronic structure calculations were performed for Li_2ZnSiS_4 using the computational program WIEN2K, (*64*) which employs density functional theory and the full-potential linearized augmented planewave method. The structure of the compound, in space group *Pna*2_1, obtained through single crystal X-ray diffraction at room temperature was used and no geometry or volume optimizations were performed for these calculations. The Perdew-Burke-Ernserhof generalized gradient approximation (PBE-GGA) (*65*) was implemented to treat the exchange and correlation effects. The calculations were carried out for 1000 k-points. The muffin tin radii (MTR) were reduced by three percent, resulting in RMT values of 2.01 bohr, 2.33 bohr, 1.84 bohr and 1.91 bohr

for lithium, zinc, silicon and sulfur, respectively. In addition to the electronic band structure, the total and partial density of states (DOS) were also calculated.

5.3. Results and Discussion

5.3.1 Crystal Structure

Li_2ZnSiS_4 is a diamond-like compound that crystallizes in the noncentrosymmetric space group $Pna2_1$ and adopts the lithium cobalt (II) silicate, Li_2CoSiO_4, structure type. (*66,67*) The unit cell is displayed in Figure 5.1 and the distinct honeycomb pattern common among diamond-like structures is observed when viewed down the crystallographic *c* axis. The crystal structure contains eight crystallographically unique atoms, two lithium, one zinc, one silicon, and four sulfur atoms. Each metal cation is tetrahedrally coordinated to four sulfur anions, and each sulfur anion is tetrahedrally coordinated to two lithium (both crystallographically unique), one zinc and one silicon cation. This connectivity creates a three-dimensional, corner-sharing tetrahedral structure, shared by all quaternary diamond-like structures of the formula I_2-II-IV-VI_4. (*47,48*) The bond distances and angles of all MS_4 tetrahedra are in good agreement with other such tetrahedral units in the literature. (*21,68,69*)

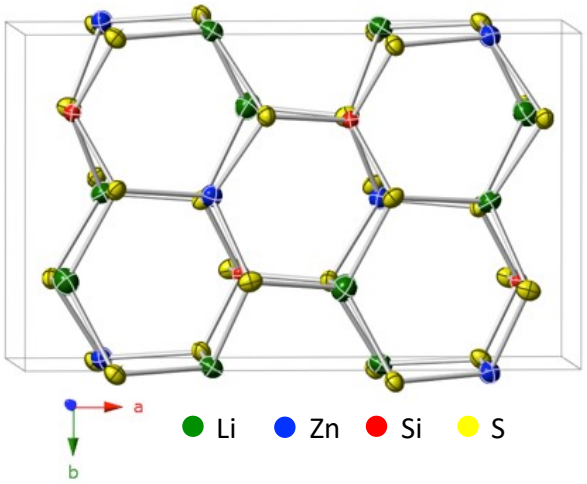

Figure 5.1: Oak Ridge thermal ellipsoid (ORTEPs) representation of the unit cell of Li_2ZnSiS_4 with 99% probability. The atoms indicated in green, blue, red and yellow represent lithium, zinc, silicon and sulfur atoms respectively.

The structure can be described as a closest packed array of sulfide ions where the cations occupy half of the tetrahedral holes. When viewed down the crystallographic *a* and *b* axis, as in Figure 5.2, it is easily observable that all the MS_4 tetrahedra point in the same direction, along the *c* axis. This alignment is responsible for the noncentrosymmetric structure expected for a diamond-like material. The difference between the structure types, i.e. space group, for DLMs lies in the cation ordering patterns. The ZnS_4 and SiS_4 tetrahedra are isolated from one another, while the $Li(1,2)S_4$ create a 3-dimentional network in which each LiS_4 tetrahedra connects to four others through corner sharing. One way to describe the cation ordering pattern is to view it down the crystallographic *a* axis, as in Figure 5.2a, and describe the rows of cations while moving along the *b* axis. It consists of a row of $Li(2)S_4$ and ZnS_4 (ABAB), a row of SiS_4 tetrahedra, then a second row of $Li(2)S_4$ and ZnS_4 that switch ordering (BABA) and next a row of $Li(1)S_4$ tetratedra. This pattern continues across the *b* axis and going along the *a* axis the pattern is shifted by two rows. Also displayed in Figure 5.2b, is a pattern of alternating rows of ZnS_4 and $Li(1)S_4$ tetrahedra (CDCD), and separated by alternating rows of SiS_4 and $Li(2)S_4$ (EFEF). This pattern is then alternated $Li(1)S_4$ and ZnS_4

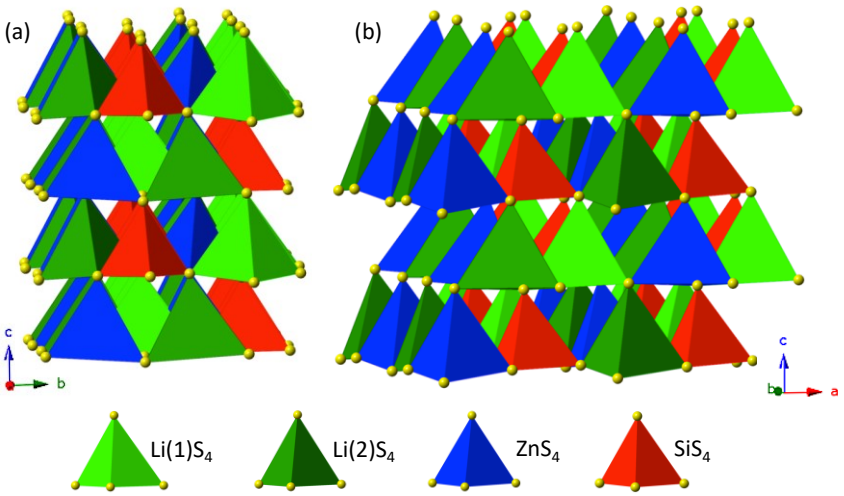

Figure 5.2: Cation ordering pattern for Li_2ZnSiS_4 view down the crystallographic (a) *a* axis and (b) *b* axis. The LiS_4, ZnS_4, SiS_4 tetrahedra are represented in green, blue and red respectively. The light green and dark green distinguish between the two crystallographically unique lithium atoms, Li(1) and Li(2), respectively.

(DCDC) and $Li(2)S_4$ and SiS_4 (FEFE), after which it repeats when viewed down the crystallographic *b* axis.

5.3.2 Synthesis Optimization of a Nearly Phase Pure Material

To obtain accurate measurements for the intrinsic properties of a material it is imperative that the measurements are collected on a phase-pure sample, devoid of secondary phases. Alternatively, Zhou et al hand-picked single crystals, which were then ground for analysis. This work utilized microcrystalline powders; however, phase-purity samples were not achieved. The heating profile and reaction conditions that resulted in the single crystals of Li_2ZnSiS_4 were the optimized reaction conditions reported for Cu_2ZnSiS_4. (*20*) While these conditions produced single crystals of Li_2ZnSiS_4 and were a logical starting point, it was clear from the severe reaction of Li_2S with the reaction vessel that these were not the optimal conditions. Li_2S is highly oxophilic and reacted with the fused-silica reaction vessel despite the secondary reaction vessel, as the high temperature increased the volatility of Li_2S. Systematic decreases of 100 °C in the maximum reaction temperature from 1000-600 °C were performed to determine an appropriate reaction temperature. It was observed that as the maximum temperature decreased, Li_2ZnSiS_4 became the dominant phase; at 600 °C the least amount of secondary phase was observed. These conditions with a direct stoichiometric ratio of reactants resulted in the presence of Li_2ZnSiS_4 and ZnS. It was then serendipitously discovered, while attempting to synthesize $Li_4ZnSi_2S_7$, that the direct stoichiometric ratio for targeting $Li_4ZnSi_2S_7$ preferentially produced Li_2ZnSiS_4. The XRPD pattern indicated Li_2ZnSiS_4 with additional small shoulder peaks present that did not match with ZnS. Based on the 4:1:2;7 ratio of reactants the phases that could be present due to excess reactants were

a combination of excess Li_2S and Li_2SiS_3. Removal of the suspected secondary phases was attempted through washing the products with a variety of solvents with differing polarities including acetone, ethanol, hexane, methanol, iso-propanol and water in which the products were sonicated. Varying the washing solvent, unfortunately, did not remove the secondary phase. At this point since the 4:1:2:7 ratio of reactants was not the optimal reaction condition the next step was to slightly vary this ratio. To do this, the input ratios of Li_2S, Zn Si, S, Li_2S and S, and Zn and Si were varied systematically by 0.1 mmol. The ratio of starting materials that produced the best results was a ratio of 2:0.8:1.7:5 of Li_2S:Zn:Si:S. These conditions produced a sample that gave rise to an XRPD pattern that did not contain any additional peaks and resulted in a UV-vis-NIR spectrum that was the closest to containing one absorption edge (which will be further discussed in section 3.3). Other alterations to the reactant ratios resulted in the observation of secondary phases (usually ZnS) in the XRPD patterns and/or a prominent second absorption edge in the UV-vis-NIR spectra. Variations in the reaction dwell time were also investigated. These reactions produced ZnS, in addition to Li_2ZnSiS_4, as evident by the XRPD analysis. The optimal conditions for producing a nearly phase-pure material are outlined in section 2.1.2, although this result has not been reproducible despite numerous efforts at reproduction. Attempts at reproduction formed products with prominent second absorption edges in the UV-vis-NIR spectra or ZnS present as a secondary phase in the XRPD pattern.

5.3.3 X-ray Powder Diffraction (XRPD)

Comparing the XRPD pattern for the collected data of Li_2ZnSiS_4 with a calculated XRPD pattern generated from the single crystal data (Figure 5.3) shows that all the peaks in the

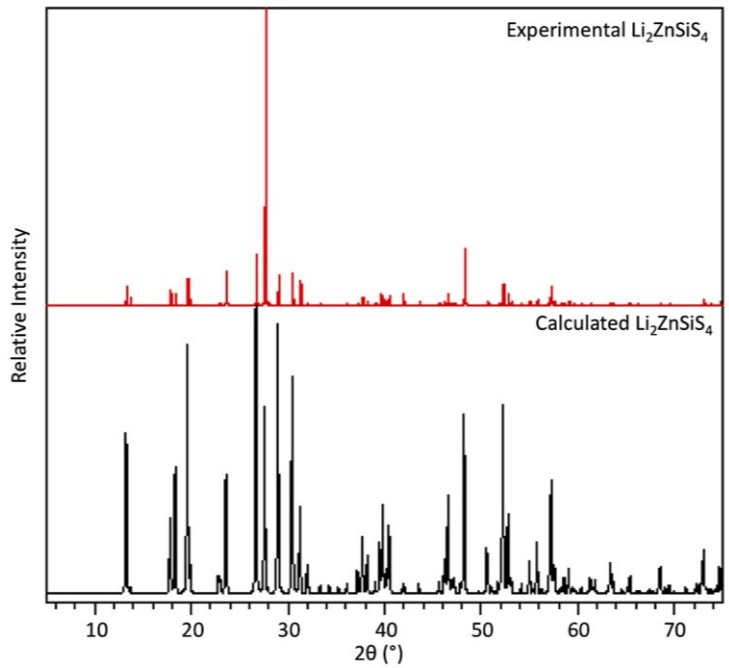

Figure 5.3: Li_2ZnSiS_4 XRPD pattern comparison of the experimentally collected and the calculated patterns, red and black respectively.

experimental pattern match with those of the calculated, with no residual peaks present. The lack of additional peaks indicates that secondary phases were not present within the detection limit of the instrumentation. It should be noted that the intensities of the peaks in the experimentally collected data do not match with those of the calculated pattern. This indicates that either preferential orientation was an issue during sample preparation or that an unidentified secondary phase was present whose peaks overlap with those of Li_2ZnSiS_4. This reaction product was reground and the sample prepared in several different ways in an effort to prevent preferred orientation, yet the discrepancy in peak intensity persisted. As the intensity of the peaks was not changed by sample preparation, it is more likely that a secondary phase is present. It is likely that the secondary phase is ZnS as this was the predominate secondary phase whenever the reaction conditions were altered. The amount of secondary phase present would also be relatively small as the major peaks overlap with those of Li_2ZnSiS_4 and the minor peaks that do not match with those for Li_2ZnSiS_4 are not present. The products of the reaction which resulted in the closest to phase purity were used for the analysis discussed in this chapter, and the reaction conditions are outlined in section 5.2.1.2.

5.3.4 Optical Diffuse Reflectance UV-vis-NIR Spectroscopy

The raw data from the optical diffuse reflectance UV-vis-NIR spectroscopy were collected as percent reflectance (%R) and converted to relative absorption (α_{KM}). A plot of the relative absorption versus photon energy in eV can be seen in Figure 5.4. To determine the optical bandgap the absorption edge was extrapolated to a baseline. The energy at which the extrapolation of the absorption edge and the baseline intersect is considered the bandgap of the material. The experimentally collected bandgap of Li_2ZnSiS_4 is approximately 4.2 eV. This bandgap is 0.3 eV larger than that reported by the Zhou group who reported an experimental bandgap of 3.9 eV. (*57*) In both cases, a second absorption edge was observed. In the work reported by the Zhou group the second absorption edge is likely due to the secondary phase that was observed in their XRPD pattern, although they did not address what this secondary phase was. In our work, this indicates that a secondary phase is present that could not be observed in the experimentally collected XRPD pattern. The secondary phase may be the reason for the difference in relative intensities between the experimentally collected and calculated XRPD. The second absorption edge is around 3.5 eV, which is close to the bandgap of ZnS. (*70-73*)

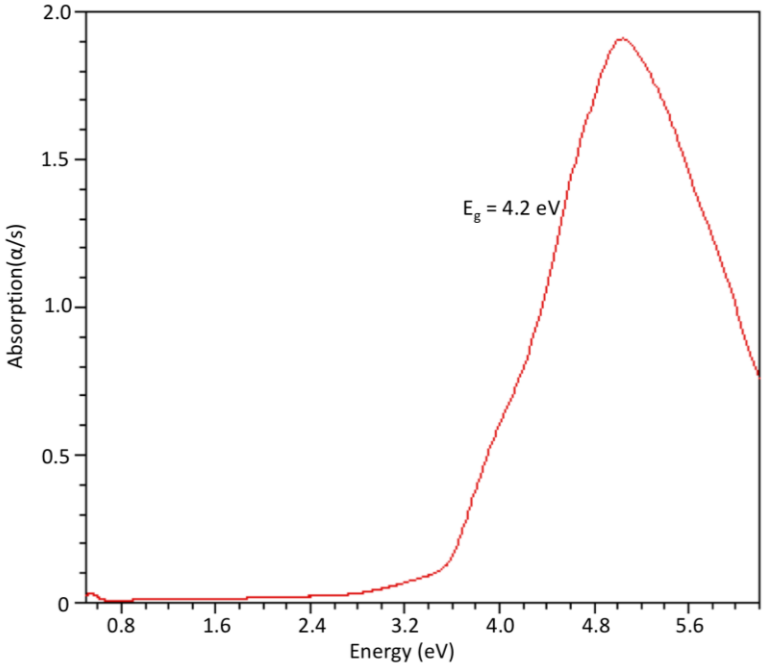

Figure 5.4: UV-vis-NIR spectrum illustrating the bandgap of Li_2ZnSiS_4.

Li_2ZnSiS_4 has a wider bandgap in comparison to the bandgap reported for the related compound Cu_2ZnSiS_4, between 3.0-3.2 eV. Li_2ZnSiS_4 also has a wider bandgap in comparison to the commercially available DLSs $AgGaS_2$ and $AgGaSe_2$, 2.75 eV and 1.8 eV respectively. (74,75) When compared to lithium-containing ternary DLS, Li_2ZnSiS_4 still has a wider bandgap in contrast to $LiGaS_2$, $LiGaSe_2$, $LiInS_2$, and $LiInSe_2$, which have bandgaps of 3.62 eV, 3.13 eV, 3.56 eV, 2.83 eV, respectively. (*76*) The bandgap of the title compound is also wider than almost all the NSC SHG materials listed in Table 5.1, so much so that Li_2ZnSiS_4 could almost be considered an insulator rather than a semiconducting material, as an insulator is generally considered to be a material with a bandgap >4.0 eV. (*77*)

5.3.5 Differential Thermal Analysis (DTA)

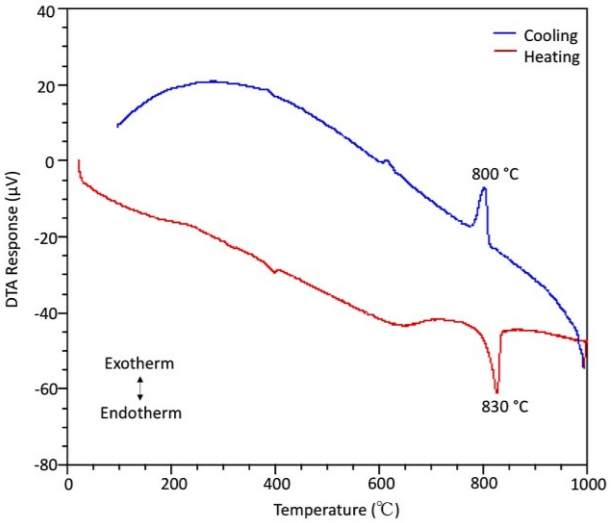

Figure 5.5: Differential thermal analysis diagram of Li_2ZnSiS_4.

Differential thermal analysis (DTA) of Li_2ZnSiS_4 allowed for the thermal behavior of the material to be studied. The collected data, as presented in Figure 5.5, contain an endothermic peak at 830 °C, which can be tentatively assigned to the melting point of Li_2ZnSiS_4 and the exothermic at 800 °C is likely the temperature of recrystallization. The crystallization temperature is higher than the maximum synthesis temperature of 600 °C, because the optimal synthesis conditions use an excess of Li_2S and S which create a Li_2S:S flux that allows the material to be prepared at lower temperature. (*78*)

5.3.6 Electronic Structure

The calculated band structure as well as the total and partial density of states (DOS) diagrams for Li_2ZnSiS_4 are displayed in Figure 5.6. As shown in the band structure diagram, the valence band maximum (VBMa) and the conduction band minimum (CBMi) are both located at the Γ-point in the Brillouin zone. Therefore, the plot indicates that this material is a direct bandgap semiconductor in which the Fermi level (E_f) is slightly above the VBMa. The difference between the CBMi and VBMa results in a calculated bandgap of 3.46 eV. The underestimation of the bandgap using DFT with the Perdew-Burke-Ernzerhof generalization gradient approximation (PBE-GGA) function, is a well-known limitation of this calculation. (*79*)

To better understand the origin of the bandgap, the partial density of states (PDOS) has been carefully examined. The PDOS diagrams, indicate that the states at the VBMa, 0 eV to -2 eV, are primarily due to contributions from the *p* orbitals of sulfur. In this region, there are only

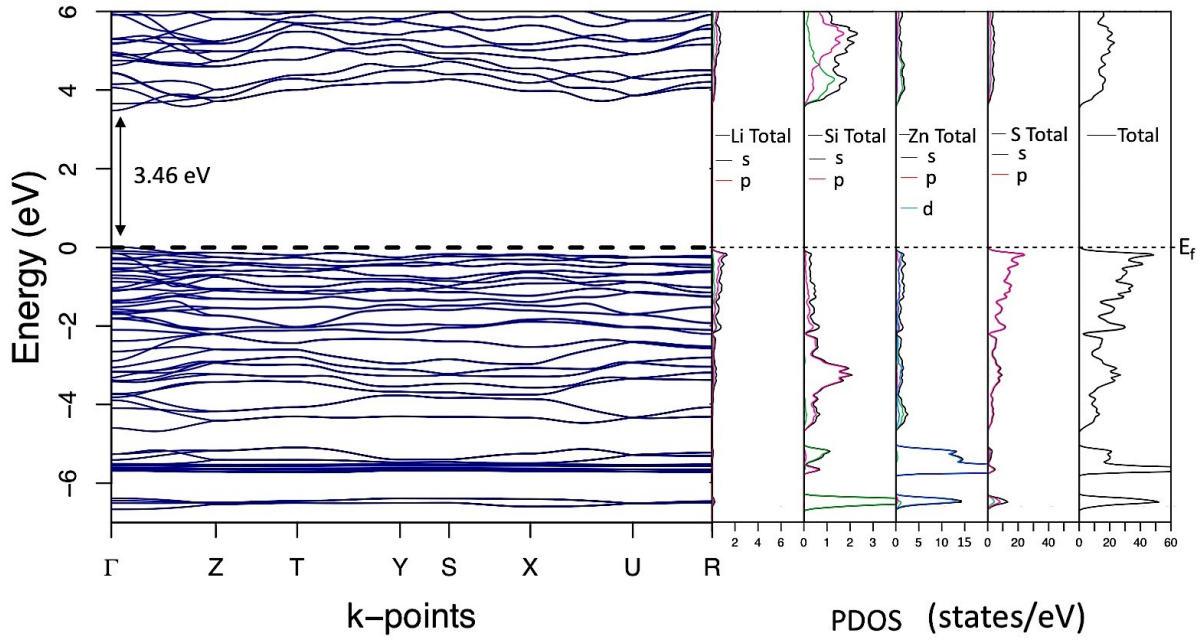

Figure 5.6: Electronic band structure and total and partial density of states for Li_2ZnSiS_4. The *s*, *p* and *d* orbitals are displayed in green, red and blue respectively.

minor contributions from the zinc *p*, zinc *d*, germanium *p*, lithium *s* and lithium *p* orbitals. The zinc *d* orbitals provide the dominant impact on the states in the region -4.5 eV to -6.5 eV. The major involvement of the germanium *p* orbitals lies in the vicinity of -2 eV to -4.5 eV, while the germanium *s* orbitals provide their main influence on the section from -4.5 eV to -6.5 eV. Unlike the other elements, the lithium atomic orbitals have very little bearing over the entire valence band due to their highly ionic interactions with sulfur in the structure. The CBMi starts at approximately 3.5 eV to 4.5 eV is mostly impacted by the *p* orbitals of sulfur and the *s* orbitals of zinc and germanium. While the *s* orbitals of germanium have a more significant role, the *p* orbitals of germanium also contribute to this area. This trend for the germanium orbitals switches after 4.5 eV and the *p* orbitals dictate the element's contribution, with the *s* orbitals effects becoming minimal. After 4.5 eV, further into the conduction band the sulfur orbitals influences persists as described previously. As in the case of the VBMa, the lithium orbitals have an insignificant role until high into the conduction band past 6 eV.

The Zhou group briefly discusses the electronic band structure and partial density of states calculations done using first principle theory with CASTEP. (*57*) Zhou et al calculated a direct bandgap of 3.17 eV at the Γ-point. (*57*) In agreement with our findings, the Zhou group also reported that the sulfur *p* orbitals are the major contributor to the VBMa and the CBMi is a result of zinc *s* orbitals. (*57)*

To emphasize the effect that the choice of elements has on the orbital contributions, a comparison of the PDOS of Li_2ZnSiS_4 to the related compounds Ag_2ZnSiS_4 and Cu_2ZnSiS_4 follows. As stated previously, the atomic orbitals of the lithium atoms do not have a significant effect on the PDOS; however, in comparison, the monovalent cations in Ag_2ZnSiS_4 and Cu_2ZnSiS_4 have a profound effect on the VBMa and the CBMi. (*20,68*) This is a direct result of the atomic

orbital contributions of the silver and copper *d* orbitals to the VBMa. The PDOS of Li_2ZnSiS_4, Ag_2ZnSiS_4 and Cu_2ZnSiS_4 are similar in regard to the orbital contributions of zinc. (*20,68*) In general, the zinc orbitals for all three of these compounds have a relatively small impact on the VBMa and CBMi. (*20,68*) This suggests that a series of compound of the formula Li_2-II-SiS_4 could exist and exhibit wide bandgaps like that of Li_2ZnSiS_4.

5.4. Conclusions

While the Zhou group was the first to report Li_2ZnSiS_4, this work assessed the thermal stability and presented a more in-depth analysis of the electronic structure and partial density of states. In summary, Li_2ZnSiS_4 is a wide bandgap material. The experimental bandgaps of Ag_2ZnSiS_4 and α/β-Cu_2ZnSiS_4 are 3.28 eV and 3.0/3.2 eV, respectively, which are significantly smaller than the experimental bandgap of Li_2ZnSiS_4 reported in this publication. (*20,68*) In future work, the DTA data reported here could potentially be used as a guide for the synthesis of large crystals of Li_2ZnSiS_4. Zhou et al collected the SHG, measurements using a 2.09 μm laser and determined that Li_2ZnSiS_4 is type-I phase-matchable and has a SHG response 1.1 times greater than $AgGaS_2$. (*57*) The LIDT was also measured by Zhou et al and was found to be 10 times that of $AgGaS_2$. (*57*) Based on the combined data from our study and that of the Zhou group, Li_2ZnSiS_4 has potential for NLO applications particularly those operating at higher powers. Yet, the difficulty of synthesizing Li_2ZnSiS_4 should be considered. If this material is to be further investigated for large-scale crystal growth and commercial use, the difficult synthesis may be a limiting factor.

5.5 References

(1) Todd, M.W.; Provencal, R.A.; Owano, T.G.; Paldus, B.A.; Kachanov, A.; Vodopyanov, K.L.; Hunter, M.; Coy, S.L.; Steinfeld, J.I.; Arnold, J.T., *Appl. Phys. B*, **2002**, *75*, 367-376.

(2) Williams, O.M., *Infrared Phys. Technol.*, **1998**, *39*, 473-486.

(3) Knuteson, D.J.; Singh, N.B.; Kanner, G.; Berghmans, A.; Wagner, B.; Kahler, D.; McLaughlin, S.; Suhre, D.; Gottlieb, M., *J. of Cryst. Growth*, **2010**, *312*, 1114-1117.

(4) Zuclich, J.A.; Lund, D.J.; Stuck, B.E., *Health Physics*, **2007**, *92*, 15-23.

(5) Richardson, M.A.; Coath, J.A., *Opt. Laser Technol.*, **1998**, *30*,137-140.

(6) Lu, W.; Liu, L.; Sun, J.; Pan, W., *Optik*, **2008**, *119*, 388-394.

(7) Chatterjee, U., *Pramana-J. Phys,*, **2014**, *82*, 29-38.

(8) Stoeppler, G.; Schellhorn, M.; Eichhorn, M., *Laser Physics*, **2012**, *22*, 1095-1098.

(9) Tura, A.; Maran, A.; Pacini, G., *Diabetes Res. Clin. Pract.*, **2007**, *77*, 16-40.

(10) Amaral, C.E.F.; Wolf, B., *Med. Eng. Phys.*, **2008**, *30*, 541-549.

(11) Haidar, S.; Miyamoto, K.; Ito, H., *Opt. Commun.*, **2004**, *241*, 173-178.

(12) Vaicikauskas, V.; Kaucikas, M.; Svedas, V., *Rev. Sci. Instrum.*, **2007**, *78*, 023106.

(13) Hopkins, F.K., *Opt. Photonics News*, **1998**, *9*, 32-38.

(14) Kim, Y.; Seo, I-S.; Martin, S. W.; Baek, J.; Halasyamani, P.S.; Arumugam, N.; Steinfink, H., *Chem. Mater.*, **2008**, *20*, 6048-6052.

(15) Luo, Z.-Z.; Lin, C.-S.; Cui, H.-H.; Zhang, W.-L.; Zhang, H.; He, Z.-Z.; Cheng, W.-D., *Chem. Mater.*, **2014**, *26*, 2743-2749.

(16) Wu, K.; Yang, Z.; Pan, S., *Chem. Mater.*, **2016**, *28*, 2795-2801.

(17) Li, Y.-Y.; Liu, P.-F.; Wu, L.-M., *Chem. Mater.*, **2017**, *29*, 5259-5266.

(18) Li, G.; Wu, K.; Liu, Q.; Yang, Z.; Pan, S., *J. Am. Chem. Soc.*, **2016**, *138*, 7422-7428.

(19) Brant, J.A.; Clark, D.J.; Kim, Y.S.; Jang, J.I.; Zhang, J.-H.; Aitken, J.A., *Chem. Mater.*, **2014**, *26*, 3045-3048.

(20) Rosmus, K.A.; Brant, J.A.; Wisneski, S.D.; Clark, D.J.; Kim, Y.S.; Jang, J.I.; Brunetta, C.D.; Zhang, J.-H.; Srnec, M.N.; Aitken, J.A., *Inorg. Chem.*, **2014**, *53*, 7809-7811.

(21) Brant, J.A.; Clark, D.J.; Kim, Y.S.; Jang, J.I.; Weiland, A.; Aitken, J.A., *Inorg. Chem.*, **2015**, *54*, 2809-2819.

(22) Li, S.-F.; Jiang, X.-M.; Liu, B.-W.; Yan, D.; Lin, C.-S.; Zeng, H.-Y.; Guo, G.-C., *Chem. Mater.*, **2017**, *29*, 1796-1804.

(23) Luo, Z.-Z.; Lin, C.-S.; Cui, H.-H.; Zhang, W.-L.; Zhang, H.; Chen, H.; He, Z.-Z.; Cheng, W.-D., *Chem. Mater.*, **2015**, *27*, 914-922.

(24) Lin, H.; Chen, H.; Zheng, Y.-J.; Yu, J.-S.; Wu, X.-T.; Wu, L.-M., *Dalton Trans.*, **2017**, *46*, 7714.

(25) Wu, K.; Yang, Z.; Pan, S., *Inorg. Chem.*, **2015**, *54*, 10108-10110.

(26) Zhang, J.-H.; Clark, D.J.; Brant, J.A.; Sinagra, C.W. III; Kim, Y.S.; Jang, J.I.; Aitken, J.A., *Dalton Trans.*, **2015**, *44*, 11212-11222.

(27) Lv, S.; Wu, Q.; Meng, X.; Kang, L.; Zhong, C.; Lin, Z.; Hu, Z.; Chen, X.; Qin, J., *J. Mater. Chem. C*, **2014**, *2*, 6796-6801.

(28) Zhang, H.; Zhang, M.; Pan, S.; Dong, X.; Yang, Z.; Hou, X.; Wang, Z.; Chang, K.B.; Poeppelmeier, K.R., *J. Am. Chem. Soc.*, **2015**, *137*, 8360-8363.

(29) Zhang, W.; Yu, H.; Cantwell, J.; Wu, H.; Poeppelmeier, K.R.; Halasyamani, P.S., *Chem. Mater.*, **2016**, *28*, 4483-4491.

(30) Chen, Z.; Zhang, Z.; Dong, X.; Shi, Y.; Liu, Y.; Jing, Q., *Cryst. Growth Des.*, **2017**, *17*, 2792-2800.

(31) Wu, K.; Yu, H.; Zhang, W.; Cantwell, J.; Poeppelmeier, K.R.; Pan, S.; Halasyamani, P.S., *Cryst. Growth Des.*, **2017**, *17*, 4405-4412.

(32) Wu, Q.; Liu, H.; Jiang, F.; Kang, L.; Yang, L.; Lin, Z.; Hu, Z.; Chen, X.; Meng, X.; Qin, J., *Chem. Mater.*, **2016**, *28*, 1413-1418.

(33) Huang, Y.; Meng, X.; Gong, P.; Yang, L.; Lin, Z.; Chen, X.; Qin, J., *J. Mater. Chem. C*, **2014**, *2*, 4057-4062.

(34) Wu, Q.; Meng, X.; Zhong, C.; Chen, X.; Qin, J., *J. Am. Chem. Soc.*, **2014**, *136*, 5683-5686.

(35) Aitken, J. A.; Brant, J. A.; Clark, D. J.; Kim, Y. S.; Jang, J. I. *Nonlinear Optics: Fundamental, Applications and Technological Advances*; Wilkins F. Ed.; Nova Science Publishers Inc.: New York, **2014** (Pages 1-61)

(36) Halasyamani, P.S., *Chem. Mater.*, **2004**, *16*, 3586-3592.

(37) Kunz, M; Brown, I.D., *J. Solid State Chem.*, **1995**, *115*, 395-406.

(38) Kim, Y.H.; Lee, D.W.; Ok, K.M., *Inorg. Chem.*, **2014**, *135*, 11942-11950.

(39) Lu, H.; Gautier, R.; Donakowski, M.D.; Tran, T.T.; Edwards, B.W.; Nino, J.C.; Halasyamani, P.S.; Liu, Z.; Poeppelmeier, K.R., *J. Am. Chem. Soc.*, **2013**, *53*, 11942-11950.

(40) Ra, H.-S.; Ok, K.M., Halasyamani, P.S.; *J. Am. Chem. Soc.*, **2003**, *125*, 7764-7765.

(41) Kim, S.H.; Yeon, J.; Halasyamani, P.S., *Chem. Mater.*, **2009**, *21*, 5335-5342.

(42) Phanon, D.; Gautier-Luneau, I., *Angew. Chem. Int. Ed.*, **2007**, *46*, 8488-8491.

(43) Ok, K.M.; Halasyamani, P.S., *Angew. Chem. Int. Ed.*, **2004**, *43*, 5489-5491.

(44) Li, P.-X.; Hu, C.-L.; Xu, X.; Wang, R.-Y.; Sun, C.-F.; Mao, J.-G., *Inorg. Chem.*, **2010**, *49*, 4599-4605.

(45) Huang, Y.-Z.; Wu, L.-M.; Wu, X.-T.; Li, L.-H.; Chen, L.; Zhang, Y.-F., *J. Am. Chem. Soc.*, **2010**, *132*, 12788-12789.

(46) Phanon, D.; Bentria, B.; Benbertal, D.; Mosset, A.; Gautier-Luneau, I., *Solid State Sciences*, **2006**, *8*, 1466-1472.

(47) Goryunova, A. J. C. *The Chemistry of Diamond-like Semiconductors*, The MIT Press, Cambridge MA, **1964**.

(48) Parthé, E. *Crystal Chemistry of Tetrahedral Structures*, Gordon and Breach Science Publishing, New York, NY, **1964**.

(49) Brunetta, C.D.; Minsterman III, W. C.; Lake, C.H.; Aitken, J. A., *J. Solid State Chem.* **2012**, *187*, 177-185.

(50) Pauling, L, *J. Am. Chem. Soc.* **1929**, *51*,1010-1026.

(51) Ohmer, M.C.; Pandey, R., *MRS Bull*, **1998**, *23*, 16-22.

(52) Petrov, V.; Zondy, J.-J.; Bidault, O.; Isaenko, L.; Vendenyapin, V.; Yelisseyev, A.; Chen, W.; Tyazhev, A.; Lobanov, S.; Marchev, G.; Kolker, D., *J. Opt. Soc. Am. B.*, **2010**, *27*, 1902-1927.

(53) Isaenko, L; Yelisseyev, A; Lobanov, S.; Krinitsin, P.; Petrov, V.; Zondy, J.-J., *J. Non-Cryst. Sol.*, **2006**, *352*, 2439-2443.

(54) Jackson, A.G.; Ohmer, M.C., LeClair, S.R., *Infrared Phys. Techn*, **1997**, *38*, 233-244.

(55) Clark, D.J.; Zhang, J.-H.; Weiland, A.; Brant, J.A.; Kim, Y.S.; Jang, J.I.; Aitken, J.A., manuscript in preparation.

(56) Catella, G.C.; Burlage, D., *MRS Bull*, **1998**, *23*, 28-36.

(57) Li, G.; Chu, Y.; Zhou, Z., *Chem Mater.*, **2018**, *30*, 602-606.

(58) SAINT and SADABS are part of the Apex2 software package v2.1-4 Program for Data Collection and Reduction on Bruker AXS CCD Area Detector Systems. *Apex2 software package v2.1-4*; Bruker Analytical X-ray Systems, Inc., Madison, WI, **2005**.

(59) SHELXTX, release 6.14; Bruker AXS; Madison, WI, **2005**.

(60) CrystalMaker, version 9, CrystalMaker Software Limited, Oxfordshire, UK.

(61) X.p.H. Plus, PANalytical. B.V., Almelo, the Netherlands.

(62) J. Faber and T. Fawcett, Acta Crystallogr., Sect. B: Struct. Sci., **2002**, *58*, 325–332.

(63) V. Džimbeg-Malčić, Ž. Barbarić-Mikočević, K. Itrić, *Technical Gazette*, **2011**, *18*, 117-124.

(64) Blaha, P.; Schwarz, K; Madsen, G.K.H.; Kvasnicka, D.; Luitz, J., Vienna University of Technology, Austria **2011**.

(65) Perdew, J.P.; Burke, S.; Ernzenhof, M., *Phys. Rev. Lett.*, **1996**, *77*, 3865-3868.

(66) Yamaguchi, H.; Akatsuka, K.; Setoguchi, M.; Takaki, Y., *Acta Cryst.,* **1979**, *B35*, 2680-2682.

(67) A.R. West, F.P. Glasser, *J. Solid State Chem*., **1972**, *4*, 20–28.

(68) Brunetta, C.; Karuppannan, B.; Rasmus, K. A.; and Aitken, J. A., *J. Alloys and Compd.*, **2012**, *516*, 65-72.

(69) Rosmus, K. A.; Aitken, J. A., *Acta Cryst.*, **2011**, *E67*, i28.

(70) Tran, T.K.; Park, W.; Tong, W.; Kyi, M.M.; Wagner, B.K.; Summers, C.J. *J. Appl. Phys.*, **1997**, *81*, 2803-2809.

(71) Soref, R.A.; Moos, H.W., *J. Appl. Phys.,* **1964**, *35*, 2152-2158.

(72) Cardona, M.; Harbeke, G., *Phys. Rev.*, **1965**, *137*, A1467.

(73) Theis, D., *Phys. Stat. Sol.*, **1977**, *79*, 125-130.

(74) Chemla, D.S.; Kupecek, P.J.; Robertson, D.S.; Smith, R.C., *Opt. Commun.,* **1971**, *3*, 29-31.

(75) Route, R.K.; Feigelson, R.S.; Raymakers, R.J., *J. Cryst. Growth.*, **1974**, *24*, 390-395.

(76) Eifler, A.; Reide, V.; Brückner, J.; Weise, S.; Krämer, V.; Lippold, G.; Schnitz, W.; Bente, K.; Grill, W., *Jpn. J. Appl. Phys.*, **2000**, *39*, 279-281.

(77) Miessler, G.L.; Tarr, D.A., *Inorganic Chemistry*, 4th edition, Pearson Education Inc., New Jersey, **2011**.

(78) Poser, J.D.; Meyer, H.-J., *Z. Anorg. Allg. Chem.*, **2012**, *638*, 1293-1296.

(79) Lee, J.G., *Computational Materials Science: An Introduction*, 1st edition, CRC Press, Florida, **2012**, 135-141.

Chapter 6: Wurtz-Kesterite and Disordered Wurt-Kesterite Type Cu_2ZnSiS_4: A Study of Polymorphism

6.1 Introduction

Diamond-like semiconductors (DLSs) are used commercially in photovoltaics (*1-3*) and nonlinear optics (*4-16*). They are also being investigated for their use in thermoelectrics, (*17,18*) photocatalysis, (*19*) lithium-ion batteries, (*20-22*) magnetoelectronics (*23-25*) and spintronics. (*26,27*) The ease of crystallization is of paramount importance, in addition to the properties of a material, when studying its potential for commercial use. There are several DLSs that exist as polymorphs including ZnS, (*28,29*) Cu_2ZnSnS_4, (*30,31*) Ag_2CdSnS_4, (*32,33*) and Li_2MnSnS_4. (*34*) Chen and coworkers have evaluated the ground state energies for different structures of quaternary DLSs and found that in many cases there is little difference in the ground state energy between a structure derived from cubic diamond versus that derived from hexagonal diamond. (*35*)

Zinc sulfide is one example of a DLS in which multiple polymorphs exist. Zinc sulfide exists mainly in two crystalline forms, the cubic, $F\bar{4}3m$, (*28*) sphalerite type and the hexagonal, $P6_3mc$, (*29*) wurtzite type, although over 190 polymorphs of zinc sulfide have been reported with varying degrees of hexagonal and cubic closest packing. (*36-38*) While the alpha and beta polymorphs are similar, they differ in their birefringence. (*39*)

Cu_2ZnSnS_4 (CZTS) is of interest for its potential use as the absorber layer of thin-film solar cells, but the polymorphs of CZTS are an issue that has plagued this material for decades. (*30,31*) To this end, abundant research has been conducted on CZTS and three polymorphs have been reported, all tetragonal crystal structures; kesterite ($I\bar{4}$) (*31*), stannite ($I\bar{4}2m$) and primitive-mixed CuAu structure ($P\bar{4}2m$, this structure is still theoretical). (*40*) Obtaining one phase when three polymorphs have been reported is a challenge, which is only complicated more by the presence of

stable secondary and ternary phases that are often present in reaction products. Secondary phases are frequently present, as there is a very narrow existence region of a single phase in the equilibrium phase diagram of CZTS. (*41*) The binary and ternary phases commonly present in reactions targeting CZTS are ZnS, CuS, Cu_2S, SnS_2 and Cu_2SnS_3. (*41-45*) Changes to the reactant ratio have been attempted to eliminate the formation of secondary phases, although this has also lead to off-stoichiometric formation of Cu_2ZnSnS_4 polymorphs. (*31, 46*) Adjustments to the synthesis process have also been shown to influence the optoelectronic properties. (*31*) The combination of the three reported polymorphs, the off-stoichiometric polymorphs, and the secondary phases all affect the solar cell efficiency, reported to be approximately 8.5%, too low for commercial applications. (*45*) Crystallographic defects also create issues relating to efficiency of CZTS in solar cells. (*45-50*) One defect of note are the anti-site defects among the isoelectronic Cu^+ and Zn^{2+} cations. *(46,47,49,51*)

α/β-Cu_2ZnSiS_4 is a related DLS that has already been investigated for its NLO properties, but further assessment of this material has been hindered by the co-synthesis of two polymorphs. Prior to 2011, only the alpha polymorph of Cu_2ZnSiS_4 had been reported with the wurtz-stannite structure ($Pmn2_1$). (*52-56*) The beta polymorph was later reported to crystallize in the *Pn* space group with the wurtz-kesterite structure by Rosmus et. al. (*56*) At the time, the Cu^+ and Zn^{2+} site occupation factors from these studies were ambiguous since the X-ray diffraction data were insufficient to differentiate between the isoelectronic Cu^+ and Zn^{2+} ions and determine the extent of the disorder without neutron data. (*57*) Rosmus et. al. determined that the bandgaps were 3.2 eV and 3.0 eV for β and α respectively.(*57*) Previously, the bandgap of Cu_2ZnSiS_4 had been reported ranging from 2.97-3.41 eV, but it should be noted that these measurements were reported before the beta polymorph was discovered. (*55,58,59*) However, neither wurtz-stannite or wurtz-

kesterite are the predicted lowest energy structure for Cu_2ZnSiS_4, as determined by Chen and coworkers, rather they predicted a kesterite structure would be most stable. (*35*) The NLO properties of α/β-Cu_2ZnSiS_4 were later investigated on a sample that was determined to be a 60/40 mixture of the α/β phases. (*60*) The $\chi^{(2)}$ was established to be 15±2 pm/V and the laser induced damage threshold (LIDT) has been reported as 2.0 GW/cm^2 when measured at λ=1064 nm with a pulse width of 30 ps, which exceeds that of $AgGaSe_2$ measured under the same conditions. (*60*) The optical transparency was measured to be >80% from 0.7-25 μm. (*60*) As α/β-Cu_2ZnSiS_4 has a larger LIDT than commercially available $AgGaSe_2$ this material was deemed a potential NLO material, but the presence of two polymorphs makes it unclear whether one or both of the materials have good NLO properties and it is not apparent how much, if any difference between their properties.

The need to isolate the α and β polymorphs of Cu_2ZnSiS_4 was the inspiration for this work. This work experimented with the synthetic variables, in particular cooling rate, to observe the effect on the presence/amount of the polymorphs in the reaction product. Previous work by Rosmus et al. indicated that Rietveld refinement could be utilized to differentiate between the polymorphs and assess the phase fractions with synchrotron data. Here we also employed neutron diffraction data in order to confidently refine the occupancies of the isoelectronic ions Cu^+ and Zn^{2+}. Due to the extreme similarity in the diffraction patterns of the polymorphs, even with high-resolution synchrotron data, a more powerful technique, solid-state NMR was also used and is presented here.

6.2 Experimental

6.2.1 Synthesis

Cu_2ZnSiS_4 was originally synthesized by heating the combination of reactants to 1000 °C, dwelling for 96 hours and then cooling to room temperature at a rate of 7.5 °C/hour. (*57*) Samples of the "Cu_2ZnSiS_4" composition were prepared via high-temperature, solid-state synthesis. The reaction mixtures were prepared by weighing out Cu (2 mmol, 99.999%, Strem), Zn (1 mmol, 99.999%, Strem), Si lump (1 mmol, ground using a diamonite mortar and pestle, 99.999+%, Alfa Aesar) and S (4 mmol, sublimed powder, 99.5%, Fisher Scientific), which were combined in an agate mortar and pestle and ground for 10 minutes. The ground starting materials were housed in 9 mm o.d. carbon-coated, fused-silica tubes that were produced by pyrolyzing acetone and inserted into 12 mm o.d. fused-silica tubes that were subsequently sealed under a vacuum of 10^{-4} mbar. The reaction vessels were heated to 1000 °C in 12 hours, dwelled at 1000 °C for 96 hours, and then cooled using one of seven cooling rates including; ice quenching, air quenching, 100 °C/hour, 25 °C/hour, 25 °C/hour, cooling to 400°C at a rate of 7.5 °C/hour before cooling ambiently, 7.5 °C/hour and 2 °C/hour.

6.2.2 Optical Diffuse Reflectance UV-vis-NIR

A Varian Cary 5000 spectrometer, equipped with a Harrick Praying Mantis diffuse reflectance attachment was used to collect the optical diffuse reflectance spectra in the ultraviolet, visible and near infrared regions. Barium sulfate (99.92%, Fisher) was used as a 100% reflectance standard. The ground samples were placed on top of the barium sulfate standard, which was proloaded in the sample cup, and collected. Both the background and the sample were scanned

from 2500 nm to 200 nm at a rate of 600 nm/min. The Kubelka-Munk transformation was used to convert the data, that were collected as percent reflectance (%R), to relative absorption (α_{KM}). (*61*)

6.2.3 Synchrotron X-ray Diffraction

High-resolution synchrotron X-ray powder diffraction data were collected for powder samples of "Cu_2ZnSiS_4" using beamline 11-BM at the Advanced Photon Source (APS), Argonne National Laboratory. The 11-BM bending magnet source operates at an electron energy of 7 GeV with a critical photon energy of 19.5 keV and operates over the energy range of 14 keV-35keV. The flux is ~$5x10^{11}$ phs/sec at 30 keV. For the collection a Si (111) double crystal monochromator was used with sagittally bent Si(111) horizontal focusing and 1 meter Si/Pt mirror vertical focusing. A beam size of 1.5 mm x 0.5 mm was used. The detection system included 12 independent analyser sets with 2θ separation of ~2° Si (111) analyser crystals and $LaCl_2$ scintillation detectors. The measurements were collected at ambient temperature over a 2θ range of 0.5°-130°, using a minimum 2θ step size of 0.0001°.

6.2.4 Neutron Diffraction

Neutron powder diffraction measurements were performed using 5g of material at the National Institute of Standards and Technology Center for Neutron Research (NCNR). Data were collected at the high-resolution neutron powder diffractometer, BT1, utilizing a Cu (311) monochromator with a 90° take-off angle, and in-pile collimation of 60 minutes of arc were used corresponding to a neutron wavelength of 1.5397(2) Å. Data were collected over the range of 3-168° 2θ with a step size of 0.05°. Samples were loaded into vanadium sample cans (50 mm tall, i.d 9.2 mm) in an He environment glovebox, and sealed with an indium o-ring, and

subsequently mounted onto a bottom-loaded closed cycle (CCR) refrigerator. Samples were cooled to base temperature (c.a. 5 K) for measurement.

6.2.5 Rietveld Refinement of Neutron Data

The single crystal structure of the beta polymorph from the work of Rosmus et. al. was used as the starting model for the refinements. (*56*) The gamma phase model also used this single crystal structure, but dual occupancy of the Cu and Zn sites was added. The Rietveld refinement was completed with the GSAS II (*62*) software in conjunction with the EXPGUI interface. For all samples, the unit cell parameters, atomic positions, and isotropic atomic displacement parameters were refined. The background was fit using the Chebyschev function. (*63*) The peak shapes were fit using Gaussian and Loretzian terms. Additionally, site occupation factors were refined for the sites that were disordered between copper and zinc.

6.2.6 Solid-State MAS-NMR

^{65}Cu spectra were acquired on a Bruker Avance III 500 MHz spectrometer with a 2.5 mm CP-MAS probe. A full shifted echo acquisition sequence ($\frac{\pi}{8} - \tau - \frac{\pi}{4}$ −acq) was used. The radio-frequency (r.f.) field was set to 104 kHz and τ to 0.5 ms. Spectra were acquired under MAS (30 kHz) condition with a recycle time of 0.5 s. ^{65}Cu spectra were referenced at 0 ppm against solid state CuCl.

The ^{67}Zn spectrum of the sample cooled at 2°C/hr was acquired on a Bruker Avance III 500 MHz spectrometer with a 4 mm 'low γ' CP-MAS probe. The CPMG (Carr-Purcell-Meiboom-Gill) approach combined with MAS.[64] r.f. field of 23 kHz was used for excitation ($\pi/6$) and refocusing ($\pi/3$) pulses. The recycle time was 1s and MAS frequency was set to 14055 Hz for

synchronization purposes. The final spectrum was constructed by adding the first 12 full echoes of the CPMG acquisition. The ^{67}Zn spectrum was referenced at 0 ppm against a $Zn(NO_3)_2$(aq) solution.

^{29}Si spectra were acquired on a Bruker Avance III 300 MHz spectrometer with a 4mm CP-MAS probe. ^{29}Si MAS (10 kHz) spectra were obtained by using a single $\pi/3$ pulse excitation of 3.5 μs. The recycle time was set to 60 s. Spectra were referenced at 0 ppm against TMS.

The "dmfit" software[65] was used for the spectral decompositions.

6.3 Results and Discussion

6.3.1 Optical Diffuse Reflectance

The absorption edge of each reaction product was assessed using diffuse reflectance is the ultraviolet, visible and near infrared regions to estimate the bandgap and are listed in Table 6.1. For every sample, the experimentally measured absorption edge is lower in energy than the bandgap reported by Rosmus et al. The difference in energy may due to the ratio of polymorphs present.

Table 6.1: Experimental absorption edges of "Cu_2ZnSiS_4" samples with different cooling rates.

Reaction Cooling Rate	Absorption edge (eV)
Ice Quench	2.72
Air Quench	2.78
100 °C/hour	2.76
25 °C/hour	2.79
1000 °C to 400 °C at 7.5 °C/hour, 400 °C to 25 °C ambiently	2.70
7.5 °C/hour	2.89
2 °C/hour	2.84

6.3.2 Rietveld Refinement of Synchrotron Data

To determine the effect of cooling rate on the polymorphic phase fractions Rietveld refinement was used. The calculated X-ray powder diffraction patterns of α-Cu_2ZnSiS_4 ($Pmn2_1$) and β-Cu_2ZnSiS_4 (Pn) are indistinguishable via laboratory-grade X-ray powder diffraction data. Thus, it was essential to determine the phase fractions within the reaction products using synchrotron X-ray powder diffraction data. Initial analysis of the synchrotron data indicated that, in addition to the presence of α/β-Cu_2ZnSiS_4, the samples also contained sphalerite type ZnS. (*66*) The starting model for the Rietveld refinement included three phases; α-Cu_2ZnSiS_4, β-Cu_2ZnSiS_4 and sphalerite type ZnS. This model did not refine well, which lead to the thought that both polymorphs may not be present in the sample. Therefore, refinement of the data proceeded with two new models, one using only the alpha phase and ZnS, and the other including only the beta phase and ZnS. The refinements using two phases were less effective than those with three phases. Refinement with three phases was again attempted, but this time the order in which the α-Cu_2ZnSiS_4 and β-Cu_2ZnSiS_4 polymorphs were refined was tested. Changing the order in which the polymorphs were refined resulted in poor refinement statistics, refinements were attempted with both the alpha phase and the beta phase refined first. The next models included all three phases but refinements of the site occupation factors were introduced to allow, copper deficiencies in the alpha polymorph, copper deficiencies in the beta polymorph, zinc deficiencies in the alpha polymorph and zinc deficiencies in the beta polymorph. These models also failed to yield sufficient refinements.

6.3.3 Solid-State MAS-NMR

Based on the results from Rosmus et al., differentiation between the polymorphs should be possible when using synchrotron data, although it was unsuccessful for this work. Solid-state NMR was then pursued to determine an appropriate starting model for the Rietveld refinement of the diffraction data. Figures 6.1 and 6.2 display the ^{65}Cu spectra for samples obtained via different cooling rates. It can be observed that all the spectra look similar. They only differ in that the "horns" that become gradually smoother as the cooling rate increases. This reflects larger electric field gradient (EFG) distributions for faster cooling rates. This is significant, as the EFG at a given crystallographic site is very sensitive to the local geometry of the site. The stronger the distortion of this site, the higher the EFG. When distortions at a given site are not exactly the same for all the unit cells, EFG distribution occurs that induces ^{65}Cu line broadening through quadrupole interaction, which is the coupling between the EFG and the quadrupole moment

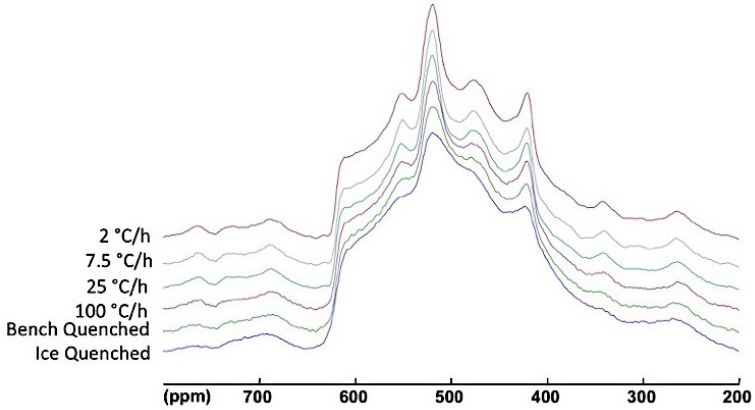

Figure 6.1: ^{65}Cu solid-state MAS-NMR spectra from 800 to 200 ppm comparing samples of varying cooling rates.

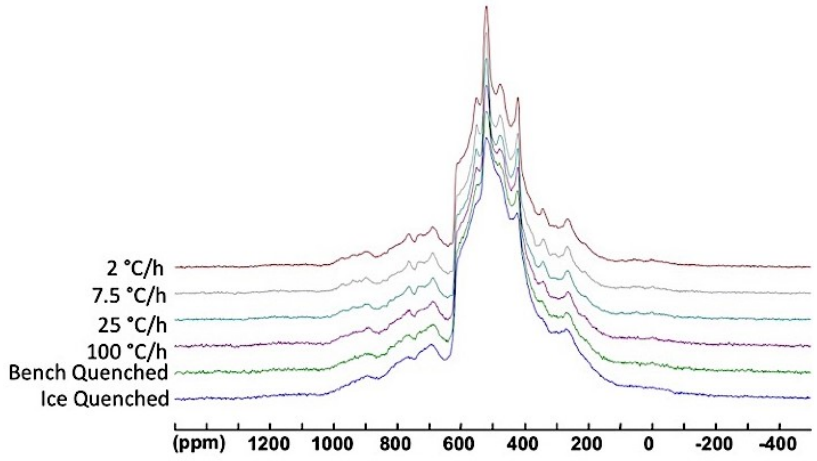

Figure 6.2: ^{65}Cu solid-state MAS-NMR spectra from 1500 to -400 ppm comparing samples obtained by varying reaction cooling rates.

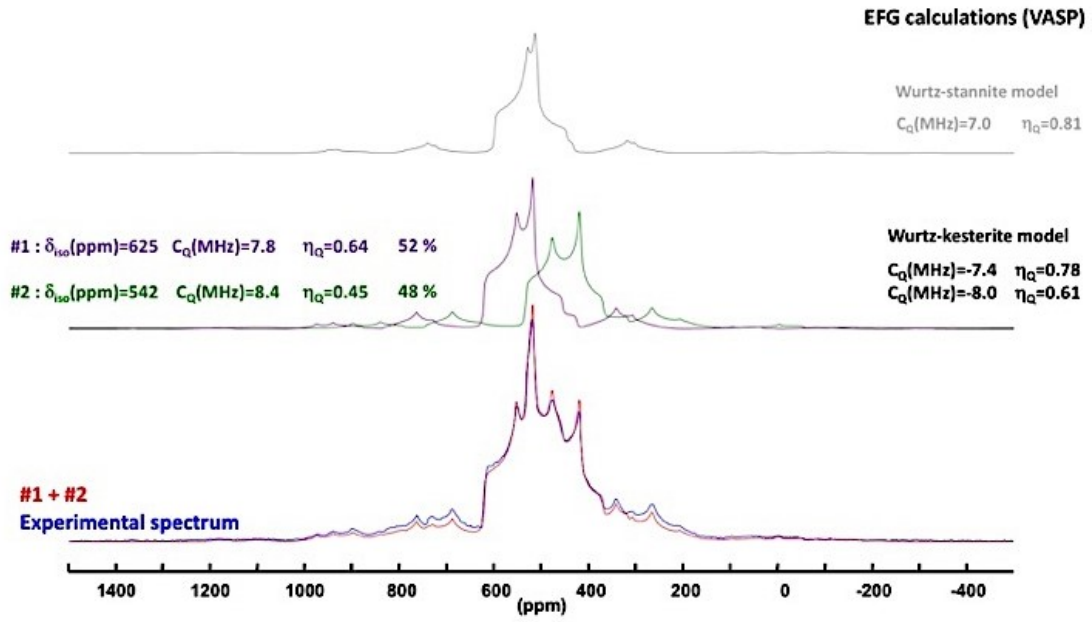

Figure 6.3: Calculated ^{65}Cu solid-state NMR spectra of α-Cu_2ZnSiS_4 and β-Cu_2ZnSiS_4 in grey and purple/green, respectively. The combined calclated β-Cu_2ZnSiS_4 (red) compared to the experimentally collected data (blue).

of the nucleus. However, since the "horns" are visible in each spectrum, the actual EFG distributions are weak. The change in the "horns" also indicates that there is a change in the products of the different cooling rates. The ^{65}Cu spectra can be used to differentiate between the alpha and beta polymorphs. This is possible, as the simulated ^{65}Cu spectra for alpha-Cu_2ZnSiS_4 and beta-Cu_2ZnSiS_4 show one and two peaks respectively, indicative of one and two crystallographically unique copper atoms in the structures. Figure 6.3 demonstrates that the experimental spectrum matches the calculated spectrum for the beta polymorph. The ^{67}Zn spectra

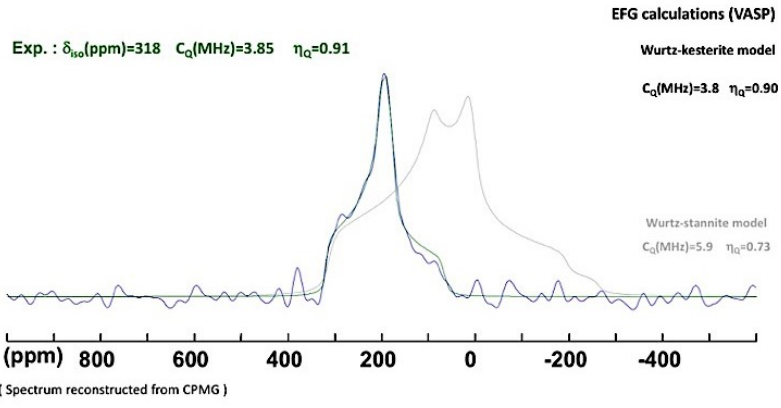

Figure 6.4: ^{67}Zn solid-state NMR comparing the calculated α-Cu_2ZnSiS_4, β-Cu_2ZnSiS_4 and experimental data in grey, green and blue respectively.

further indicate that only the beta polymorph is present in the sample cooled at 7.5 °C/hour to 400 °C and ambiently to room temperature, as the experimental spectrum matches the calculated beta polymorph, Figure 6.4. There is no evidence of the alpha phase in NMR. Since the alpha-phase was not detected, yet it was not possible to refine the synchrotron data using only the beta phase, a disordered beta phase was hypothesized as similar results had previously been observed for Cu_2ZnSiS_4. (*51*)

6.3.4 Rietveld Refinement of Neutron Diffraction Data

Neutron diffraction data were also collected on the sample cooled at 7.5 °C/hour to 400 °C and ambiently to room temperature. Neutron diffraction data were collected because the solid-state NMR data indicated that only the beta polymorph was present, while refinement of the synchrotron data with only the beta polymorph and ZnS did not refine appropriately. The sample with this cooling rate was chosen, as it resulted in the least amount of ZnS present in the sample. The neutron diffraction data were collected to determine if mixing of the Cu and Zn sites occurred. Mixing of the isoelectronic cations was suspected as this occurs in the related DLS Cu_2ZnSnS_4. (*46,47,49*)

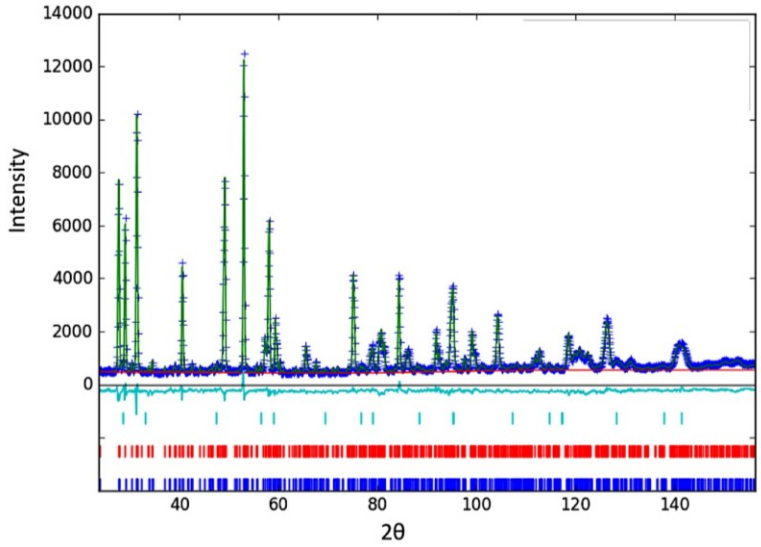

Figure 6.5: Rietveld refinement results for Cu_2ZnSiS_4. The collected neurtron data are plotted using plus signs (+), overlapped with the pattern calculated from the model (green). The expected Bragg reflections for ZnS, beta-Cu_2ZnSiS_4 and gamma-Cu_2ZnSiS_4 are displayed in teal, red and blue tick marks, respectively.

Table 6.2: Refined atomic coordinates and site occupancy factors for the beta-Cu_2ZnSiS_4 phase.

Atom	x	y	z	Site Occupancy	Uiso
Cu	0.91851	0.66740	0.28263	1	0.03569
Cu	0.42048	0.84477	0.52711	1	0.01559
Zn	0.90501	0.68706	0.79141	1	0.01000
Si	0.91787	0.68706	0.79141	1	0.00849
S	0.30157	0.67291	0.78595	1	0.00000
S	0.26808	0.66610	0.25266	1	0.00000
S	0.28585	0.21657	0.48282	1	0.00000
S	0.82691	0.87295	0.54248	1	0.00000

Table 6.3: Refined atomic coordinates and site occupancy factors for the gamma-Cu_2ZnSiS_4 phase.

Atom	x	y	z	Site Occupancy	Uiso
Cu	0.92002	0.67347	0.28131	0.3858	0.01000
Cu	0.42150	0.84478	0.53254	0.5643	0.01000
Cu	0.92293	0.67704	0.76577	0.3941	0.01000
Zn	0.92293	0.67704	0.76577	0.6059	0.01000
Zn	0.92002	0.67347	0.28131	0.6142	0.01000
Zn	0.42150	0.84478	0.53254	0.4357	0.01000
Si	0.92257	0.16732	0.52249	1.0000	0.00905
S	0.29546	0.66357	0.77589	1.0000	0.00465
S	0.28763	0.66713	0.27651	1.0000	0.00133
S	0.25749	0.19155	0.53378	1.0000	0.00235
S	0.80306	0.87375	0.52208	1.0000	0.01888

Rietveld refinement of the neutron diffraction data using the beta phase, a disordered beta phase and ZnS was completed. From this point, the disordered beta phase will be referred to as the gamma phase The gamma phase models dual occupancy of the Cu and Zn sites. These refinement conditions were successful, Figure 6.5, a wR of 6.124% resulted from the above described refinement conditions. The refinement elucidated that the phase fractions of the β-Cu_2ZnSiS_4, modified γ-Cu_2ZnSiS_4 and ZnS phases were 34.6(5)%, 64.0(3)% and 1.32(5)%, respectively. The refined unit cell parameters for β-Cu_2ZnSiS_4 are a = 6.14188, b = 6.40595, c = 7.44157, β = 89.906 and a volume of 292.785 $Å^3$. The refined unit cell parameters for γ-Cu_2ZnSiS_4 are a =

6.13516, b = 6.39438, c = 7.43142, β = 90.082 and a volume of 291.538 Å^3. The refined beta-phase and gamma-phase information is in Tables 6.2 and 6.3, respectively.

6.4 Conclusions

While this work was laid out to determine if there are synthetic conditions under which α-Cu_2ZnSiS_4 could be preferentially synthesized over the β-Cu_2ZnSiS_4 and vice versa, this was not accomplished. The evaluation of the NLO properties of each individual polymorph would be useful in further investigating Cu_2ZnSiS_4 as a new candidate material for IR-NLO applications. Surprisingly, in the experiments presented here, there is no evidence of the alpha polymorph being synthesized. There is no support for the presence of the alpha phase in these samples in the synchrotron X-ray powder diffraction data, the solid-state MAS-NMR data or the neutron powder diffraction data. However, the results from solid-state NMR suggested that, in addition to β-Cu_2ZnSiS_4, a related polymorph, γ-Cu_2ZnSiS_4, which has a disordered kesterite structure (i.e. disordered β-Cu_2ZnSiS_4) exists. A model including this new phase in combination with beta and sphalerite type ZnS refines well using the neutron powder diffraction data of the sample that was cooled at a rate of 7.5 °C/hour to 400°C after which it was cooled ambiently. The presence of an additional polymorph further complicates the evaluation of Cu_2ZnSiS_4 in powder form for IR-NLO applications. Future work should be focused on single crystal growth experiments to determine if they may be more successful in producing only one polymorph of Cu_2ZnSiS_4.

6.5 References

(1) Mitzi, D.B.; Gunawan, O.; Todorov, T.K.; Wang, K.; Guha, S., *Sol. Energy Mater. Sol. Cells*, **2011**, *95*, 1421-1436.

(2) Fella, C.M.; Romanyuk, Y.E.; Tiawari, A.N., *Sol. Energ. Mat.*, **2013**, *119*, 276-277.

(3) Delbos, S., *EPJ Photovolt*, **2012**, *3*, 35004.

(4) Wang, C.; Sahay, P., *Sensors*, **2009**, *9*, 8230-8262.

(5) Persijn, S.; Harren, F.; Vander Veen, A., *Appl. Phys. B*, **2010**, *100*, 383-390.

(6) Williams, O.M., *Infrared Phys. Techn.*, **1998**, *39*, 473-486.

(7) Richardson, M.A.;. Coath, J.A., *Opt. Laser. Technol.*, **1998**, *30*, 137-140.

(8) Eckardt, R.C., *Proc. SPIE*, **1995**, *2469*, 132-140.

(9) Lu, W.; Liu, L.;. Sun, J.; Pan, W., *Opik*, **2008**, *119*, 388-394.

(10) Hopkins, F.K. *Opt. Photonics News*, **1998**, *9*, 32-38.

(11) Hecht, J., *Laser Focus World*, **2014**, *50*, 31-38.

(12) Clewes, R.J.; Howle, C.R.: Stothard, D.J.M.; Dunn, M.H.; Robertson, G.; Miller, W.; Malcom, G.; Maker, G.: Cox, R.; Williams, B.; Russell, M., *Proc. SPIE*, **2012**, *8456*, 85460X.

(13) Vaicikauskas, V.; Kaucikas, M.; Swedas, V.; Kuprionis, Z., *Instrum.*, **2007**, *78*, 023106.

(14) Andreev, Y.M.; Geiko, P.P.; Krekov, G.M., *Proc. SPIE*, **1991**, *1811*, 367-370.

(15) Bamford, D.J.: Cook, D.J.; Sharpe, S.J.; Van Pelt, A.D., *Appl. Opt.*, **2007**, *46*, 3958-3968.

(16) Udem, T.; Holzwarth, R.; Hänsch, T.W., *Nature*, **2002**, *416*, 233-237.

(17) DiSalvo, F.J., *Science*, **1999**, *285*, 703-706.

(18) Chen, G.; Dresselhaus, M.S.; Dresselhaus, G.; Fleurial, J.P.; Caillat, T., *Int. Mater. Rev.*, **2003**, *48*, 45-66.

(19) Tsuji, I.; Shimodaira, Y.; Kato, H.; Kobayashi, K.; Kudo, A., *Chem. Mater.*, **2010**, *22,* 1402-1409.

(20) Takada, K., *Acta Materialia*, **2013**, *61*, 759-770.

(21) Knauth, P., *Solid State Ionics*, **2009**, *180*, 911-916.

(22) Brant, J.A.; Devlin, K.P.; Bischoff, C.; Watson, D.; Martin, S.W.; Gross, M.D.; Aitken, J.A., *Solid State Ionics*, **2015**, *278*, 268-274.

(23) Cheng, Y.; Peng, B.; Hu, Z.; Zhou, Z.; Lui, M., *Phys. Lett. A*, **2018**, *382*, 3018-3025.

(24) Joshi, V.K., *Eng. Sci. Technol. Int. J.*, **2016**, *19*, 1503-1513.

(25) Leung, C.M.; Li, J.; Viehland, D.; Zhuang, X., *J. Phys, D: Appl. Phys.*, **2018**, *51*, 263002.

(26) Lu, J.W.; Chen, E.; Kabir, M.; Stan, M.R.; Wolf, S.A., *Int. Mater. Rev.*, **2016**, *61*, 456-472.

(27) Žutic, I.; Fabian, J.;. Sarma, S.D., *Rev. Mod. Phys.*, **2004**, *76*, 323-410.

(28) Gerlach, W., *Physikalische Zeitschrift*, **1922**, *23*, 114-120.

(29) Aminof, G., *Zeitschrift fuer Kristallographie*, **1923**, *58*, 203-219.

(30) Just, J.; Lützenkirchen-Hecht, D.; Frahm, R.; Schorr, S.; Unold, T., *Appl. Phys. Lett.*, **2011**, *99*, 262105.

(31) Dimitrievska, M.; Xie, H.; Fairbrother, A.; Fontané, X.; Gurieva, G.; Saucedo, E.; Pérez-Rodríguez, A.; Schorr, S; Izquierdo-Roca, V., *Appl. Phys. Lett.*, **2014**, *105*, 031913.

(32) Brunetta, C.D.;. Minsterman III, W.C.; Lake, C.H.; Aitken, J.A., *J. Solid State Chem.,* **2012**, 187, 177-185.

(33) Parthé, E.; Yvon, K.; Deitch, R.H., *Acta Cryst.*, **1969**, *B25*, 1164-1174.

(34) Devlin, K.P.; Glaid, A.J.; Brant, J.A.; Zhang, J.-H.; Srnec, M.N.; Clark, D.J.; Kim, Y.S.; Jang, J.I.; Daley, K.R.; Moreau, M.A.; Madura, J.D.; Aitken, J.A., *J. Solid State Chem.*, **2015**, *231*, 256-266.

(35) Liang, F.; Kang, L.; Lin, Z.; Wu, Y,; Chen, C., *Coordination Chemistry Review*, **2017**, 333, 57-70.

(36) Mardix, S., *Phys. Rev. B.*, **1986**, *33*, 8677-8684.

(37) Myer, G.H.; *American Mineralogist*, **1962**, *47*, 977-978.

(38) Fleet, M.E., *American Mineralogist*, **1977**, *62*, 540-546.

(39) Brafman, O.; Steinberger, I.T., *Phys. Rev.*, **1966**, *143,* 501-505.

(40) Kattan, N.; Hou, B.; Fermín, D.J.; Cherns, D., *Appl. Mater. Today*, **2015**, *1*, 52-59.

(41) Just, J.; Lützenkirchen-Hecht, D.; Frahm, R.; Schorr, S.; Unold, T., *Appl. Phys. Lett.*, **2011**, *99*, 262105.

(42) Just, J.; Sutter-Fella, C.M.; Lützenkirchen-Hecht, D.; Frahm, R.; Schorr, S.; Unold, T., *Phys. Chem. Chem. Phys.*, **2016**, *18*, 15988.

(43) Dimitrievska, M.; Xie, H.; Fairbrother, A.; Fontané, X.; Gurieva, G.; Saucedo, E.; Pérez-Rodríguez, A.; Schorr, S.; Izquierdo-Roca, V., *Appl. Phys. Lett.*, **2014**, *105*, 031913.

(44) H. Cui, W. Li, X. Liu, N. Song, C.-Y. Lee, F. Liu, X. Hao, *Appl. Phys. A*, **2015**, *118*, 893-899.

(45) Kattan, N.; Hou, B.; Fermín, D.J.; Cherns, D., *Appl. Mater. Today*, **2015**, *1*, 52-59.

(46) Bosson, C.J.; Birch, M.T.; Halliday, D.P.; Tang, C.C.; Kleppe, A.K.; Hatton, P.D., *Chem. Mater.*, **2017**, *29*, 9829-9839.

(47) Delbos, S., *EPJ Potovoltaics*, **2012**, *3*, 35004.

(48) Chen, S.; Gong, X.G.; Walsh, A.; Wei, S.-H., *Appl. Phys. Lett.*, **2010**, *96*, 021902.

(49) Valakh, M.Y.; Dzhagan, V.M.; Babichuk, I.S.; Fontane, X.; Perez-Rodriguez, A.; Schorr, S., *JETP Letters*, **2013**, *98*, 255-258.

(50) Chen, S.; Yang, J.-H.; Gong, X.G.; Walsh, A.; Wei, S.-H., *Phys. Rev. B*, **2010**, *81*, 245204.

(51) Bais, P.; Caldes, M.T.; Paris, M.; Guillot-Deudon, C.; Fertey, P.; Domenges, B.; Lafond, A, *Inorg. Chem.*, **2017**, 56, 11779-11786.

(52) Nitsche, R.; Sargent, D.F.; Wild, P., *J. Cryst. Growth* **1967**, *1*, 52-53.

(53) Schleich, D.M.; Wold, A., *Mater. Res. Bull.* **1977**, *12*, 111.

(54) Yao, G.Q.; Shen, H.S.; Honig, E.D.; Kershaw, R.; Dwight, K.; Wold, A., *Solid State Ionics* **1987**, *24,* 249.

(55) Levcenco, S.; Dumcenco, D.; Huang, Y.S.; Arushanov, E.; Tezlevan, V.; Tiong, K.K.; Du, C.H., *J. Alloys Compd.* **2010**, *506*, 46-50.

(56) Rosmus, K.A.; Aitken, J.A., *Acta Crystallogr., Sect. E* **2011**, *67*, i28.

(57) Rosmus, K.A.; Brunetta, C.D.; Srnec, M.N.; Karuppannan, B.; Aitken, J.A., *Z. Anorg. Allg. Chem.* **2012**, *638*, 2578-2584.

(58) Levcenco, S.; Dumcenco, D.; Huang, Y.S.; Arushanov, E.; Tezlevan, V.; Tiong, K.K.; Du, C.H., *J. Appl. Phys.*, **2010**, *108*, 073508-073512.

(59) Levcenco, S.; Dumcenco, D.; Huang, Y.S.; Arushanov, E.; Tezlevan, V.;. Tiong, K.K.; Du, C.H., *J. Alloys Compd.*, **2011**, *509*, 4924-4928.

(60) Rosmus, K.A.; Brant, J.A.; Wisneski, S.D.; Clark, D.J.; Kim, Y.S.; Jang, J.I.; Brunetta, C.D.; Zhang, J.-H.; Srnec,M.N.; Aitken, J.A., *Inorg. Chem.*, **2014**, *53*, 7809-7811.

(61) Džimbeg-Malčić, V.; Barbarić-Mikočević, Ž.; Itrić, K., *Technical Gazette*, 2011, **18**, 117-124.

(62) Toby, B.H., Van Dreele, R.B., "GSAS-II: the genesis of a modern open-source all purpose crystallographic software package", *J. Appl. Crystallogr.*, **2013,** *46*, 544-548.

(63) *Handbook of Mathematical Functions* (Eds.: M. Abramowitz, I. A. Stegun), Dover Publications, Dover, NY, **1965**, ch. 22.

(64) Larsen, F. H.; Jakobsen, H. J.; Ellis, P. D.; Nielsen, N. C. QCPMG-MAS NMR of Half-Integer Quadrupolar Nuclei. *J. Magn. Reson*. **1998**, *131*, 144–147.

(65) Massiot, D.; Fayon, F.; Capron, M.; King, I.; Le Calvé, S.; Alonso, B.; Durand, J.-O.; Bujoli, B.; Gan Z.; Hoatson, G., *Magn. Reson. Chem*., **2002**, *40*, 70–76.

(66) Agrawal, B.K.; Yadav, P.S.; Agraw, S., *Phase Transition*, **1992**, 38, 127-220.

Chapter 7: Conclusions

7.1 Restatement of Overall Research Goal

The overall goal of this research was to identify new candidate IR-NLO material among quaternary I_2-II-IV-VI_4 and I_4-II-IV_2-VI_7 diamond-like semiconductors and study their physicochemical properties as microcrystalline powders and large single crystal samples. This knowledge was then to be used to assess if these compounds are commercially viable for IR-NLO applications, by surpassing at least one of the desired properties of commercially available IR-NLO crystals, specifically $AgGaS_2$ and $AgGaSe_2$. (*1*) To this end five DLSs have been investigated; Li_2MnGeS_4, $Cu_4MnGe_2S_7$, $Cu_4CdSi_2S_7$, Li_2ZnSiS_4 and Cu_2ZnSiS_4.

7.2 Chapter 2 Conclusions

In Chapter 2, Li_2MnGeS_4, a previously reported DLS, was investigated. (*2*) Brant et al. showed that Li_2MnGeS_4 was a candidate IR-NLO material due to its nonlinear optical properties, most notably its laser induced damage threshold (LIDT). (*2*) Iodine vapor transport (IVT) was utilized for the growth of sizable single crystals due to its previous success in synthesizing sizable single crystals of DLSs. To the best of our knowledge IVT, has not been previously used to synthesize lithium containing chalcogenides, and we quickly discovered that this was most likely due to the extreme reactivity of lithium with the fused-silica reaction vessel. This challenge lead to the development of an interior graphite-tube containment system, which successfully prevented lithium from reacting with the reaction vessel and produced 2x1x1 mm^3 single crystals of Li_2MnGeS_4. (*3*) Thus, marking the first time a lithium chalcogenide material was synthesized via IVT. (*3*) Additionally, the creation and success of the graphite-tube containment system makes IVT a viable option for other lithium-containing compounds such as Li_2CdGeS_4 (*4*), $Li_2MnSnSe_4$

(*5*) and $Li_4HgGe_2S_7$. (*6*) Moving forward, the Bridgman growth method could be utilized to grow larger single crystals to further investigate the intrinsic properties of Li_2MnGeS_4.

7.3 Chapter 3 Conclusions

Chapter 3 investigated the NLO properties of $Cu_4MnGe_2S_7$ and Cu_2MnGeS_4. (*7*) It is interesting that while subtle differences in the structures exist, the differences in SHG and LIDT are more significant. Cu_2MnGeS_4 has a $\chi^{(2)}$ of ~16.9±2.0 pm/V at λ = 3100 nm and a LIDT of 3.4 GW/cm^2 at λ = 1064 nm and τ = 30 ps. (*8*) The $\chi^{(2)}$ of $Cu_4MnGe_2S_7$ was determined to be ~1.63±0.17 pm/V at λ = 1060 nm; the LIDT could not be measured due to the very weak SHG response. (*8*) The weak SHG response of Cu_2MnGeS_4, which is significantly less than that of $AgGaS_2$, but it does have a higher SHG than commercially available $LiInS_2$ and $LiInSe_2$. In contrast, the $Cu_4MnGe_2S_7$ was a poor NLO performer. Future directions for this would could include determining why the NLO properties of $Cu_4MnGe_2S_7$ are so much lower than those of Cu_2MnGeS_4.

7.4 Chapter 4 Conclusions

The new I_4-II-IV_2-VI_7 DLS $Cu_4CdSi_2S_7$ was reported in chapter 4. This new material was compared to Cu_2CdSiS_4 based on its physical and electronic structure. It is interesting to note that while these two compounds differ in structure and $Cu_4MnGe_2S_7$ breaks Pauling's second rule, the electronic structures of both compounds are similar. The NLO properties of $Cu_4CdSi_2S_7$ were not assessed due to synthetic difficulties, but moving forward it would be interesting to attempt to grow large single crystals of this material to further determine its commercial viability. I would suggest using the Bridgman growth method to accomplish this.

7.5 Chapter 5 Conclusions

Li_2ZnSiS_4 was determined to be a wide bandgap material in Chapter 5. The experimental bandgaps of Li_2ZnSiS_4 was determined to be 4.2 eV. The DTA data could be used as a guide for future synthesize large crystals of Li_2ZnSiS_4 on which the intrinsic properties could be determined, although the poor synthetic reproducibility of Li_2ZnSiS_4 as a microcrystalline powder should be considered. If this material is to be further investigated for large-scale crystal growth would be suggested. This material is a candidate for IVT using the graphite-tube containment system created for the work in Chapter 1.

7.6 Chapter 6 Conclusions

Chapter 6 focused on obtaining a preferred synthesis of one of the polymorphs of Cu_2ZnSiS_4 through different cooling rates. While this goal was not achieved, a third polymorph, "namely gamma", was discovered, which is a disordered version of the beta polymorph. Solid-state NMR and neutron diffraction data were instrumental in this discovery. As isolation of one polymorph was not attained, future work should focus on single crystal growth experiments which may be more successful in producing one polymorph.

7.7 References

(1) Eksma Optics, http://eskmaoptics.com/out/media/IR.pdf (Accessed March 9, 2019)

(2) Brant, J.A.; Clark, D.J.; Kim, Y.S.; Jang, J.I.; Weiland, A.; Aitken, J.A., *Inorg. Chem.*, **2015**, 54, 2809-2819.

(3) J.R. Glenn, J.R.; Yao, Y.; Aitken, J.A., *J. Cryst. Growth. Submitted*

(4) Brant, J.A.; Clark, D.J.; Kim, Y.S.; Jang, J.I.; Zhang, J.-H.; Aitken, J.A., *Chem. Mater.,* **2014**, 26, 3045-3048.

(5) Li, X.; Li, C.; Zhou, M.; Wu, Y.; Yao, J., *Chem. Asian J.,* **2017**, 12, 3172-3177.

(6) Wu, K.; Yang, Z.; Pan, S., *Chem. Commun.,* **2017**, 53, 3010.

(7) Bernert, T.; Pfitzner, A., *Z. Kristallogr.*, **2005**, 220, 968-972.

(*8*) Glenn, J.R.; Cho, J.B.; Jang, J.I.; Wang, R.; Rondinelli, J.M.; MacNeil, J.H.; Cribbs, M.M.; Stoyko, S.S.; Barton, C.; Aitken, J.A., *Dalton Trans.*, manuscript in progress.